Funded by the
European Union

ICE GENESIS

Creating the next generation of 3D simulation means for icing

Type of action: Research and Innovation Action

Call identifier: H2020-MG-2018-SingleStage

Topic: MG-2-5-2018 Innovative technologies for improving aviation safety and certification in icing conditions

---

Deliverable D3.4

Definition of Numerical Capability Requirements for Liquid Icing Conditions

---

EC Grant Agreement number: 824310

Start date of project: 1 January 2019 Duration: 48 months

Lead beneficiary of this deliverable: 10# DASSAV

Due date of deliverable: 30/04/2019 Actual submission date: 28/05/2019

Version #: R1.2

Project funded by the European Commission within the H2020 Programme (2014-2020)		
Type		
R	Document, report excluding the periodic and final reports	X
DEM	Demonstrator, pilot, prototype	
DEC	Websites, patents filing, press & media actions, videos, etc.	
OTHER	Software, technical diagram, etc.	
ETHICS	Ethics requirement	
ORDP	Open Research Data Pilot	
Dissemination level		
PU	PUBLIC, fully open, no embargo e.g. web	X
PU*	PUBLIC after embargo of 12 months	
RE	RESTRICTED, only for certain members of the consortium (including the Commission Services): specify here which consortium members have access to the document	
CO	CONFIDENTIAL, only for members of the consortium (including the Commission Services)	
CO+IGAB	CONFIDENTIAL, only for members of the consortium (including the Commission Services) and for the ICE GENESIS Advisory Board	

Revision History

V #	Date	Description / Reason of change	Author
		Part 1	
R0.1	15/02/2019	Draft version	P. Trontin
R1.1	15/03/2019	First version with partners contributions	”
R2.1	25/03/2019	Revised version with questions	O. Rouzaud
R2.2	05/04/2019	Revised version without synthesis	”
R2.3	05/04/2019	Second revised version without synthesis	“
R3.1	16/04/2019	Version with the synthesis + comments from the IGAB (Piaggio)	“
R3.2	10/05/2019	Version with the reviewers’ comments	O. Rouzaud
		Part 2	
0.1	25/02/2019	First draft	All
0.2	08/03/2019	Preliminary release to AB	All
0.3	08/04/2019	Comments from AIHs	
0.4	12/04/2019	Comments from AB and code developers	Lead +contributors
		Final	
1.0	13/05/2019	Merge Part 1 & 2	Lead
1.1	13/05/2019	Comments from reviewers	Lead
1.2	27/05/2019	Final revision	Lead

Deliverable Contributors

Authors

Organisation	Authors’ name
DASSAV	CAMINADE François, FRAZZA Loïc
ONERA	ROUZAUD Olivier, TRONTIN Pierre

Contributors

Organisation	Contributors’ name
ONERA	S. Landier, P. Lavoie, S. Peron, E. Radenac, P. Trontin
CIRA	F. Capizzano, P. Catalano, D. de Rosa, E. Iuliano, F. Morlando, F. Petrosino
AIRBUS	J. Cliquet
AIH	L. Artal

LDO	M. Di Muzio
ATR	A. Sperandio
SAF-AE	G. Linassier
GE	P. Vanacore
RR	G. Jones
SONACA	B. Bernay
LIEBHERR	C. Lenoir
POLIMI	A. Guardone
TUBS	S. Bansmer, D. Sotomayor Zakharov
TUDA	J. Breitenbach, I. Roisman, M. Schremb, C. Tropea

Internal Reviewers

Organisation	Internal Reviewers' name
CU	PERVIER Hugo (Part 1)
SAE	LINASSIER Guillaume (Part 1)
POLIMI	GUARDONE Alberto (Part 2)
LDO	CERESOLA Nicola (Part 2)
AIRBUS	MOLLER Marianne (Project Coordinator)

Table of Contents

Table of Tables

Table of Figures

1 Glossary

Abbreviation / Acronym	Description/meaning
AB	Advisory Board
AMC	Acceptable Means of Compliance
App	Appendix (C, O)
ARAC	Aviation Rulemaking Advisory Committee
CS-25/29	Certification Specification
EASp	European Aviation Safety Programme
FAR 25/29/33	Federal Aviation Regulations
FZDZ	Freezing Drizzle
FZRA	Freezing Rain
MS	Multi-Step first order calculation
MSPC	Multiple-step higher order predictor-corrector
PC	Predictor-Corrector scheme
SLD	Supercooled Large Droplet
AGC	Aupoix-Grigson-Colebrook
ALE	Arbitrary Lagrangian-Eulerian
AMR	Automatic Mesh Refinement
DNS	Direct Numerical Simulation
EMVD	Effective Mean Volume Diameter
h*	Non dimensional film thickness
IB	Immersed Boundary
IBM	Immersed Boundary Method
IDW	Inverse Distance Weighting
LES	Large Eddy Simulation
LWC	Liquid Water Content
MST	Marginal Stability Theory
MVD	Mean Volume Diameter
PDE	Partial Differential Equation
Ra	Mean roughness
RANS	Reynolds Averaged Navier-Stokes
RBF	Radial Basis Function
RHS	Right Hand Side
RMH	Roughness Maximal Height

VOF	Volume Of Fluid

2 Executive Summary

This document takes part to the first steps of the project as it describes the state of the art and the expectations for all the workflow which is foreseen on computational improvements for Liquid droplets modelling in App C and App O. It is organized in two main parts.

The first part is a literature review for liquid icing conditions. The aim is to perform an exhaustive review on the existing models, numerical techniques and experimental data that are currently available for the development of 3D numerical tools for App C and O. Four main topics have been identified:

1) Numerical methods for meshing. Different techniques are studied: immersed boundary methods (IBM), mesh deformation and automatic re-meshing.
2) Roughness characterization for App C and O. Characterization of boundary layers on rough walls is proposed too.
3) Supercooled large droplets (SLD). Models for the partial deposit of impacting droplets and characterization of the secondary (re-emitted) droplets are proposed.
4) Ice density.

The results of the previous EU projects (EXTICE, HAIC, STORM) are reviewed as well as the German (SFB TRR75 and SFB TRR150) and French (PHYSICE and PHYSICE2) projects. The objective is to provide the main conclusions as well as the gaps and future objectives to be achieved within the framework of ICE GENESIS.

Regarding numerical methods for meshing, IBM literature on the ice-accretion topic is relatively young. As far as automatic remeshing is concerned, restrictions are observed with confined geometries and complex ice shapes. The objective in ICE GENESIS is to generate grids in a robust way.

Regarding roughness, main models are tested on several test cases. A large dispersion is observed among the different models. One of the main difficulties is the definition of typical length scales: the roughness thickness in the definition of the coefficient k_s or a reference length relevant to define a dimensionless roughness height. Another point to be addressed within ICE GENESIS is the laminar/turbulent transition for a rough boundary layer.

Regarding SLDs, although numerous studies on drop impacts and splashing have been performed in the past, secondary droplets originating from SLDs have not been investigated exhaustively. The influence of properties of the surrounding gas still remains a point. The existing investigations on drop impacts with temperatures above freezing, which can be classified into impacts on dry or wet surfaces, have to be extended by possible effects due to supercooling. As far as sticking efficiency coefficient ε_s is concerned, universal trends are observed for several experiments: an increase of ε_s with the droplet diameter and velocity, followed by a threshold. Different substrates were investigated like cold solid substrates including superhydrophobic and partially wettable substrates.

This bibliographic review is a starting point for WP9 (Numerical capability development for liquid icing conditions) where the models and the dedicated numerical tools presented will be improved and validated with respect to Appendix C and O conditions. Taking into account the conclusions of the report dedicated to the requirements for the 3D numerical tools, the models and methods presented here will then be integrated and validated in industrial environment (WP11).

The purpose of the second part is:

- To specify 3D numerical tools requirements that are needed by aeronautical industries to certify their products with validated and reliable numerical tools in the scope of Super Cooled Large Droplets (SLD)

The main idea about these requirements is not only to give a list of requirements that have to be achieved by the final release of the computational tools, but also to provide more information like the expected level of accuracy or any level of priority. As these requirements have to be used by code developers from Research Institutes and Academia which are not fully aware of industrial context, attention is paid to deliver the most pertinent information for each requirement, together with quantitative and qualitative data like orders of magnitude or other practical fact (time for computations, …).

These requirements keep the tracks back from previous project in icing (HAIC, STORM). We also identify essential features that will have to be included in tools to deal with the full icing Appendices envelope, but that are not in the scope of ICE-GENESIS. By the way, specific requirements addressed for ICE-GENESIS are highlighted in order to ease the understanding of what is expected in the scope of the project.

This work will serve as inputs for:

- WP9 for numerical tools improvements and basic experiments
- WP11 for numerical tools integration and validation in industrial environments

All topics in the document are related to liquid droplets only.

3 Literature review

3.1 Introduction

This report is a literature review of the works prior to the ICE GENESIS project. Results of previous EU projects (EXTICE, HAIC, STORM) are reviewed as well as German projects (SFB TRR75 & SFB TRR150) and French projects PHYSICE and PHYSICE2 notably. The addressed topics are:

- Numerical methods for meshing. Different techniques are studied: immersed boundary methods (IBM), mesh deformation and automatic re-meshing;
- Roughness characterization for App C and O. Characterization of boundary layers on rough walls is proposed too;
- Supercooled large droplets (SLD). Models for the partial deposit of impacting droplets and characterization of the secondary (re-emitted) droplets are proposed;
- Ice density.

The objective is to provide the main conclusions as well as the gaps and future objectives to be achieved within the framework of ICE GENESIS.

3.2 Literature review on the existing models, numerical techniques and experimental data available for Appendices C and O

3.2.1 Numerical methods for meshing

3.2.1.1 Conclusions from STORM [ONERA]

3.2.1.1.1 Main results

In-flight ice accretion modelling is based on sequential calls to several solvers: aerodynamic field solution around the icing surface, droplet trajectory calculation and mass and energy balance for the water deposited on the surface. This sequential approach produces the amount of ice which freezes locally, from which an update of the ice shape is inferred. In the European project STORM work package 4, ice accretion modelling was addressed for the purposes of aero-engine icing prediction [1]. The key capabilities of icing suites investigated in the STORM project were thus: three-dimensionality, inertial forces for rotating parts, droplet re-emission model from one row of the engine to the subsequent one. Among other achievements, such as rivulet modelling, multi-layer models have been implemented in ONERA's code CEDRE, CIRA's version of OpenFOAM and AEROTEX's code HETEMS, to account for water accretion and runback through shallow-water approach.

Particular attention has been paid to the so-called "cascade rig" data-base developed in STORM WP4, in the Cranfield University icing wind-tunnel. The experiment consisted in investigating the ice accretion on two consecutive static rows of engine inlet blades (a row of struts followed by a row of variable stator vanes, VSV, Figure 1). The geometry is mainly 2D and could be computed with both the 3D codes developed in STORM and more usual 2D icing suites such as ONERA's IGLOO2D [2]. With IGLOO2D, it is possible to use either the multi-step approach or the so-called "predictor-corrector" approach. In the last case, only two steps are necessary, and re-meshing is thus used only once. In the former case, the aerodynamic and droplet trajectory solutions must be computed around the updated ice shape during the course of the simulation. On the contrary, only the predictor approach is available for the codes upgraded during the STORM project, such as ONERA's code CEDRE/FILM or CIRAS's version of OpenFOAM, which means that the retroaction of the ice growth on the aerodynamic and droplet fields is not modelled: only one aerodynamic field computation is performed around the clean geometry.

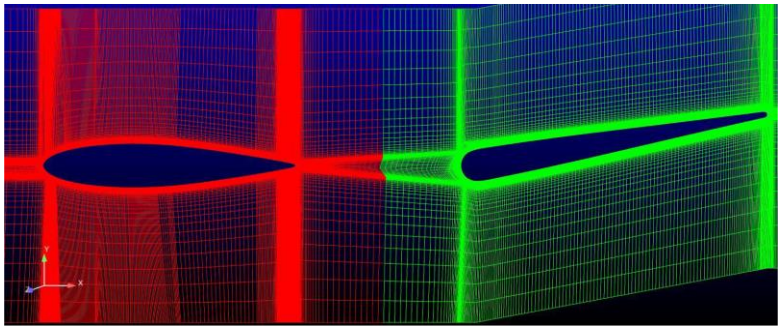

Figure 1 - Grid used for the cascade rig test-case with ONERA's code CEDRE (strut in red, VSV in green)

Figure 2 and Figure 3 show that the codes FILM and OpenFOAM fail in capturing both the rime and glaze ice shapes on the strut blade row. Regarding the rime ice shape, there is quite good agreement

between the “predictor” ice shapes of IGLOO2D and FILM, whereas the OpenFOAM’s shape is less thick. However, all codes predict ice shapes which are much too thick compared to the experiment. The “predictor-corrector” and multi-step (10 steps) approaches partly solve that problem, although the predicted ice shape is not fully satisfactory yet. It must be mentioned that the time step setting was defined arbitrarily, and that there is no best practice to set it (impact on the ice shape calculation) at the moment.

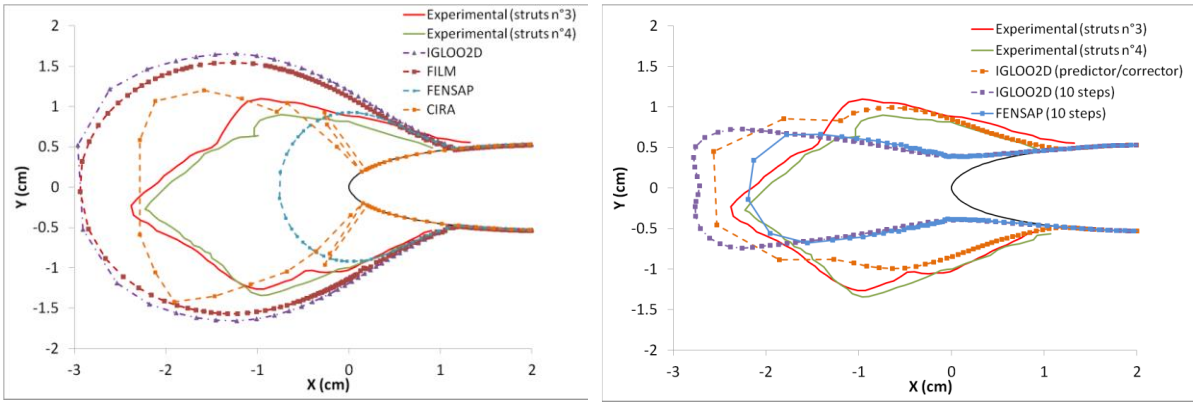

Figure 2 - Ice accretion calculation with predictor approach around the cascade rig rime case [1]

Regarding the glaze-ice case, the agreement between the codes on the “predictor” ice shape is poorer, because there are discrepancies on the heat transfer coefficients predicted by the various codes. More interestingly, the impact of re-meshing and especially “predictor-corrector” approach was shown while employing IGLOO2D. Figure 3 shows that it is indeed possible to produce a correct ice shape with this approach although a parametric study on the LWC was necessary, in a range compatible with the experimental uncertainties.

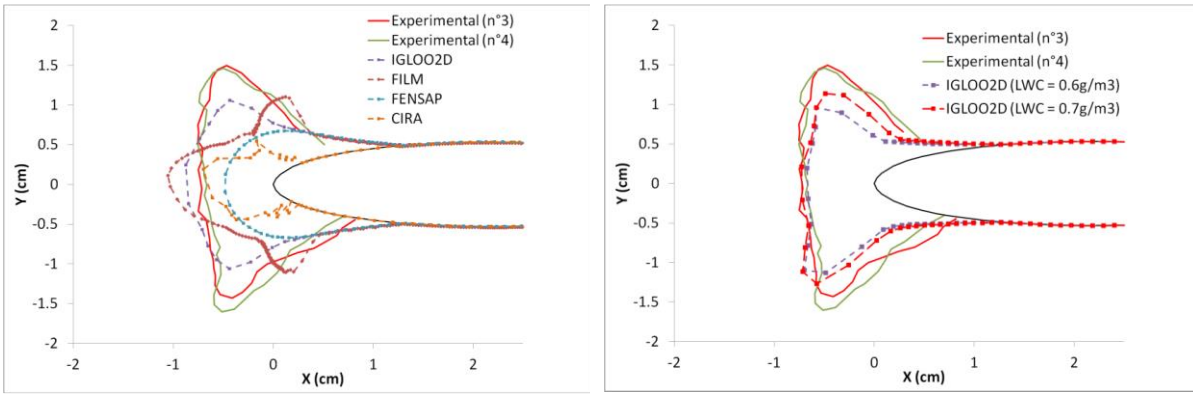

Figure 3 - Ice accretion calculation with predictor approach around the cascade rig glaze case [1]

3.2.1.1.2 Lessons learned, limitations, recommendations

Results from STORM project demonstrate that the predictor approach is not really satisfactory either for rime- or glaze-ice 2D simulations while the predictor-corrector and the multi-step approaches tend to improve the results. Re-meshing is also a good candidate for improvements. In any case, one of the main conclusions of the STORM project is that there is a strong need for multi-step methods in 3D ice accretion tools [1].

Three options will be investigated during the ICE-GENESIS project to cope with the need for the retroaction of the ice shape growth on the aerodynamic and droplet fields: automatic re-meshing to

provide a new grid to the aerodynamic and droplet solvers, mesh deformation to update the initial grid, and immersed boundary method to tag the grid cells in which ice deposition

3.2.1.1 Immersed Boundary methods (IBM) [CIRA, ONERA, TUDA]

3.2.1.1.1 Objectives and issues

Immersed boundary (IB) methods have largely developed in the last decade mainly thanks to their intrinsic fast and automatic meshing capability. Indeed, this approach relies on Cartesian grids which are, by nature, very easy to build and/or to modify. Of course, accounting for the presence of an obstacle necessitates developing ad hoc algorithms. For instance, in the direct forcing approach, the presence of a wall is modelled through a forcing term, which appears in the flow governing equations. However that may be, using Cartesian grid allows high flexibility in analysing the fluid dynamics of complex three-dimensional configurations like Fluid-Structure interaction or bio-dynamics flow. Actually, the IB approach represents a valid alternative to classic body-conforming structured or unstructured methods whose main quality is the near-wall accuracy but at the cost of a huge manpower and a high turn-around time required for developing complex hand-made meshes. On the other hand, IB methods have reached a good level of sophistication for a wide range of engineering applications. For example, the reliability of IB solutions is comparable to that of body-fitted solutions especially for laminar incompressible/compressible flows. High Reynolds number applications remain a challenging goal for every Cartesian method (IBM or cut-cell). Indeed, even if anisotropic refinement plays, the classical integration to the wall approach requires a huge amount of Cartesian cells that fatally affects the available computational resources. However, latest developments suggest the use of wall-modelling to compute the correct wall shear-stress at high Reynolds numbers.
One of the natural IB targets is ice-accretion. In particular, the Eulerian approach for water droplet impingement does not represent a challenging problem for the actual capabilities of IB methods. Encouraging results of different research groups in Europe and worldwide demonstrate a viable road for robust and time-accurate ice-accretion simulations. Indeed, the ability of accurate predictor-corrector analyses is an essential pre-requisite for ice-accretion. In this sense, the automation and speed qualities of IB meshing tools represent a potentially promising way for a complete and robust two-phase flow/ice-accretion simulation chain.

In the following subsections, a non-exhaustive review of different IB developments/applications is carried out in order to focus on the potential developments in the GENESIS Project framework.

3.2.1.1.2 Literature review

3.2.1.1.2.1 Phase-field method with IB points for freezing of supercooled water

3.2.1.1.2.1.1 Description

In the scope of the German collaborative research project SFB-TRR 75, solidification of supercooled water has been numerically studied employing a phase-field approach for the propagation of the solid-liquid interface [3]. The melting temperature as one of the couplings between the temperature fields in the solid and the liquid phase is imposed at immersed boundary points used to re-construct the phase interface. The computational model has been validated using the analytical solution for the two-phase Stefan problem, and has been extended to incorporate conjugate heat transfer between the fluid phases and a neighbouring solid substrate.

3.2.1.1.2.1.2 Main results, progress and limitations

The presented model has a good capability for the computation of the solidification in the absence of walls, or far from a wall. At a wall, the problem formulation imposes a singularity, indicated by

diverging velocities at the water-ice-wall contact line. The heat flux singularity at the contact line presents a fundamental difficulty for modelling phase change within the finite-volume continuum mechanics. New understanding of the underlying physics must be acquired, in order to formulate plausible models which would remove the singularity and provide means for using them within the conventional continuum framework. The present model has not been, but could be, easily extended towards a curvature-dependent temperature at the phase interface yet. Figure 4 shows the computed solid-liquid interface shape with the developed temperature field and the velocity field at $t = 0.001$ ms for a mesh with 200×400 cells [3].

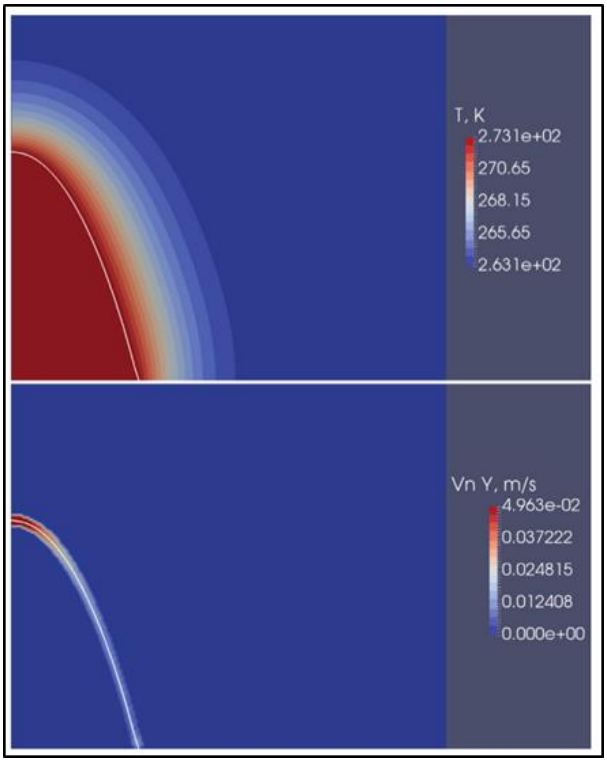

Figure 4 - The computed temperature field and the velocity field within the diffused interface band

In terms of computational costs, the model will by definition perform faster than the level-set method for capturing the phase interface, since re-initialization of the phase-field variable and computation of the extended velocity field, required for the re-initialization in the entire computational domain, is not necessary in the present model.

3.2.1.1.2.2 Level-Set method with IB points for freezing of supercooled water

3.2.1.1.2.2.1 Description

In the scope of the German collaborative research project SFB-TRR 75, dendritic freezing of supercooled water has been numerically studied using a Level-Set (LS) approach for capturing the solid-liquid phase interface [4] [5] [6]. It has been implemented in the open-source frame work OpenFOAM and employs immersed boundary points to impose the boundary conditions at the phase interface.

3.2.1.1.2.2.2 Main results, progress and limitations

The basic computational model has been validated by means of a comparison with the Marginal Stability Theory (MST) introduced by Langer and Müller-Krumbhaar [7]. Its performance has been assessed based on the computation of dendritic freezing of supercooled water. The tip velocity of two-dimensional dendrites growing in supercooled water has been determined and the computational results compared with corresponding experimental results and theoretical predictions in the range of supercooling between ΔT = 1 K and ΔT = 30 K [4] [5]. As shown in Figure 5, the computational results follow closely the theoretical predictions for the tip velocity of a single dendrite over the entire range of supercooling. However, the theory and the numerical model in its basic form deviate from the experimental observations for supercooling higher than approximately 5-6 K, since the theoretical as well as the basic computational model do not account for kinetic effects. To overcome this deviation, a term accounting for kinetic undercooling of the phase interface has been implemented into the LS approach [6]. With this extension, the computational model well predicts dendritic freezing also for higher supercooling up to approximately ΔT = 20 K.

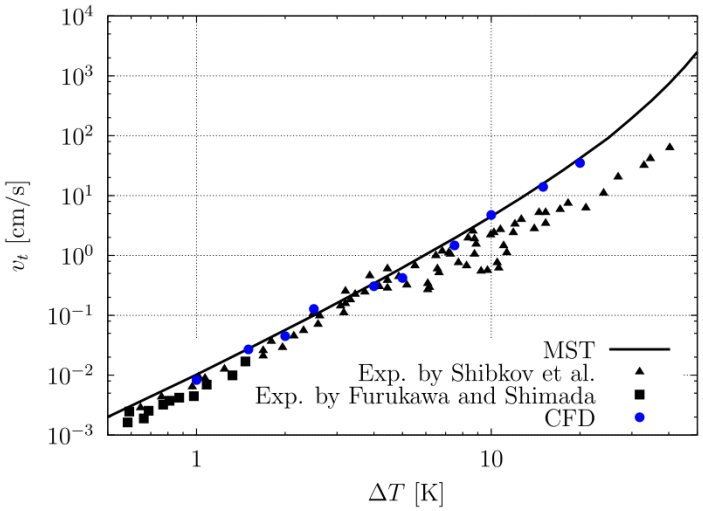

Figure 5 - Ice crystals freely growing from supercooled pure water with tip velocity v_f as a function of the initial supercooling ΔT. Comparison of the results obtained by the Level-Set approach with available experimental data and the marginal stability theory (MST) of Langer and Müller-Krumbhaar [7].

3.2.1.1.2.3 Water Droplet Impingement in the framework of the CIRA IBM Method

3.2.1.1.2.3.1 Description

The numerical simulation of ice-accretion on aerodynamic surfaces is as a multidisciplinary process whose main elements are aerodynamics, transport of multi-phase flows and heat transfer. The interest on this topic is demonstrated by the launching of different European Projects (e.g., EXTICE, HAIC, STORM) whose principal actors are aeronautical industries, research centers and academic laboratories. Icing-wind tunnel experiments and numerical approaches are used in a complementary way to improve the understanding of the ice accretion physical phenomena. In particular, during the EXTICE Project, a research activity dealt with the study, development and validation of a three-dimensional Cartesian method able to estimate the water collection onto aircraft forward surfaces by using an immersed boundary (IB) technique. The basic idea was to take advantage of the fast and

robust SIMBA simulation system based on an IB method, developed at CIRA by Capizzano et al. in the last years, which is able to simulate Euler/RANS flows around complex two- and three-dimensional configurations [8] [9]. The long-term objective is to develop a numerical tool able to investigate ice-accretion. Indeed, a high level of automation and a certain flexibility in treating arbitrary geometries characterize Cartesian grid methods. Thus, they are good candidates to treat ice-shapes. A user-friendly automatic grid generator allows local mesh refinements without restrictions on the number of refinement levels thanks to the adoption of a fully unstructured data management [10]. The SIMBA method is based on a discrete-forcing and is similar to many other approaches in literature (see for example Fadlun et al. [11], Tseng et al. [12], Yang et al. [13]). A discrete-forcing term is added to the right hand side of the momentum equation in an indirect way by means of a direct boundary condition (BC). Proper near-wall fluxes are used to satisfy the desired BCs by using different reconstruction schemes involving surrounding known values (cell-centers, wall points) and the IB local unit normal vector. Though Eulerian methods proven successful on body-conforming meshes, it is shown that satisfactory results can be obtained by using immersed boundary methods too as shown by Capizzano et al. [14]. Comparisons with experimental data drawn from literature point out a significant potential towards accurate prediction of impingement characteristics on real aircraft components. Other research groups are following analogous approaches with promising results. For example, Wutschitz et al. [15] extended a cut-cell AMR Cartesian method, developed for the air-phase, towards a droplet-phase model around iced bodies in an Eulerian frame of reference. A one-way water-air coupling is assumed in the Eulerian ghost cell immersed boundary technique based on a level-set formulation (IBM-LS) discussed in Al-Kebsi et al. [16].

3.2.1.1.2.3.2 Main results, progress and limitations

Comparisons with experimental data drawn from literature points out a significant potential towards accurate prediction of impingement characteristics on real aircraft components. In particular, the Eulerian method provides excellent results for three-dimensional water droplet fields if compared with both experiments and other body-conforming data (see, for example, the case shown in Figure 6). Generally speaking, the developed method provides a more fast and flexible way to compute water droplet impingement while preserving the robustness of classical body-conforming tools. The latter, on the other hand, require skilled specialists to use mesh-generation tools. A time-consuming activity is often spent to generate proper three-dimensional grids especially when treating complex 3D geometries. On the contrary, a robust and highly automatic Cartesian mesh solver allows to save up to 90% of the whole turn-around time for the entire meshing process. The refinement of near-wall regions is guaranteed by proper engines based on recursive cell-splitting procedures (see for example the mesh refinement on the right part of the figure, Figure 6). In particular, the tool allows treating very complex configurations, as the stator-cowl one shown in Figure 7, in a very short CPU time without human aid.

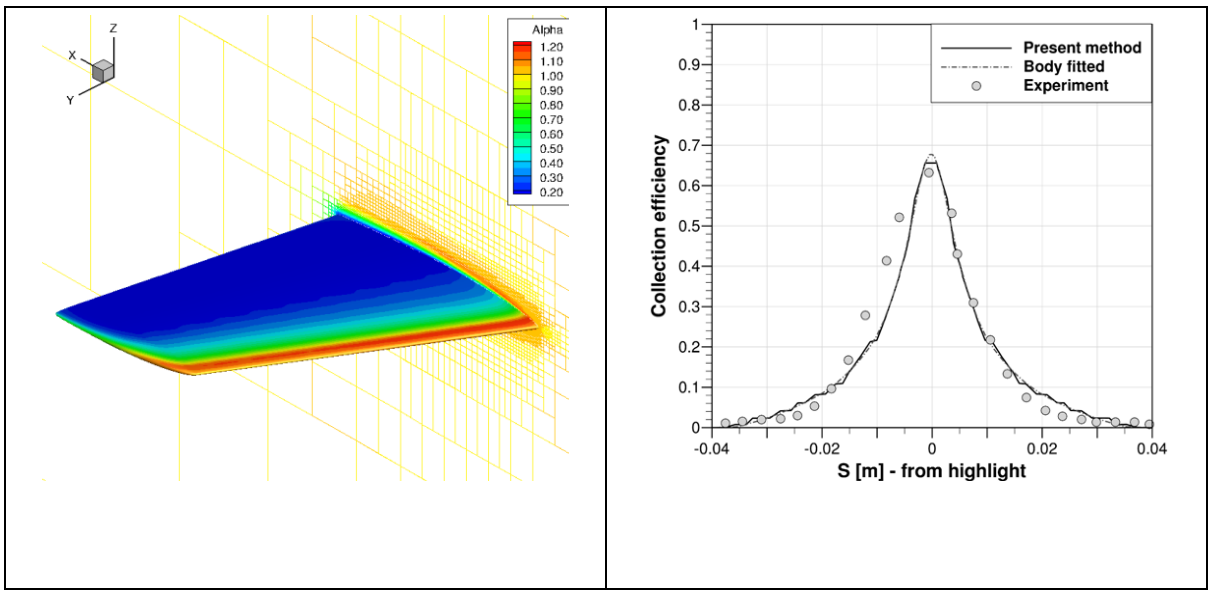

Figure 6 - Example of a phase volume fraction on a 3D tail at α=0° (left) ; example of water collection efficiency at a tail section (right)

The application to the treatment of the dispersed-phase set of equations represents a novelty, as IB techniques traditionally apply to Navier-Stokes simulation. Differently from the latter, the particle phase equations are highly hyperbolic and, after due simplifications, do not contain pressure/viscous terms but rather involve sources to model the interaction with the gas phase.

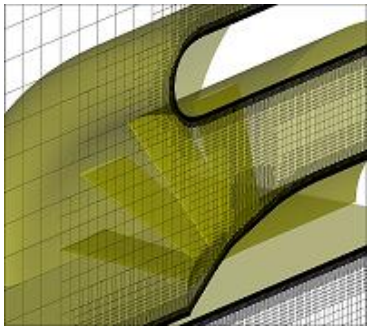

Figure 7 - Example of an AMR Cartesian mesh around a complex 3D cowl-stator configuration

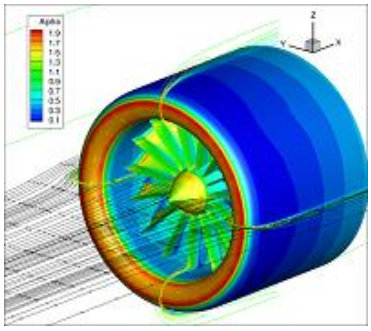

Figure 8 - Example of phase volume fraction distribution on a 3D cowl-stator configuration

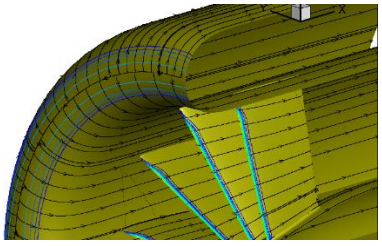

Figure 9 - Local view of a collection efficiency distribution with droplets' trajectories

Moreover, a proper treatment of the sharp change in the boundary conditions across the impingement limits helps to improve the overall tool robustness and convergence qualities. Once solved, the model set of equations give access to the both the volume fraction and the droplet velocities throughout the computational domain and allow a direct computing of the water collection efficiency on the wall surfaces as shown qualitatively in Figure 8 and Figure 9.

At the moment, the SIMBA-ICE tool involves a rime-ice accretion module which however limits the application to only a narrow range of icing conditions. Future improvements are envisaged towards a more sophisticated ice-accretion model in order to allow the simulation of glaze-ice conditions too. For example, a first development would couple the finite-volume IB-method with a classic 1-D Messinger code able of computing ice-accretion along streamlines and/or skin friction lines once the collection efficiency is known.

A higher level of complication is represented by the 2D/3D Level-Set (LS) method proposed by Osher et al. [17] and the 2D-LS Beaugendre et al. [18] whose main goal is to track the ice-air interface by means of a time-accurate PDE of a passive scalar function. This function is set to zero at the interface, positive outside and negative inside. A 2D multi-step ice accretion simulation is proposed in Al-Kebsi et al. [16] for rime and glaze ice wherein the wall boundary is treated coupling the ghost cell immersed boundary technique with the level-set formulation (IBM-LS). An IBM-LS 2D/3D Eulerian approach similar to that of [14] and [18] is developed by Pena et al. [19] in which droplets are allowed to impinge on a layer of cells defined by the LS function. Frolkovič et *al.* [20] propose a 2D-LS framework for evolving the computed ice-accreted wall surface. In particular, the validation campaign deals with several test cases whose results are in good agreement with the literature. In general, multi-layers approaches seem to give interesting results due to their major physical content if compared to simpler one-equation PDE models (e.g. the shallow-water one) [18].

In conclusion, the CIRA SIMBA-ICE 2D/3D Eulerian method is a good candidate for future developments towards complete ice accretion estimation especially if considering the automation and the short turn-around time required for the mesh generation process. In principle, the coupling with an ice accretion module (*e.g.* the 1D Messinger model) is straightforward once a distribution of collection efficiency is available. Otherwise, the film simulation would be developed internally to the IB code in order to have an integrated two-phase flow and ice-accretion framework. For example, a PDE-based multilayer model could be solved in proximity of the wall by exploiting the pre-existent solver data management. Once the water film is solved, the new iced surface would be handled and re-meshed automatically by running the SIMBA-MESH AMR-Cartesian mesher. The whole process would run time-accurate, thus allowing a complete simulation of an in-flight icing phenomena.

3.2.1.1.2.4 IBM approach in ONERA ice accretion codes

3.2.1.1.2.4.1 Description

In a paper proposed to SAE Icing Conference 2019, Lavoie employs the penalization method, which is one of the possible approaches in the IBM methodology, in ONERA's IGLOO2D solver [21]. It means that the Euler equations are penalized in the inviscid solver EULER2D (Figure 10). This method solves the same equations' set in both the solid and fluid regions and uses a "penalty function" at interface cells (wall-surfaces). It differs from the CIRA "pure IB" approach where only the fluid cells are solved and a forcing function implicitly added to the momentum equations to account for solid walls.

In the ONERA example, a slip condition is prescribed at the ice surface splitting the computational domain into two parts, the external flow and the flow "inside the ice". The governing equations are solved in both parts of the flow with their respective boundary conditions. At the end, the external flow solution corresponds to the usual Euler solution while the internal flow is discarded. The figure shows the streamlines and the pressure contours in the external flow as well as the pressure contours in the internal part. The Eulerian trajectography solver TRAJ2D is also penalized to capture the effect of the growing ice on the water collection (Figure 11). The goal is to make it possible to use the clean geometry grid all along the ice accretion computation during a multi-step computation (no remeshing). The extraction of the surface data is also required to communicate the necessary information to the surface solvers (boundary layer and ice accretion solvers).

The scope was restricted to 2D in [21]. However, it is worth mentioning that for ONERA's 3D ice accretion suite IGLOO3D, there are also other tools available at ONERA, based on IBM techniques. In particular, the ghost-cell direct-forcing IBM method is made possible through the use of the pre-processing tool CASSIOPEE coupled with the aerodynamic solver FAST [22] [23].

3.2.1.1.2.4.2 Main results, progress and limitations

It was shown that the Penalization method using a simple first-order boundary condition is an interesting candidate for ice accretion software [21]. It was able to capture rime ice and glaze ice with good accuracy for several icing simulations (one example is given in Figure 12). However, the issue of mesh refinement in the vicinity of the iced area arises. The problem is more serious for the Navier-Stokes approach, where the boundary layer requires a dense mesh wherever the boundary is. For inviscid computations, although the refinement is less important, a refined area may be expected in the whole region where ice is expected. Otherwise, the optimization of the computational cost would consider the automatic mesh adaptation techniques in order to automatically refine high-gradient areas as they appear during the ice growth.

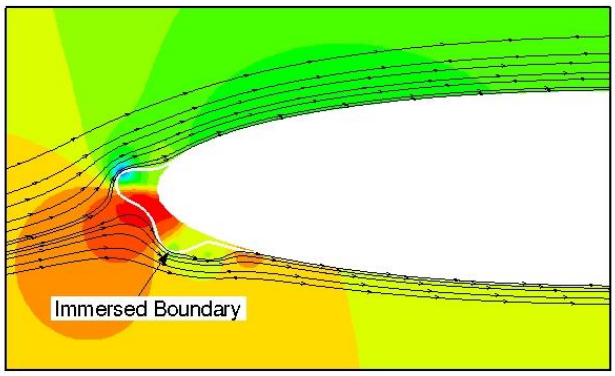

Figure 10 - Example for the Penalized inviscid flow (Euler2D), pressure contours and velocity streamlines

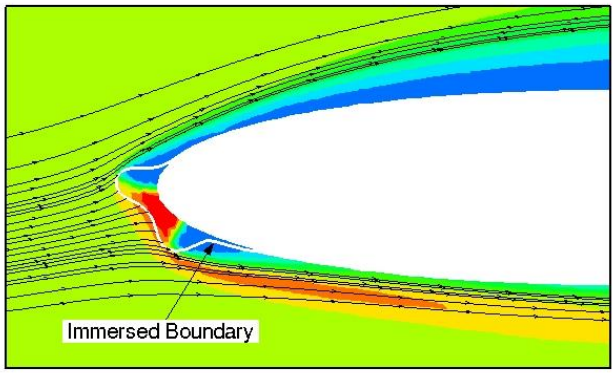

Figure 11 - Example for the Penalized trajectography (Traj2D), volume fraction of water and droplet velocity streamlines

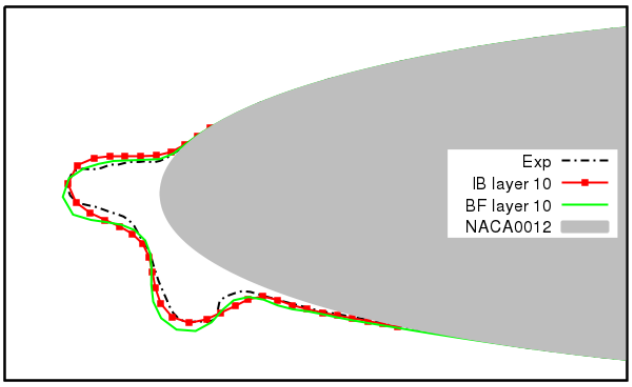

Figure 12 - Example of calculations with IGLOO2D on a glaze-ice case: comparison of immersed boundary method (IB) against the standard body-fitted (BF) approach (based on remeshing). Multi-step approach employed with 10 layers.

3.2.1.1.3 Conclusions

The IB literature on the ice-accretion topic is relatively young. This implies an open research field that is prone to new ideas, physical models and numerical schemes able to work within the current IB tools. Pure immersed boundary and embedded level-set methods have the potential to grow towards "all-in-one" ice-accretion systems able of automatize and speed-up the entire ice-simulation chain. The IB simulation of water droplet impingement seems a minor issue due to recent and successful developments. The key research area, for IB tools, seems the water-film topic. Multilayer approaches are promising but they are currently in the early stages of research and only developed in the framework of body-conforming methods.

Likely, during the ICE-GENESIS Project, the major IB developments will come from the coupling between the IB water-droplet impingement and existent/new multilayer film models.

3.2.1.1 Mesh deformation [POLIMI, CIRA, TUDA]

3.2.1.1.1 Objectives and issues

Ice accretion over realistic aircraft geometries over long ice exposure times usually results in complex ice shapes, whose influence on the aerodynamic flow field is key to determine the further accretion of ice over the aircraft surface. It is therefore necessary to modify the computational mesh, including the surface mesh, to comply with the new geometry. The new computational surface and domain meshes can be produced from scratch, similarly to the initial mesh for the clean surface. Mesh generation is quite a difficult task in this case, due to both the complexity and non-smoothness of the accreted surfaces and the complex topology of the same, which can be multiply connected or scattered over the surface (Figure 13, Figure 14).

As an alternative, one can take advantage of the existing computational mesh and modify it to comply with the new geometry. A typical technique is to deform the mesh from the initial geometry to the new one, possibly allowing some changes in the mesh connectivity or adding/deleting mesh points to comply with quality constraints. Similar techniques can be applied to the numerical simulations of the impact of particles on a liquid-gaseous interface and the modelling of crystallization and evaporation processes.

In the present section, a literature review is carried out moving from the EXTICE, HAIC and STORM projects, to investigate recent advancements in mesh deformation techniques

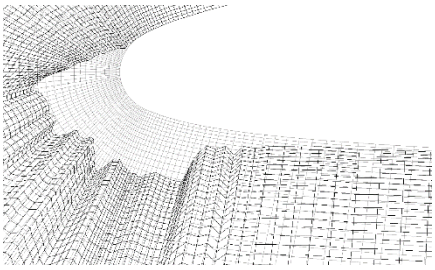

Figure 14 - Mesh deformation in 2D over the leading edge of an airfoil using the IDW scheme of Shepard. The grey lines represent the initial mesh, the black ones the final mesh including the accreted ice shape.

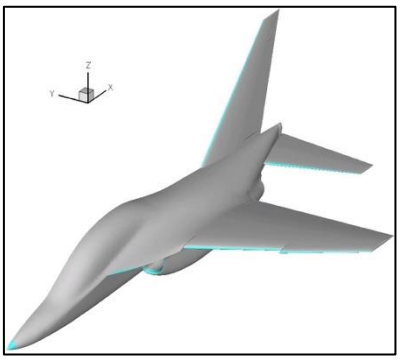

Figure 13 - Typical ice accretion regions over a complete aircraft configuration

3.2.1.1.2 Literature review

3.2.1.1.2.1 Mesh deformation for multi-step ice accretion on 3D surfaces

3.2.1.1.2.1.1 Description

Different techniques can be used to alter the mesh geometry and connectivity to comply with the new, accreted geometry in complete 3D aircraft configurations. For relatively smooth ice accretion shapes that do not alter the topology of the geometry, simple mesh displacement techniques, based on e.g. the elastic analogy, can be applied in a straightforward manner. As an example, in Figure 13, the Inverse Distance Weighted interpolation (IDW) technique of Shepard [24] is used to alter the initial mesh on the leading edge mesh of a 2D airfoil to comply with the accreted ice. The weights are inversely proportional to the 2nd power of the distance d between grid points. The technique can be

applied to 3D geometries as well, though in the latter case, more care is necessary to avoid invalid meshes [25].

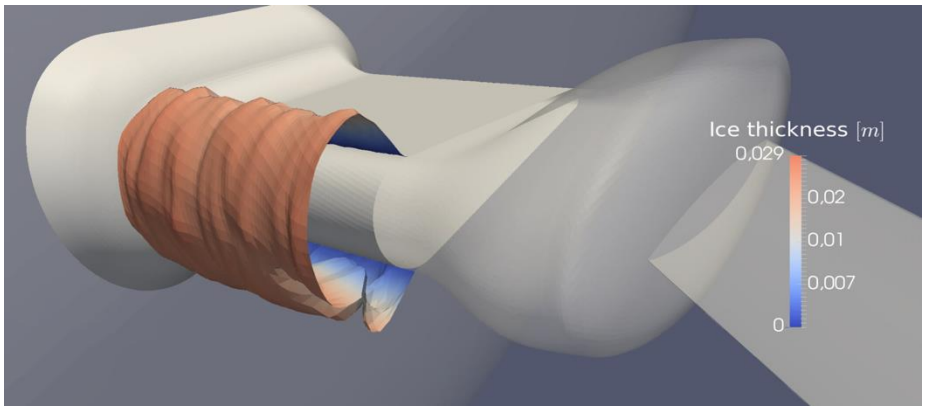

Figure 15 - 3D ice accretion over the stem of a pitot tube. The 3D mesh was modified to comply with the new iced geometry using the IDW method.

3.2.1.1.2.1.2 Main results, progress and limitations

Figure 15 shows the 3D ice accretion over the stem of a pitot tube. The resulting ice geometry is quite complex and the corresponding computational grid is obtained by applying the IDW technique to the underlying tetrahedron meshes, with no changes in the connectivity or the number of nodes. This approach presents strong limitations for complex 3D geometry and often fails to preserve the validity of the mesh. A more general technique can include connectivity changes (edge swapping, local remeshing) similarly to what is done for dynamic mesh simulations [26].

An example is given in Figure 16, where the MMG mesh alteration tool [27] is used to displace a 3D mesh around a wing-section of one chord forward [28]. Mesh displacement, deformation and adaptation can be used to create a high-quality mesh around complex geometry, though the computational complexity can be quite high. The availability of mesh alteration tool like MMG greatly simplifies the task.

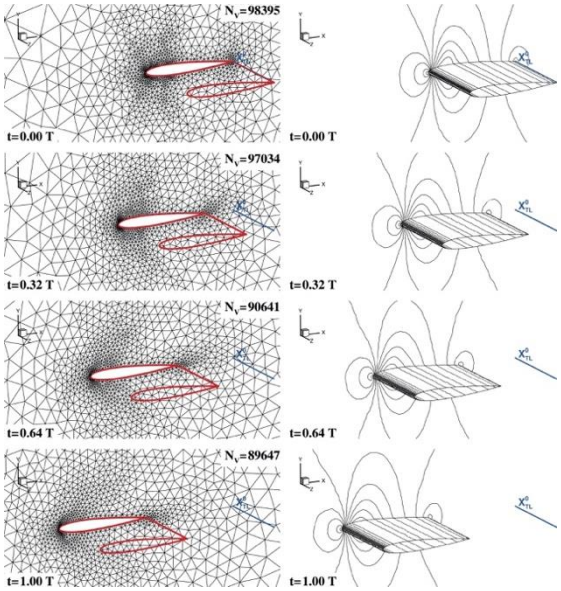

Figure 16 - Mesh deformation and adaptation can be used to comply with large domain deformation. Here a 3D wing section is displaced by one chord.

3.2.1.1.2.2 Mesh deformation for the impact of particles on a liquid-gaseous interface

3.2.1.1.2.2.1 Description

In the scope of the European collaborative research project HAIC the impact of solid particles onto a liquid gaseous interface is studied numerically with OpenFOAM, using the dynamic VOF-solver *InterDyMFoam* with an implemented mesh motion and deformation [29] [30]. Within the computational domain the solid particle is not part of the discretized domain, instead its dynamic imposes a boundary velocity on the domain and initiates a mesh motion. The dynamic of the particle

is determined by the momentum and the moment-of-momentum equations which take into account the forces and torques acting on the particle boundary due to surface tension, viscous, and inertial effects from both fluid phases and gravity. For this purpose a dynamic mesh library is implemented in the *InterDyMFoam* solver which executes mesh motions (stretching and compressing of the mesh) due to the particle dynamics.

The numerical study [29] [30] is performed for the water impact of non-rotating and rotating rigid spheres for various impact angles and impact Weber numbers based on the velocity, diameter and density of the rigid sphere and the surface tension of the liquid interface. For the axisymmetric non-rotating case the mesh deformation is applied on a two-dimensional mesh, while for the rotating case a three-dimensional mesh is employed since it is no longer axisymmetric.

3.2.1.1.2.2.2 Main results, progress and limitations

The numerical simulation in combination with the mesh deformation works fine for both non-rotating and rotating cases. The simulation results are validated by experimental data and found to be in very good agreement both qualitatively (evolution of cavity shape created by the motion of the sphere in the liquid) and quantitatively (trajectory of the particle). Even for low Weber numbers, where the influence of capillary forces is much more dominant, the results of the numerical simulation agree very well with experimental data for different type of wettability. For this reason, the applied solver with implemented mesh deformation is a valid method to simulate the impact of particles on a liquid-gaseous interface. Figure 17 shows the organization of the mesh and its local refinement. Gray lines correspond to the mesh before movement and one can see five meshing zones from the sphere sur face up to the farthest boundary (large rectangle). Black lines represent the mesh altered to account for the particle movement. Refined areas, shown as gray shaded surfaces, are moved but not distorted while the white area between the gray regions and the boundary of the bounding box is compressed and stretched.

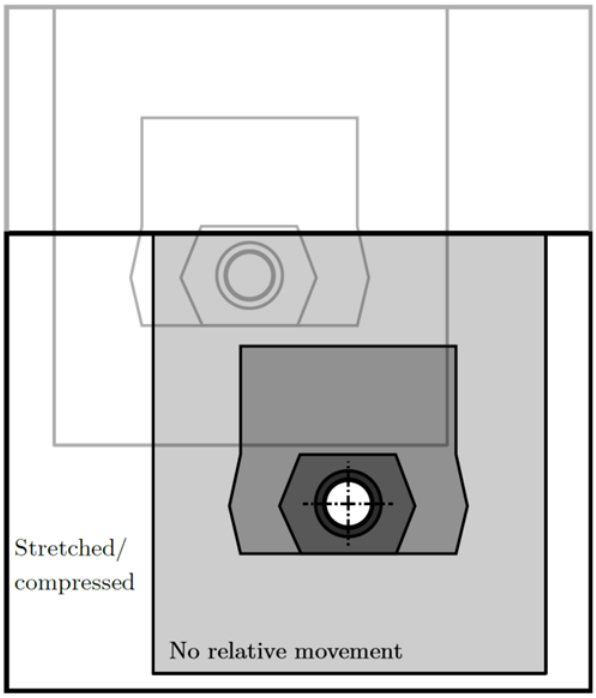

Figure 17 - Mesh deformation and its local refinement: deformation due to stretching and compressing.

Nonetheless, the mesh deformation performed in these simulations is limited by various criteria. One limitation is that only the impact of solid particles can be treated with this method, since the particle is not part of the discretized domain. Therefore, deformation of the particle cannot be resolved with the present method. Furthermore, the particle must be spherical due to symmetry aspects. For different types of non-spherical particle, the dynamic mesh Library must be expanded.

3.2.1.1.2.3 Mesh deformation for the modelling of crystallization and heat transfer in an evaporating urea-water drop

3.2.1.1.2.3.1 Description

In the scope of the German collaborative research project SFB TRR-150 the evaporation and deposit formation of urea-water drop on an initially smooth surface is numerically modelled in [31] by using the finite element method (FEM) in a moving mesh framework. The deformation of the liquid-gas interface is resolved using an Arbitrary-Lagrangian-Eulerian Method (ALE). The models were built in the COMSOL Multiphysics program. The heterogeneous crystallization of the urea on the wall is implemented by the deformation of the computational grid, so that the reaction of the deposits on the droplets is reproduced (Figure 18). When the mesh distortion exceeds a threshold value, the calculation is stopped and the deformed geometry is remeshed automatically. The big advantage is that the computational grid follows the shape of the phase boundary and the deformation of the grid finally represents the deposition (crystallization) of the urea-water drop.

3.2.1.1.2.3.2 Main results, progress and limitations

The present computation allows describing the evaporation of a multicomponent system. In addition, the concentrations and temperatures at the phase boundary are known, so that a reconstruction of the values at the phase boundary can be omitted. Due to the exact resolution of the phase boundary, an implementation of Marangoni flows is possible. The evaporation behavior of the droplet in the model was successfully validated on the basis of values from the literature and of experimental measurements.

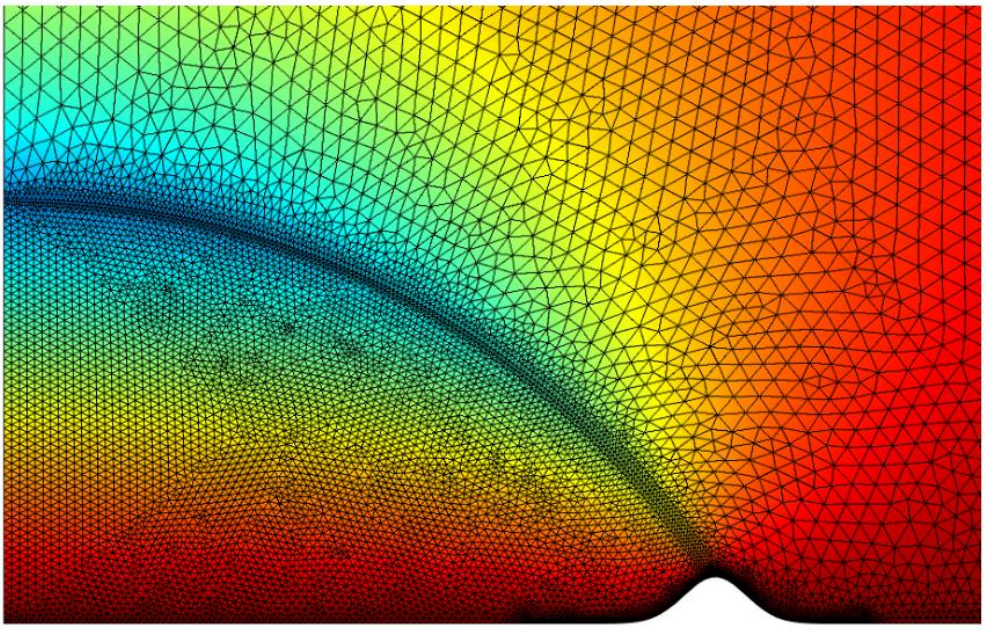

Figure 18 - Obtained by [31] in the framework of the SFB-TRR150: "Drop shape during the process of evaporation and deposit formation. The mesh is refined in the vicinity of interface. The bump-shaped wall deformation corresponds to deposit. The colour map represents the temperature field " (Reprint).

3.2.1.1.2.4 Mesh deformation by Radial Basis Function

3.2.1.1.2.4.1 Description

Radial Basis Functions (RBFs) are a powerful mathematical tool for data interpolation/regression. Three main branches of application can be identified: RBFs for approximation of given functions (time series prediction and control of non-linear functions), RBFs for meshless approximate solution of PDEs and RBFs for computational mesh deformation in support of fluid-structure interaction, shape optimization and multi-physics. With reference to the latter application, in Computer Aided Engineering (CAE), RBFs are used to modify (deform) the discretized domain according to the displacements of a set of source points [32] [33] [34]. The deformed mesh will be then driven by and consistent with the imposed displacement field. The main features of such methodology are here listed [35] [36] [37] [38]:

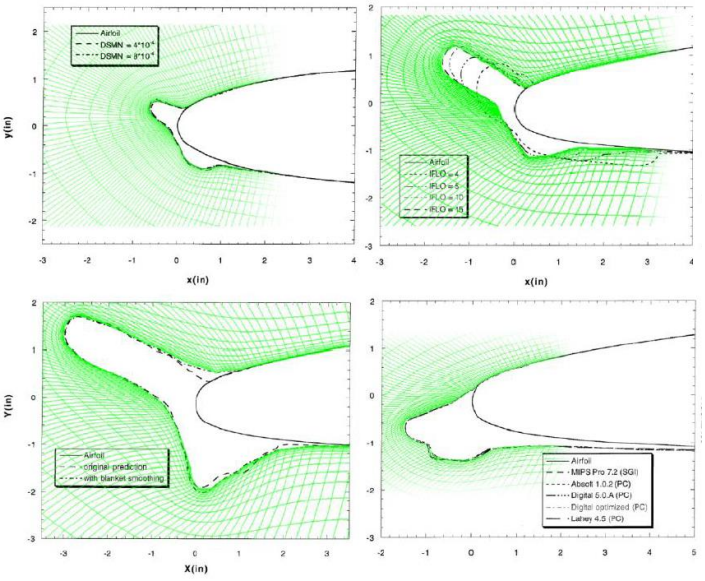

Figure 19 - Example of RBF mesh morphing with fully accreted literature ice shapes

- meshless method, *i.e.* does not require connections between nodes and can be applied to any mesh structure;

- mesh consistency, i.e. the deformed mesh will have the same topology than the original mesh and the mesh points will move in relation to their distance from the source points. If a mesh point coincides with a source point, it will move exactly as the source point;
- avoidance of noise typical of re-meshing techniques;
- easy to integrate into a computational chain;
- capability to treat large meshes with high performance and low memory usage.

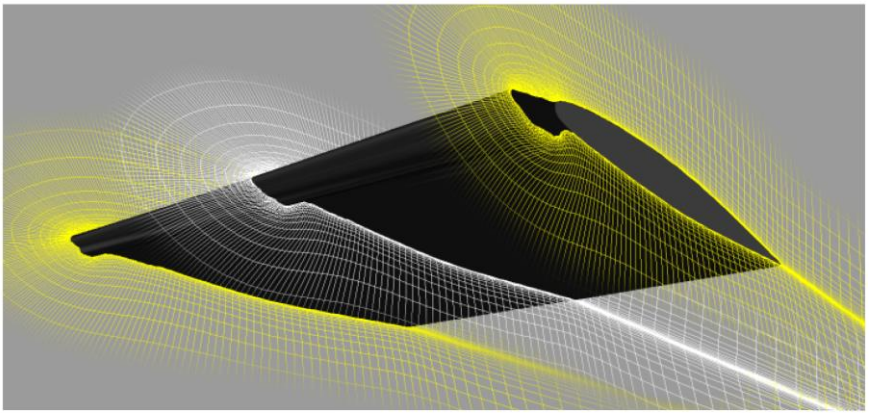

Figure 20 - Mixed accretion on a 3D wing shape

Recently, the RBF mesh morphing technique has been the major technology of the RBF4AERO Project (European Commission, 2013) which aimed at developing the RBF4AERO Benchmark Technology, namely an integrated numerical platform and methodology to efficiently face the most demanding challenges of aircrafts design and optimization [39] [40]. Within this project, the use of RBFs has been extended to icing applications [41] as an ideal tool for the grid generation problem.

3.2.1.1.2.4.2 Main results, progress and limitations

Within the RBF4AERO project, two approaches were developed for icing mesh morphing procedures: the constrained or frozen approach and the evolutionary or “on-the-fly” approach. In the former the ice growth profiles are computed before the morphing phase (e.g., by using an ice accretion tool or literature shapes) and applied to the CFD model at specific simulation times. The latter, instead, foresees that the CFD model is coupled with an ice accretion model which drives the source points displacements according to the CFD results in an on-line manner.

Characterized by a high level of automation, verification tests were focused on checking the correct functionality as well as the capability of local control and high accuracy, which is a fundamental requirement in ice accretion studies. Compared with the standard adopted approach (i.e. remeshing of each configuration), in the pre-processing phase of the most challenging case (3D icing in constrained mode) the RBF4AERO procedure allowed a time saving of 90%, since there is no need to prepare a CFD model for each configuration, only the baseline one is needed and, of course, the RBF solutions to morph the mesh. Figure 19 and Figure 20 show some examples of RBF morphing on 2D and 3D cases. Figure 19 depicts the RBF-based mesh deformation applied to literature icing cases, including thick ice accretions and horn shapes. Figure 20 shows a deformed three-dimensional mesh around an iced wing section with different icing conditions along the span. The geometry is 2D (extruded), but the accretion is 3D as icing conditions have been varied along the span, so also the mesh deformation is 3D.

3.2.1.1.3 Conclusions

In this section, a review was presented on mesh deformation for multi-step ice accretion on 3D surfaces, to study the impact of particles on a liquid-gaseous interface and for modelling of crystallization and heat transfer in an evaporating urea-water drop. Both unstructured- and structured-grid approaches were presented, the latter relying on Radial Basis Function deformation techniques. For unstructured meshes, differently from the simpler two-dimensional case, it is apparent that mesh movement involves also the introduction and/or the deletion of the grid nodes and elements, to preserve the local mesh qualities. Therefore, in three spatial dimensions, mesh deformation algorithms do not differ from those required to perform mesh adaptations, as discussed below, and they entails the same computational complexity.

3.2.1.1 Automatic re-meshing [ONERA, TUDA]

3.2.1.1.1 Objectives and issues

Ice accretion calculations are based on successive calculations of the airflow and the trajectories of water droplets around the iced obstacle, and finally of the mass and energy balance of the water deposited on that surface. Then, the ice growth changes the fluid volume, which in turn affects the airflow and the water droplet trajectories. To take this effect into account, it is possible to re-mesh the fluid volume. The automatic re-meshing approach is often used in 2D ice accretion suites [2]. However, in 2D codes, there is a gain in geometric simplicity compared to 3D codes. Also, aerodynamic calculations are often based on an inviscid code, which is not very restrictive for cell quality in the vicinity of walls (there is no need for orthogonal and very fine cells like in boundary layers).

In 3D, it is sometimes possible to use methods of the same type as in 2D. But the issues of the robustness of the methods, the number of cells generated and the quality of the near-wall mesh for Navier-Stokes approaches are to be discussed.

3.2.1.1.2 Literature review

3.2.1.1.2.1 Methods generally used in 2D icing suites

3.2.1.1.2.1.1 Description

There are many meshing methods, both structured and unstructured, in the literature. The unstructured methods should allow to automatically generating 3D grids rather easily, at least on the basis of tetrahedral elements. Such methods are often used in 2D icing suites like IGLOO2D [2] where the grid generation code GMSH is used to make grids for inviscid computations. 3D ice accretion calculations are often based on the resolution of Navier-Stokes equations. For these calculations, structured grids are often used or prismatic layers are included near the walls. A method allowing to make unstructured grids for Navier-Stokes simulations, which has not yet been used for ice accretion applications, will be discussed in section .3.2.1.1.2.1.2

Hasanzadeh's PhD thesis [42] presents a literature review on structured mesh generation methods used in 2D icing suites or that can be used. In particular, it appears that several methods used in 2D icing codes are based on parabolic methods (e. g. the method used in Thompson and Soni's ICEG2D solver in LEWICE [43], or the method used in NSGRID2D [44]). The parabolic method consists of iteratively propagating the grid from the body. The grid is often smoothed by solving a Poisson equation with well-chosen source terms (elliptic method). Besides, a hyperbolic method is available in IGLOO2D [2] (for inviscid calculations however). The hyperbolic method solves a hyperbolic system of equations for the coordinates of the grid nodes (the equations are inferred from conditions on orthogonality and cell size). Conformal mapping methods such as the iso-parametric mapping are other solutions proposed in IGLOO2D [2] for instance. A mapping between the Cartesian coordinates of a parametric space and the curvilinear coordinates of the real space is defined. The grid quality of such a method is not always ensured in the vicinity of boundaries with large curvature.

Among the aforementioned approaches used in 2D, some were extended to 3D. The parabolic method described hereafter was indeed used for 3D icing applications with NSMB3D-ICE (and the grid generator NSGRID3D, see [45]). It should be noted that it is also possible to extend the hyperbolic method to 3D [46].

3.2.1.1.2.1.2 Main results, progress and limitations

Thompson and Soni's method mainly presents difficulties in concave areas (grid clustering or even grid shock like in Figure 21) and in the outer boundary definition. Additionally, the grid quality may be altered near sharp corners. Handling multi-element bodies as well as multi-blocks is also an issue. The method proposed and implemented in NSGRID by Hasanzadeh is also based on the parabolic method. But elliptical methods are added for grid smoothing (a blended approach combining Sorenson (RLS) and Spekreijse (SPS) methods) [44]. The method thus allows to improve the treatment of concave areas and to better control the grid quality in the whole field. It was also used in a multi-block approach. It is interesting to note that the method was also used in 3D, as illustrated in Figure 22.

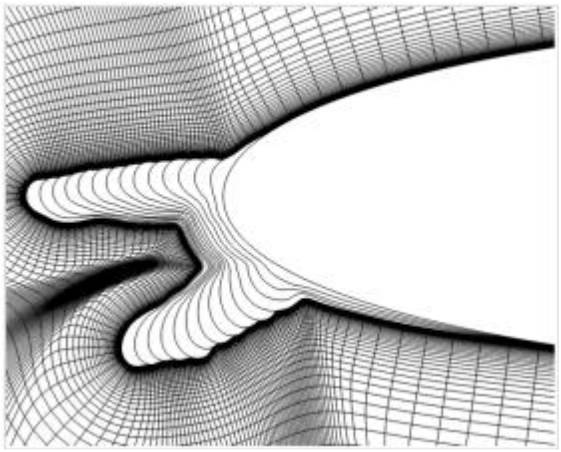

Figure 21 : Grid shock obtained with parabolic method in the concave area between two horns. Picture extracted from [42]

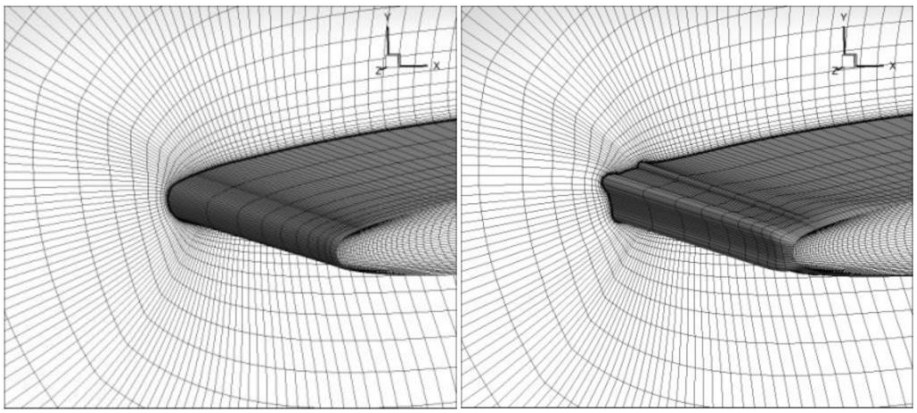

Figure 22 : Example of automatic mesh generation with NSGRID3D (blended parabolic/elliptic method combining Sorenson and Spekreijse approaches for elliptic smoothing)

However, there may still be issues about the robustness of hyperbolic and parabolic 3D methods for internal geometries for example (or applications with outer boundary conditions other than far-field conditions).

3.2.1.1.2.2 DRAGON and cut-cell methods present in Cassiopee software

3.2.1.1.2.2.1 Description

In reference [47], Vuillot et al employed the Cassiopee software to create unstructured grids for aeroacoustics simulations around a landing gear. Although the purpose of this study is not icing, there are several interesting points to be noted. The method allows automatic re-meshing. The studied geometry is 3D and relatively complex (Figure 23). Navier-Stokes calculations are performed. The question of a reduction in the number of cells is addressed. Finally, two approaches are compared.

Additionally, solvers used by ONERA like CEDRE were used in [47] and ONERA will be working on re-meshing in the ICE-GENESIS project.

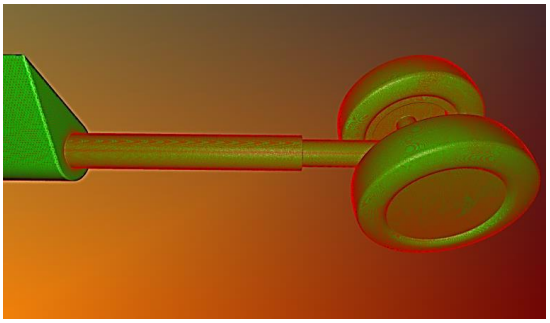

Figure 23 : The so-called LAGOON landing-gear model investigated by Vuillot et al [47]

The first method is the so-called DRAGON method, originally developed by Kao and Liou [48]. A surface geometry or a surface mesh is first read by Cassiopee. Then, prismatic layers are generated from the surface mesh, which allows refined high-quality grids in the boundary layer. In the far-field, an octree grid is automatically created by Cassiopee, which allows for coarse grids in regions where gradients are low. The "merging" of the two kinds of grids is then made by, first, blanking the octree grid around the prism layer and, second, filling the hole with tetrahedra (the open-source TetGen tool is integrated in Cassiopee). Finally, the whole mesh is converted into a conformal polyhedral representation.

The second method employs the cut-cell approach to merge the prism layer and the octree mesh [49]. The intersection of octal cells and prisms generates new cells. Some cleaning must be done to avoid poor quality cells (complex cell shapes, very small cells, etc.).

3.2.1.1.2.2.2 Main results, progress and limitations

The article [47] showed that there are three kinds of grids which can be generated by Cassiopee, and it is possible to perform complex manipulations and combinations of these three types of meshes.

The DRAGON method proved efficient and robust [47]. Very good quality cells were obtained in the vicinity of the walls (with $y^+<1$). Figure 24(a) shows an illustration of the kind of grids which was generated. The major flow structures were well captured with the automatically generated grid with a number of cells almost reduced by two, compared to previous simulations with classical unstructured grids. However, it is worth mentioning that there are numerous tetrahedra in the assembled mesh (around 30% of the cells in the LAGOON test-case investigated in [47]).

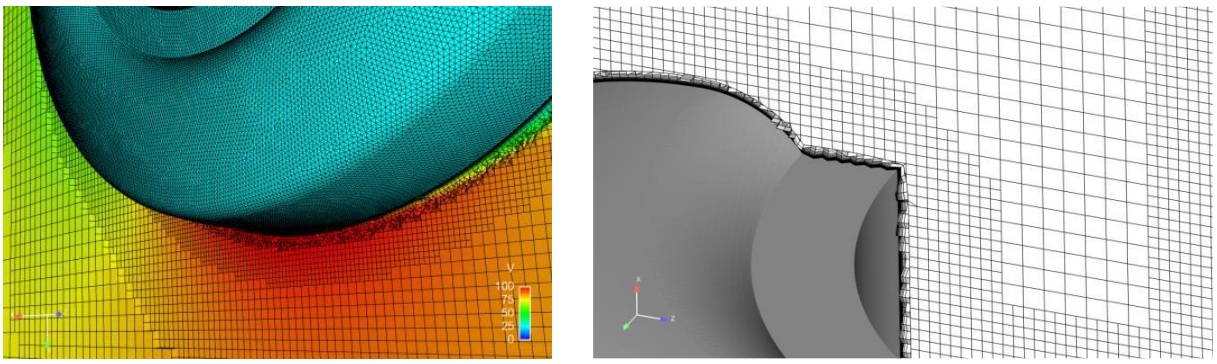

(a) DRAGON method *(b) method based on cut cells*

Figure 24 : Grids obtained with the DRAGON method and the method using cut cells [47]

The “cut-cell” approach attempted to save on the cell count by removing the tetrahedra. Some grids could be generated with this method (Figure 24(b)). However, the mesh could not be used efficiently with CEDRE. Very small time-steps were indeed required. The method generates some very small polyhedral cells, some concave cells and some very high aspect-ratio cells which reduce the code efficiency. Most of the problematic cells could be fixed (around 90%). However, some work was still needed to completely eradicate the ill-formed cells. These problems have been addressed in a very recent article [50].

Additionally, it is worth mentioning that the CEDRE solver deals with generalized polyhedral grids. This allows the use of cut cells with any number of faces, but not all Navier-Stokes solvers are compatible with this approach.

3.2.1.1.2.3 2D and 3D adaptive mesh refinement in combination with dynamic load balancing

3.2.1.1.2.3.1 Description

In the scope of a German research collaboration of different groups (SFB-TRR 75 & SFB-TRR 150) at the TUDA, 2D and 3D adaptive mesh refinement in combination with dynamic load balancing has been implemented in the open-source CFD package OpenFOAM [51] [52] [53] [54]. The dynamic adaptive mesh refinement (AMR) technique allows increasing locally the mesh resolution at the interface and thus reducing the overall number of cells in the domain as well as the total computation time. The AMR in OpenFOAM is based on the class hexRef8 which performs mesh cutting operations to split the original hexahedral cell in each direction and thus into eight cells of equal size [52] [54].

3.2.1.1.2.3.2 Main results, progress and limitations

Due to the dynamic load balancing, a significant increase of the speed-up in comparison to the speed-up without load balancing has been achieved and demonstrated. Dynamic load balancing means that the re-distribution of the mesh is done ‘on the fly’ during the simulation. Figure 25 schematically

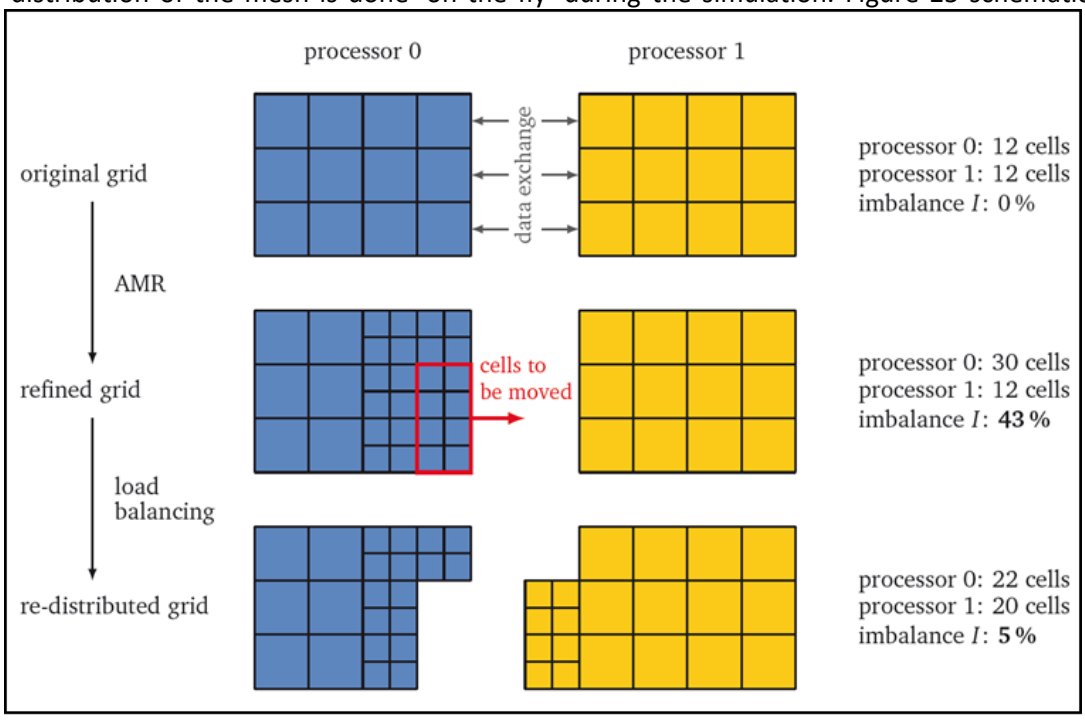

Figure 25 - Illustration of the load balancing procedure in a parallel computation with AMR

illustrates the automatic mesh refinement with the dynamic load balancing procedure. The developments are of relevance for OpenFOAM's transient top-level solvers for incompressible flow. Due to its modular design, the implementation can be readily used for various applications.

3.2.1.1.3 Conclusions

There are many methods in the literature regarding re-meshing. The present literature review is far from comprehensive. This review mainly presents some techniques usually used in 2D and some recent advances (made especially with tools developed at ONERA). It seems possible to extend the methods used in 2D to 3D. However, there may be some restrictions when dealing with confined geometries rather than far-field environments. There could also be limitations for Navier-Stokes approaches around very complex ice shapes.

Some methods may be tested as part of the ICE-GENESIS project. Emphasis will be placed on the ability to generate meshes in a robust way, in order to allow easy use in automatic icing suites. The issue of the number of cells generated may be addressed, so as to allow reduced computational costs. As 3D Navier-Stokes solvers are targeted as a priority, the quality of the near-surface mesh should be ensured by the use of prismatic layers. Some issues regarding the nature and quality of the grid cells generated by the method(s) studied will need to be discussed. The targeted codes of the ICE-GENESIS project have their own restrictions in terms of required quality and accepted cell types. The re-meshing techniques selected will have to be adapted to these restrictions. The cut-cell approach for instance may not be accepted by any Navier-Stokes solver although solvers like CEDRE or elsA may however be available.

Finally, some robustness issues for the re-meshing of very complex ice shapes may need to be addressed during the project.

3.2.2 Roughness[1]

3.2.2.1 Conclusions from STORM [ONERA]

3.2.2.1.1 Main results

As already described earlier (in Sec. 3.2.1.1), the work-package 4 of the STORM project was dedicated to the development of 3D numerical tools suitable for simulations of ice accretion in aero-engines.

Besides, the usual approach in icing codes is generally based on integral boundary layer methods. For instance, this method was employed in HETEMS. It is also available in codes like LEWICE2D or IGLOO2D [2]. It consists of computing the integral boundary layer quantities and relating the heat transfer coefficient to these quantities and the equivalent sand-grain roughness height k_s (section 4.2.4.2.2).

In the STORM project, the integral boundary layer method was replaced by an unstructured RANS code both in CEDRE and OpenFOAM. Some models are available in the codes for the impact of roughness on heat transfer (see section 4.2.4.2.3 for the model available in CEDRE). Some simulations performed with CEDRE during the STORM project produced a level of heat transfer coefficient similar to that produced by the integral method of IGLOO2D. One test-case was investigated for that purpose (Figure 26). However, the easiest way to achieve this objective was to disable the thermal correction and use the same value in $k_s=c/1000$ as in IGLOO2D (for an airfoil of chord c). Additionally, $k_s=c/1000$ is often employed in IGLOO2D, but it is a rough estimate of the equivalent sand-grain roughness height (which often produces rather correct ice shapes, as shown in Figure 26 (a)).

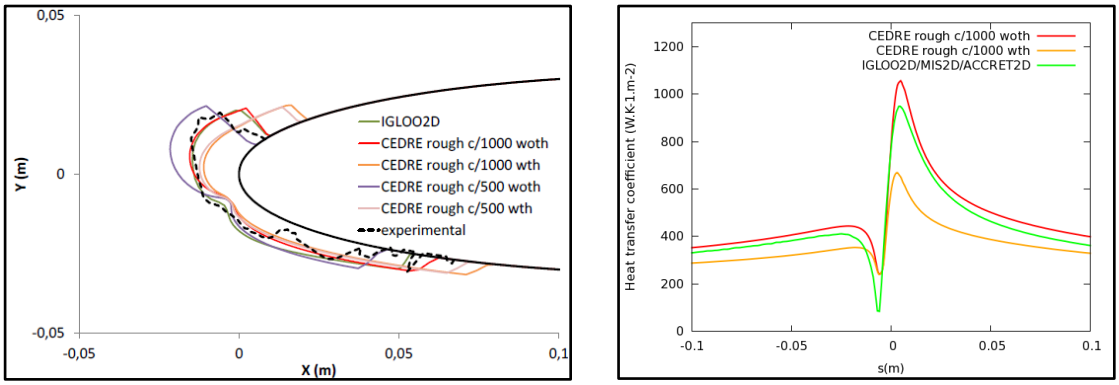

(a) ice shapes

(b) heat transfer coefficient

Figure 26 - NACA0012 test-case of the STORM D4.8 public report [1]: parameters of the roughness model for the RANS code CEDRE (woth: thermal model disabled, wth: thermal model enabled), comparison against IGLOO2D run with the integral boundary layer method fed with $k_s=c/1000$

3.2.2.1.2 Lessons learned, limitations and perspectives

Several issues were reported regarding the impact of the surface roughness on the ice accretion process but not resolved during the STORM project [1]. In particular, the impact of roughness on the heat transfer only was considered, whereas roughness can also affect the water runback dynamics (wall skin friction, development of rivulets, retroaction on roughness heights and airflow, etc.). Very detailed approaches such as DNS or the multi-scale approach of Rothmayer [55] are necessary to

[1] For the roughness characterization, refer to "Characterization of surface roughness", T.R. Thomas, Precision Engineering (1981), or "Roughness parameters", E.S. Gadelmawla *et al.*, Journal of Materials Processing Technology 123 (2002).

capture all phenomena. Simplified models could be inferred from these simulations, which requires a huge effort and could not be made in the framework of the STORM project.

Concerning the RANS approach, there is less experience in the use of such models for icing. Firstly, the laminar-turbulent transition should be modelled, which is more complex than in integral boundary layer methods. Secondly, the model of section 4.2.4.2.3 is more evolved than the one of section 4.2.2.2.2, but there are three parameters (k_s, the mean roughness height k and the corrected surface S_{corr}) instead of one (k_s). The new parameters must thus be characterized.

A finer assessment of k_s and a characterization of k and the corrected surface S_{corr} are expected in the ICE-GENESIS project to make the RANS approach available with thermal correction enabled.

3.2.2.2 Roughness characterization for App C [ONERA, CIRA, TUDA, TUBS, POLIMI]

3.2.2.2.1 Objectives and issues

The ice roughness has a major impact on the convective heat transfer, which is a key parameter for ice accretion modelling. Thus, it is important to characterize the roughness size and distribution to feed the ice accretion codes.

The following sections will give an overview of the roughness-size models available in the literature. There are several types of roughness size models in the literature. The simplest models, such as the ones successively implemented in LEWICE by Ruff, Shin and Bond and Wright or the one implemented in ONERA's codes, provide a constant and uniform roughness thickness, depending on icing conditions. The Han and Palacios, and McClain models provide a spatial and temporal evolution of the roughness, always in relation to global icing conditions.

3.2.2.2.2 Literature review

3.2.2.2.2.1 Constant roughness models: Equivalent sand-grain models

The simplest roughness height model is the ONERA's model, used in the IGLOO2D and IGLOO3D codes (as well as in ONICE2D and ONICE3D). Since the experimental characterization of roughness size is not complete, a constant and uniform value is employed for the equivalent sand-grain roughness height k_s, which is related to the chord length, c as follows [56]:

$$k_s = \min(\max(\mathrm{c}/1000; 0.2\mathrm{mm}); 1.5\mathrm{mm}) \qquad \textit{Equation 1}$$

The models of Ruff, and Shin and Bond and the investigations of Anderson confirm the trend that obstacle size is indeed a first-order parameter (for chord lengths studied in the range of 0.267 m to 0.8 m).

Ruff [57] proposed the following model for the equivalent sand-grain roughness height in LEWICE:

$$k_s = 0.00117 \times \mathrm{c} \times \mathrm{f}_{k,LWC}(\mathrm{LWC}) \times \mathrm{f}_{k,T}(T_\infty) \times \mathrm{f}_{k,V}(V_\infty) \qquad \textit{Equation 2}$$

$$\text{where } \mathrm{f}_{k,LWC}(\mathrm{LWC}) = 0.5714 + 0.2457 \times \mathrm{LWC} + 1.2571 \times LWC^2$$

$$\mathrm{f}_{k,T}(\mathrm{T}) = 0.0468\mathrm{T} - 11.2037$$

$$\mathrm{f}_{k,V}(\mathrm{V}) = 0.4286 + 0.0044139\mathrm{V}$$

This model was obtained by retro-engineering in order to best reproduce the ice shapes of a database generated by Gent and co-authors with LEWICE (mainly NACA0012 profiles of 0.30 m chord length and possibly RAE profiles). In addition to the chord length, it takes into account the effect of the liquid water content LWC and the static temperature T_∞ as well as the air velocity V_∞.

Shin and Bond used a similar retro-engineering approach based on the ice shapes obtained by Olsen et al [58] on a NACA0012 of 0.53 m chord. They also relied on the few photographic observations of the latter about the shape of the rough elements. In particular, Olsen et al confirmed the influence of temperature, minimized that of velocity and pointed out that the diameter of the impinging droplets (MVD_∞) could have an influence. Shin and Bond [59] therefore proposed to correct the Ruff model as follows:

$$k_s = 0.6839 \times 0.001177 \times \mathrm{c} \times \mathrm{f}_{k,LWC}(\mathrm{LWC}) \times \mathrm{f}_{k,T}(T_\infty) \times \mathrm{f}_{k,D}(MVD_\infty) \qquad \textit{Equation 3}$$

$$\text{where } \mathrm{f}_{k,T}(\mathrm{T}) = 0.047\mathrm{T} - 11.27$$

$$\mathrm{f}_{k,D}(\mathrm{D}) = \begin{cases} 1 \; if \; D \leq 20\mu m \\ 1.667 - 0.0333\mathrm{D} \text{ otherwise} \end{cases}$$

Since the order of magnitude of the functions $f_{k,LWC}$, $f_{k,T}$, $f_{k,V}$ and $f_{k,D}$ is 1, the magnitude of Equation 1 is well respected.

However, Equation 3 seems to have limited validity in terms of LWC (it was built for LWC less than 1g/m^3). Shin [60] studied the influence of LWC, temperature, flow velocity and the accretion time on the shape of the roughness (height, diameter, spacing, smooth zone extent) for droplets 20 µm in diameter. He confirmed that velocity has a negligible influence on the roughness size. He also showed that Equation 2 significantly overestimates the roughness size, even for LWC less than 1g/m^3.

As shown in section 3.2.2.2.2.2, Anderson *et al.* proposed to correlate the roughness size no longer with dimensional parameters but with the "classical" dimensionless icing parameters, in particular the freezing rate f_0 near the stagnation point and the accumulation parameter A_c. They found that f_0 could have little influence on the roughness size. Wright [61] maintained the use of non-dimensional parameters but, contrary to Anderson, he made the equivalent dimensionless sand grain roughness height depend on f_0 in LEWICE 3.2:

$$k_s = \frac{c}{1000}\frac{1}{2}\sqrt{0.15 + 0.3/f_0} \qquad \textit{Equation 4}$$

This dependence makes k_s 35% greater for f_0=*0.2* than for f_0=*0.4*, which is a greater influence than that observed by Anderson and Shin [62].

3.2.2.2.2.2 Constant roughness models: experimental characterization

In order to gain in physical representation, Anderson and Shin [62] used experimental characterization (camera acquisition). They investigated Shin's data [60] in more detail, proposing to correlate them no longer with dimensional parameters but with the "classical" dimensionless icing parameters, in particular the freezing rate f_0 and the accumulation parameter A_c.

$$A_c = \frac{V_\infty \times LWC \times \tau}{\rho_i \times 2r_0} \qquad \textit{Equation 5}$$

τ is the exposure time to the icing cloud, r_0 is the radius of curvature at the leading edge and $\rho_i = 917$kg/m^3 is the ice density. Since most of the investigated data correspond to glaze ice accretion, this value is representative of the ice density.

The authors reported that, depending on the size of the drops on the wall relative to the thickness of the boundary layer, and depending on the rate of solidification, the shear stress applied to the sessile droplets could affect the roughness size. But they neglected this effect in the papers [62] and [63], by not considering any dimensionless numbers related to the boundary layer.

Since there were too few data from Shin's campaign, Anderson et al [63] completed this study in 1998. They performed a parametric study on the chord length, A_c and f_0, still investigating a NACA0012 with angle of attack AOA=0°. The chord length investigated in [62] was 0.5334m, whereas it was varied in the range 0.267 m to 0.8 m in [63]. For several sets of LWC, V_∞, MVD_∞ and T_∞, Anderson also made a variation on τ. There are similar conclusions in both test campaigns. In particular, above a given value of A_c, $A_c \geq A_{c,lim}$, a constant value of the roughness diameter is reached (as well as the size of the smooth zone mentioned below). Anderson introduced the notion of "plateau" to name that. The limit diameter Φ (which is therefore reached after a given accretion time determined by $A_c \geq A_{c,lim}$ and measured on pictures) is:

$$\Phi = 0.06 \times 2\mathrm{r}_0 \approx 1.9 \times 10^{-3} \times \mathrm{c} \Longrightarrow \mathrm{k} \approx 0.981 \times 10^{-3} \times \mathrm{c} \qquad \textit{Equation 6}$$

where k is the rough element thickness, which was found to be related to the rough element diameter as $\mathrm{k} = 0.515\Phi$. The correlation for k is thus very similar to the ONERA's correlation for k_s (Equation 1) although their definition is not the same.

However, with Shin's data, $A_{c,lim}$=0.15 [62] while with more recent data, $A_{c,lim}$=0.4 [63]. In addition, in [63], f_0 has no impact on the geometry of the roughness, while the diameter is 20% larger for f_0=*0.2*

than for $f_0=0.4$ with Shin's data. However, it should be noted that there is a large dispersion of results and some repeatability errors in the results of [63].Note that if the size of the rough elements depends only on A_c, the velocity and LWC will have more effect than temperature on the rough element size (before the “plateau”).

Finally, to draw a parallel with McClain more recent work, it should be noted that McClain refers to the notion of "glaze-ice plateau" to describe anything other than Anderson plateau: the slightly rough area near the stagnation point where the instability of the runback film seems to be the cause of roughness. In addition, McClain et al [64] report that for fairly high values of A_c, quite close to $A_{c,lim}$, ice accumulation is no longer considered as "early-stage" (very thin ice thickness) but the ice shape starts initiating horn or scallop shapes when the conditions are met.

3.2.2.2.2.3 Non-uniform roughness models

More recently, non-uniform roughness size models were developed to account for the fact that roughness size is not constant along the ice shape and over time, which has been experimentally observed by [65], [60], [63], [64], [66], [67].

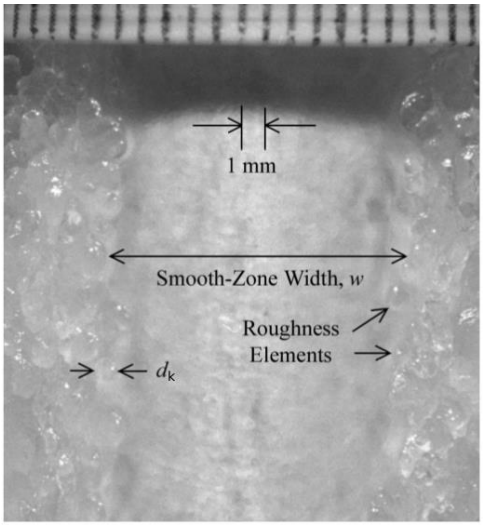

Figure 27 - Spatial distribution of rough elements, after Anderson [63]

Regarding spatial evolution, an almost smooth zone is often obtained near the stagnation point (Figure 27). Then, the roughness size increases significantly. Hansman and Turnock [65] report that isolated drops (formed by gradual coalescence) are observed on the surface and can remain stationary. The different authors therefore generally rely on a distinction of different regions, as shown in Figure 27, valid for both wing profiles and cylinders. In particular, they all model the possible existence of a smooth zone, followed by a rough zone. Feathers can be considered downstream the rough zone but are generally not explicitly modelled, although Hansman et al [68] specify that they are obtained in all rime regions (rime conditions but also dry areas of the glaze shapes, especially on horns).

Regarding the evolution over time, the roughness size increases during the first moments of accretion then it stabilizes, according to Anderson [62].

3.2.2.2.2.3.1 Description

Two global models are available in the literature to describe the spatial and temporal evolutions of roughness size. They were both derived from experimental characterizations. They are global in the sense that they depend on global icing conditions and not on local conditions on the icing surface (only numerical models offer the possibility to predict the roughness height but were not included in the present literature review since we focused on the roughness characterization).

Han et al [69] developed a non-uniform roughness model on 2D airfoils with AOA=0°. The model is based on a set of 74 cases, very differently investigated:

- 10 experiments of Han and Palacios [66] on a NACA0012 profile of 0.5334 m chord length, for air temperature in a range of -10.2°C to -3.6°C, LWC ranging from 0.25 to 1.7 g/m^3, air velocity from 44.5 to 66.7 m/s and MVD from 20 to 30 µm. The spatial distribution of roughness size was measured (in 8 positions from s/c= 0 to 0.08) at short accretion times included between 45 seconds and 2 minutes,
- Anderson and Shin [62] and Anderson et al [63] experiments (height of rough elements were considered as quasi-hemispheric),
- the Ruff correlation, Equation 2, built so that LEWICE can best reproduce a Gent experiment database. Here, k_s is "measured".

On the other hand, several studies have been carried out successively at Baylor University on NACA0012 profiles, with chord length in the range from 0.5334 m to 1.8288 m [70], with a sweep angle $\Lambda = 0°$ or 30° [71] (the chord length is 0.9144 m). The angle of incidence is always AOA = 0°. Another model was inferred from these investigations.

3.2.2.2.2.3.2 Main results, progress and limitations

Han et al expressed their correlation in the following form:

$$R_a = k_M - \frac{4k_M}{(l - w_s)^2}\left(s - \frac{l + w_s}{2}\right)^2 \qquad \textit{Equation 7}$$

$$\text{where } \frac{k_M}{2r_0} = -0.008246 \times \frac{A_c}{f_0} + 0.03752\sqrt{\frac{A_c}{f_0}}$$

$$\frac{w_s}{2r_0} = 0.07254(A_c f_0)^{-0.6952}$$

$$\frac{l}{c} = 0.075$$

The general form of the correlation as a function of the curvilinear abscissa *s* is consistent with the measurements of [66], as shown in Figure 28(a). A smooth-zone length w_s and a rough-zone length *l* are thus defined in accordance with common observations in the literature.

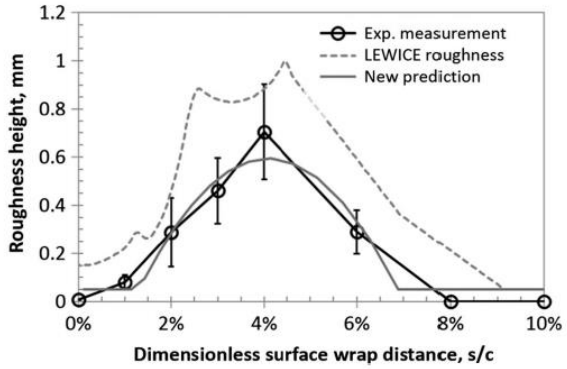

(a) Model derived from experiments

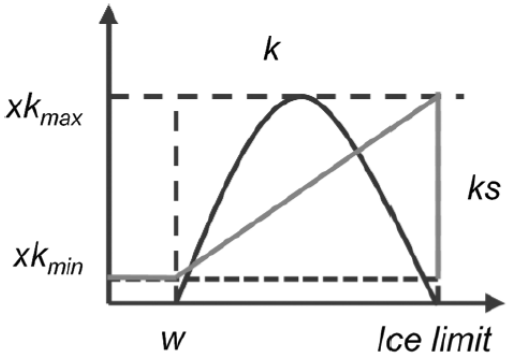

(b) simplified model used for feeding the Makkonen model

Figure 28 - Han and Palacios models, pictures extracted from [69]

The correlation on the maximum roughness height k_M reached at the top of the parabola was established by using the 3 types of data described above. It is not surprising that A_c is an important parameter since it was observed by Anderson. But f_0 is a parameter of the same order as A_c, while [63] neglects its impact (most authors nevertheless see f_0 as an important parameter). In addition, the correlation proposed for k_M has a high dispersion, especially for large A_c/f_0. Besides, k_M has a maximum in $A_c/f_0 \cong 5$. It therefore does not seem recommended to use the model for $A_c/f_0 > 5$ (it is not believed that the roughness size should decrease over time).

For the smooth zone length, w_s, the proposed correlation is based on both Han and Anderson's data. There is less dispersion. Again, the two parameters are A_c and f_0, although Anderson did not note any dependence on f_0 in the 1998 study. Note that with this expression of w_s, the smooth length tends towards 0 when the accretion time increases. Finally, the iced length is based on Han and Palacios' observations. In addition, *Ra* has been limited to a minimum of 0.05 mm to adapt to LEWICE constraints.

The model was used for comparisons with heat flux measurements on one side and accretion calculations for 0.25 m and 0.61 m chord lengths on the other side, which were quite representative of the model development range. However, it should be noted that in Han calculations with the Makkonen model exposed in section 4.2.4.2.2, the distribution of roughness is not k_s=*Ra*. As the heat transfer coefficient h_{tc} gradually increases, the too abrupt variation of *Ra* provided by Equation 7 leads to an overestimation of the exchange coefficient. So Han adopted a more gradual variation of k_s, linear from 0 to k_M in $s = l$ (Figure 28(b)). The results seem to rather agree with the measurements by doing so. But there is no real justification. In addition, the calculations presented in [69] were performed for final accumulation factor values A_c up to 4.26, which raises the problem of limiting A_c to $A_{c,lim}$.

It would be interesting to feed the codes with experimental data as modelled by Equation 7. The transitional area should then probably be taken into account to more physically smooth the variation of h_{tc}.

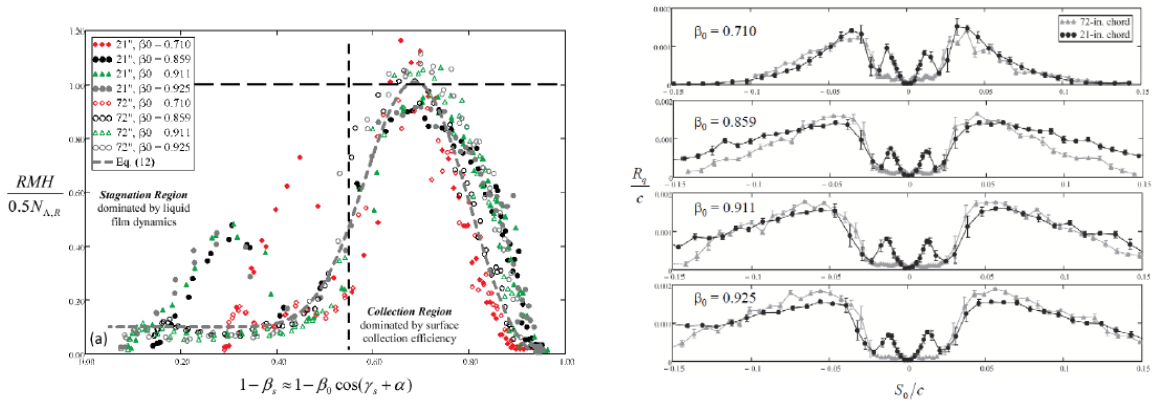

(a) McClain model (b) Rq/c

Figure 29 - Model and experimental characterizations of McClain and co-authors, pictures extracted from [64] and [72]

Regarding the investigations of McClain's group in Baylor University, the following relation was inferred from the successive studies:

$$\mathrm{RMH} = 3.09R_q = \mathrm{I}\,\mathrm{S}$$

$$\text{where } \mathrm{I} = C_t 2r_0 A_c \beta_0 \cos\Lambda$$

$$S = \frac{Wei\left(\beta - 0.05, \beta_{fb} - 0.15, 3\right)}{Wei\left(0.875\left(\beta_{fb} - 0.15\right), \beta_{fb} - 0.15, 3\right)} + \frac{0.1}{2}\left(1 - \tanh\left(10\left[\beta_{fb} - \beta\right]\right)\right)$$

$$Wei(x, \lambda, k) = \frac{k}{\lambda}\left(\frac{x}{\lambda}\right)^{k-1} e^{-(x/\lambda)^k} \qquad \textit{Equation 8}$$

β_0 and β_{fb} are the collection efficiency at the stagnation point and at the liquid-film breakdown location, respectively and Λ is the sweep angle. The model was developed using Langmuir and Blodgett's approach to assess β_0 [64]. A sinusoidal evolution assumption was also used to obtain a distribution of the collection efficiency:

$$\beta = \beta_0 \cos(AOA + \gamma_s) \cos\Lambda \qquad \textit{Equation 9}$$

γ_s is the angle that the normal makes to the surface of the wing at the curvilinear abscissa s (Figure 30). The C_t coefficient was assessed as C_t=*0.5* for the straight and swept wings tested [64]. Some possible adaptations are proposed for C_t in [71]. *Wei* is the Weibull probability density function.

The location of the film breakdown is probably the hard point of the model. We can imagine that the previous Han correlation for w_s could be used for example. However, for simplicity, β_{fb}=0.45 is used as in [71]. Besides, this model was developed for the rough area, where the roughness size is linked to the droplet collection (Figure 29(a)). Smooth zone modeling, where the roughness size is linked to film runback instability, was designated as valuable further work in [64].

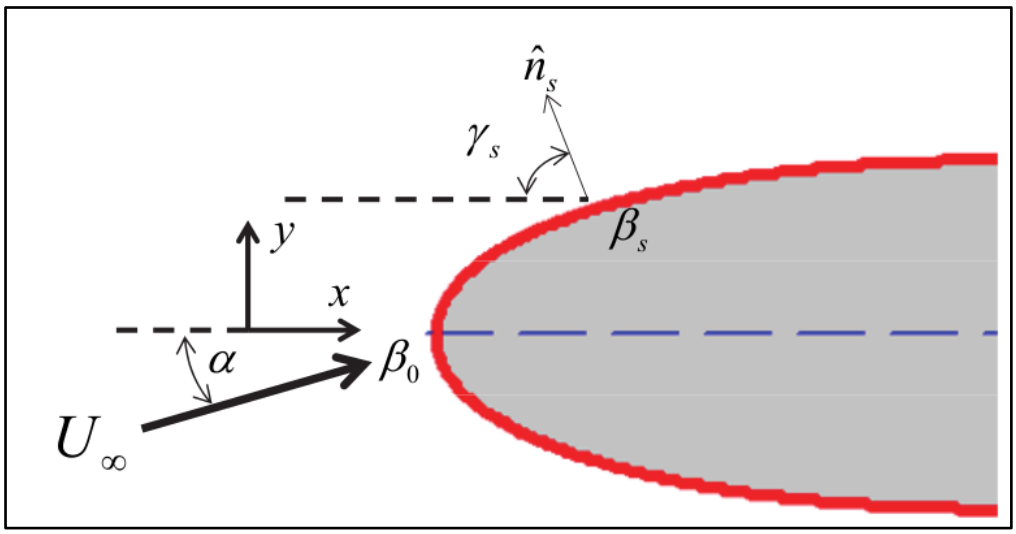

Figure 30 –Geometric evaluation of local surface collection efficiency [70]

No time limitations are reported for RMH. The roughness must therefore linearly increase over time, via A_c. However, McClain studied rather short accretion times (A_c=0.348 in [70], A_c ranges from 0.061 to 0.408 in [72] or from 0.03 to 0.484 in [71]). As for Han, we can imagine a threshold on A_c, as observed by Anderson, beyond which the size of the roughness no longer increases. Among the limitations, McClain points out that Equation 8 was established for a reduced range of f_0 (from 0.19 to 0.25), for symmetric wings with zero-AOA.

3.2.2.2.3 Conclusions

The roughness-distribution structure most often observed is that of an area in the vicinity of the stagnation point where the roughness size is very small, followed by an area where the roughness size significantly increases (corresponding to experimental observations like in Figure 27). Additionally, the size of rough elements increases over time. But an author like Anderson suggests that an asymptotic value exists and is approximated for an accumulation parameter value of about A_c=*0.4*.

The main models in the literature have been tested on several test cases (an example is provided in Figure 31, where the error bars around the experimental data are quite large because a 99% confidence interval is given). The orders of magnitude are generally all the same. But the precise comparison is made difficult by the fact that the different models are not necessarily based on the same definition of the roughness size (k_s for uniform models, maximum height of rough elements for Anderson, *Ra* for Han and Palacios measurements, *Rq* for McClain). It must be noted that R_q was favoured over *RMH* for McClain's model because R_q was shown of order 0.001c in [72] (Figure 29(b)). It is worth mentioning that for the PHYSICE model, the two additional parameters, *k* and S_{corr}, have

also to be determined, and are not be necessarily linked to any of the parameters characterized in the literature up to now.

Besides, the cross-comparisons between the various models also pointed out that a large dispersion is observed (for instance, even Han's model does not reproduce all Han's database very accurately), that not all models have the same driving parameters and that there are inherent weaknesses in the construction of the models (for instance, the use of Equation 9 is a restrictive assumption for McClain's model).

The models generally need to make the roughness height non-dimensional. The chord length is generally used for this purpose. The agreement with the experiment seems correct for a range of chord lengths in the range of 0.2 to 2 m. But the experiments are almost all done on NACA0012 airfoils without zero-AOA. This is the case for the example in Figure 31. One key issue is thus to know if using another reference length for non-dimensional roughness height would be relevant. The radius of curvature at the leading edge would be an example of alternative reference length. A model of this type could generate very different roughness sizes for profiles with very high curvature at the leading edge. Experiments on profiles whose leading edge curvature is not that of a NACA0012 would be interesting to answer to this question.

Glaze conditions have been extensively studied in the literature. In colder conditions, it seems that the roughness sizes are expected to be smaller, but the characterization of the rime conditions still needs further investigation.

The onset of the laminar-turbulent transition depends on the roughness and may have a significant effect on the ice shapes. It will therefore be necessary to make progress on the modelling of the smooth area at the stagnation point and the transition to the highly roughened area. Models have been proposed in the literature, but there are still contradictions that need to be addressed.

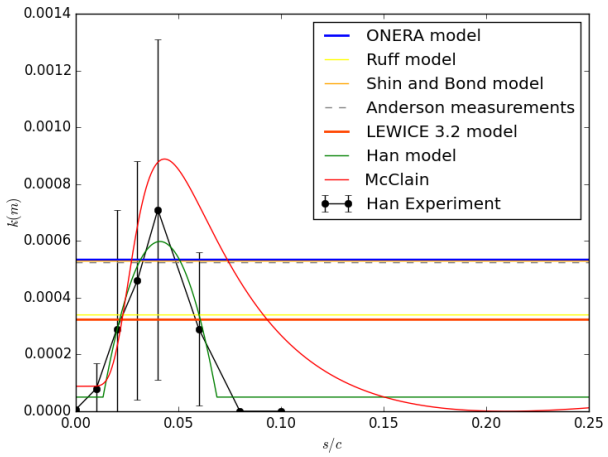

Figure 31 - Roughness size produced by several models of the literature on the R3 case in Han and Palacios database [66]

3.2.2.1 Roughness characterization for App O [TUBS, ONERA, CIRA, TUDA, POLIMI]

3.2.2.1.1 Objectives and issues

Roughness characterization of icing formations under the conditions established on Appendix O [73] is an early step needed to be done for the development of numerical tools for CFD. As well known, roughness on a surface has a strong effect on flow characteristics of the boundary layer: shear stress is altered [74], as well as the close-to-the-wall turbulent characteristics [75], which also result in a change on the local rate of heat transfer.

The alteration of flow characteristics due to roughness can influence the way ice is accreted over a surface, as well as the shapes of the resulting ice structures. But, the formation of the roughness itself depends on the current state of the flow and the physics of drop impingement and wall film dynamics. Therefore, numerical tools need to calculate the way roughness evolves in an iced surface according to the current flow characteristics and then evaluate the way the flow characteristics change due to this roughness. In this section, we will make comment on the way roughness is developed.

3.2.2.1.2 Literature review

3.2.2.1.2.1 Self-organizing map approach

3.2.2.1.2.1.1 Description

Appendix O deals with Supercooled Large Droplets which can have MVD values above of 40 microns [73]. In this topic, we comment about the works of McClain, Vargas and Tsao, which, with the aid of some other authors, have published several research papers about the current topic. In their work, roughness is characterized with a parameter designated as RMH (Roughness Maximum Height) using a method called “self-organizing map approach”, or SOM, which is based on neural networks [76]. For ice shape applications, the SOM analyses clusters of three-dimensional “noisy” data obtained from laser scans of ice shapes in order to generate a one-dimensional representative manifold or curve. Figure 32 shows a generated manifold β from several sets of data.

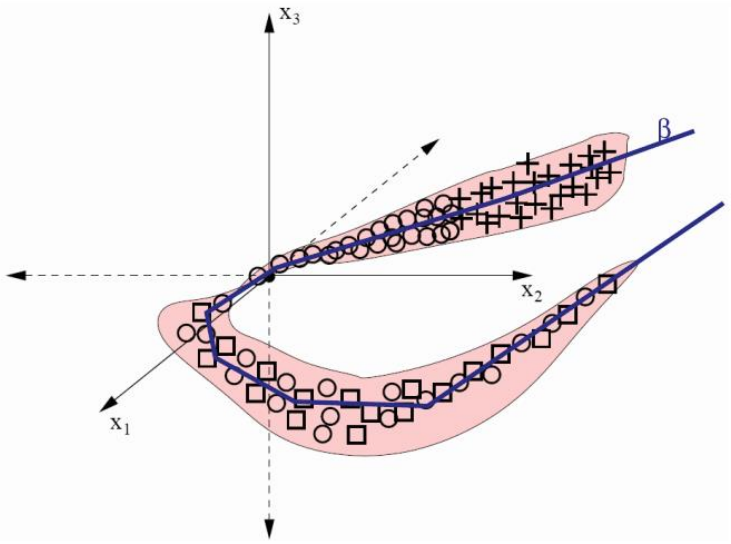

Figure 32 – Example of manifold β generated from clusters of data

The generated manifold is composed of connected points, designated as codebook vectors. The generation of the codebook vectors is done through a method that refines an initial random distribution of vectors. The refinement process moves the vectors in the direction of clusters of points, finally describing a representative manifold, as shown in Figure 33. Since this method is based on neural networks, a training process is required.

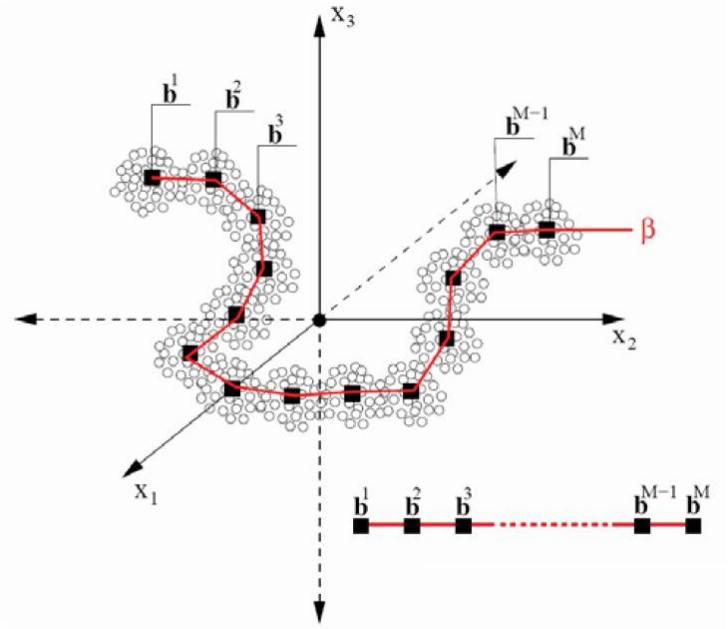

Figure 33 – Self-Organizing Map example over point clouds

Once defined a manifold that describes the main ice shape, the height of the points towards the closest codebook vector can be used to calculate roughness parameters. For example, the roughness maximum height (RMH) in the location of the codebook vector can be calculated as being three times the root-mean-square of the height relative to that codebook vector [76]:

$$RMH_b = 3R_b = 3\left[\frac{1}{J}\sum_{j=1}^{J} {h_{b,j}}^2\right]^{\frac{1}{2}}$$

With this method, a clean ice geometry can be generated with a roughness distribution associated to it. With this, the analysis of aerodynamic effects over icing conditions can become more effective.

3.2.2.1.2.1.2 Main results, progress and limitations

Measurements have been carried in order to observe the evolution of ice shapes under icing conditions stated in both appendix C and O (SLD cases). Figure 34 and Figure 35 are taken from a study from McClain et. al. [77], showing evolution of ice roughness and thickness over time on a 36 in. NACA 0012 airfoil for a velocity around 67 m/s, static temperature of -4.6 °C and LWC of 0.6 g/m3. A particle MVD of 30 microns was used for the appendix C test cases, while for appendix O a MVD of 150 microns was used. The SOM approach was applied to get sets of data from both appendix C and O conditions.

It can be seen that roughness variations along the surface are different between both cases, as well as the ice thickness distribution, which show a wider plateau for appendix O cases.

Additional studies [78] were carried on a NACA 0012 for appendix O cases with different particle MVD and LWC, which results are shown in Figure 36.

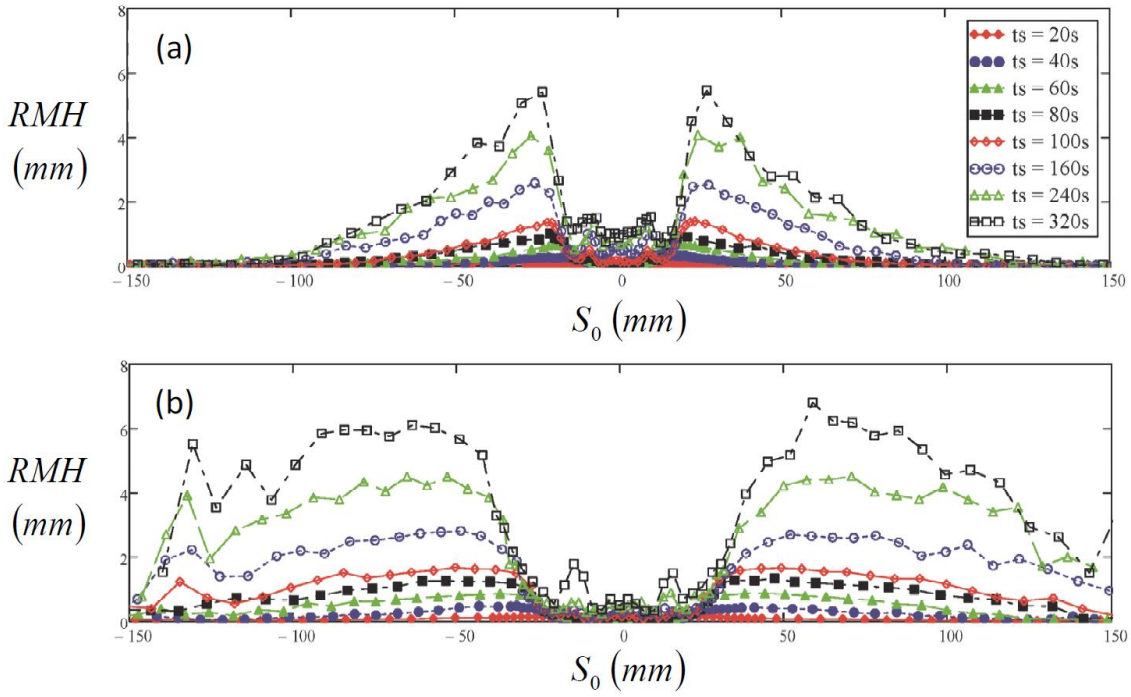

Figure 34 - Surface roughness along a NACA 0012 surface for Appendix C (a) and O cases (b) [69]

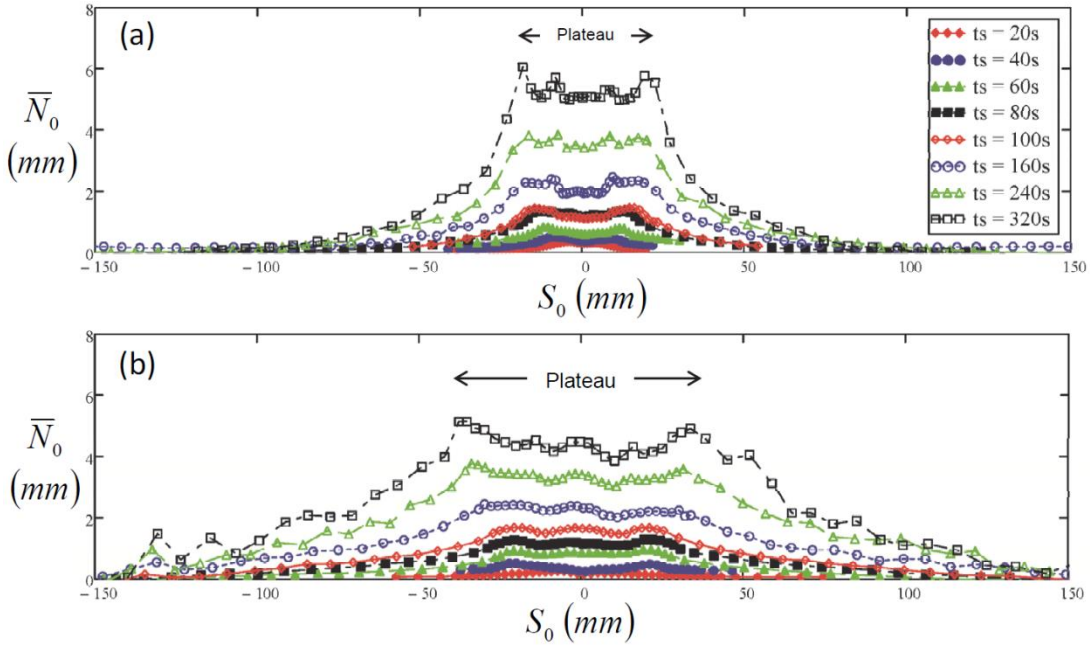

Figure 35 - Ice thickness along a NACA 0012 Surface for Appendix C (a) and O cases (b) [75]

From Figure 36, it can be noticed that the RMH on appendix O cases is directly related to the accumulation parameter. In contrast, experiments for appendix C conditions (Shin, 1994) show that the RMH tends to reach an asymptotic value as the accumulation parameter A_c is increased.

Although McClain reported an equation for the temporal and spatial behaviour of roughness under appendix C conditions, he states that the first-order transient effects of SLD surface roughness are still not well understood and further research is necessary for these conditions [77]. A limitation appears as the lack of a proper model which will describe evolution of roughness under appendix O conditions.

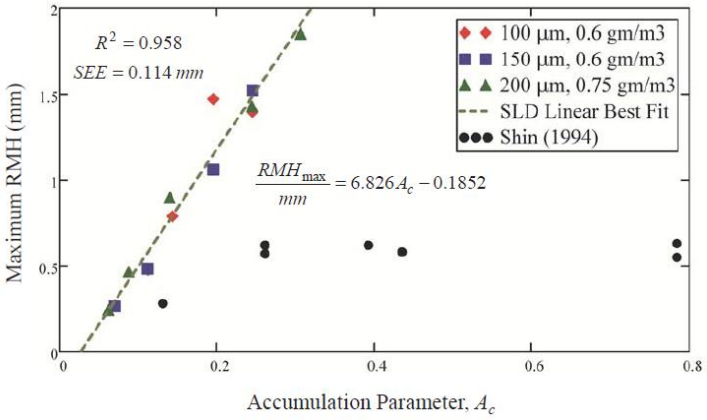

Figure 36 - Airfoil RMH as a function of accumulation parameter [76]

3.2.2.1.3 Conclusions

An introduction of the Self-Organizing Map approach was given, which is used in order to characterize the ice shapes, as well as to obtain values of distribution of roughness parameters over a surface.

With this method, ice shapes for cases under conditions of appendix C and O (SLD) were characterized. Differences in the ice thicknesses and roughness distributions were found between these cases.

A model for spatial and temporal evolution of roughness for appendix C cases was proposed (check “Roughness characterization for App C” section), although is stated that appendix O (SLD) cases require further investigation.

3.2.2.2 Boundary layers on rough walls [ONERA, CIRA, TUDA, TUBS, POLIMI]

3.2.2.2.1 Objectives and issues

Wall roughness has an impact on skin friction, heat transfer and laminar-turbulent transition. By the way, the latter also has an influence on the level of heat transfer and skin friction. The iced walls are highly rough, and convective heat transfer has a major effect on the accretion process. In particular, glaze ice shapes, for which water runback occurs, are highly dependent on heat transfer and therefore on wall roughness.

Regarding the impact on the laminar-turbulent transition, the classic approach is based on a critical roughness Reynolds number $Re_{k,crit} = \left(\frac{ku_k}{\upsilon}\right) \cong 600$ [79]. This model is implemented in most icing suites, with various assessments of the velocity u_k in particular. A brief literature review shows that it would be interesting to revisit this model, particularly by considering the effect of the airflow Reynolds number, and by suggesting that an enlarged transitional region be taken into account [80] [81]. However, the present literature review will not focus on the impact of wall roughness on laminar-turbulent transition.

Regarding ice accretion simulations, the classic approach to model the impact of roughness on skin friction and heat transfer is Makkonen's integral approach, which is compatible with integral boundary layer codes coupled with inviscid solvers. RANS models have also been developed, notably recently at ONERA, as part of the PHYSICE project.

3.2.2.2.2 Literature review

3.2.2.2.2.1 The effect of roughness on the boundary layer

Roughness is a component of surface texture. It is quantified by the deviations in the direction of the normal vector of a real surface from its ideal form.

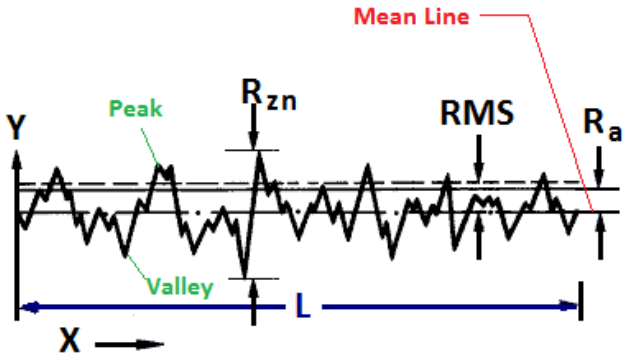

Figure 37 – Scheme for surface roughness

Roughness can be considered as “distributed” if the imperfections globally cover the surface, or “localized” if it is concentrated in one point or a small region of the considered geometry.

The effect of roughness on a boundary layer strongly depends on the parameter k/δ where k is the height of the roughness and δ is the thickness of the boundary layer. In case of constant protrusion height, this parameter decreases with the distance from the stagnation point since the thickness of the boundary layer increases with the distance. This means that the flow can be completely rough in the forward portion of a boundary layer and eventually become smooth in the last part.

Historically the results obtained by Nikuradse [82] for rough pipes have been transposed to boundary layers. Nikuradse [82] performed experimental studies for flows in smooth pipes and in pipes artificially roughened with sand of different grain size k_s glued on the walls of the pipes. He identified

as key parameter the ratio between the protrusion height and the thickness of the laminar boundary layer k_s/δ_l. If this parameter is less than one, i.e. the roughness element is well inside the laminar boundary layer, roughness has no effect. This parameter can be turned into a Reynolds number considering that $\delta_l \sim \nu/u_\tau$ and hence $k/\delta_l \sim \frac{ku_\tau}{\nu}$ can be considered as a Reynolds number based on the roughness height and the friction velocity u_τ. Three regimes can be identified:

- **Hydraulically smooth**: $0 \leq \frac{k_s u_\tau}{\upsilon} \leq 5$. All roughness protrusions are inside the laminar region of the boundary layer;
- **Transition regime**: $5 \leq \frac{k_s u_\tau}{\upsilon} \leq 70$. Roughness protrusions partly go out of the laminar sublayer;
- **Completely rough**: $\frac{k_s u_\tau}{\upsilon} > 70$. All the roughness protrusions are out of the laminar sublayer.

The log-law of the velocity profile on smooth surface holds also for flows over rough surfaces as:

$$\frac{u}{u_\tau} = \frac{1}{\kappa_a} log\left(\frac{y}{k_s}\right) + B - \Delta U^+$$

with ΔU^+ depending on the sand grain roughness following the different roughness regimes above defined.

The relation between roughness and the term ΔU^+ has been achieved experimentally and the effect of this term is shown in the following figure.

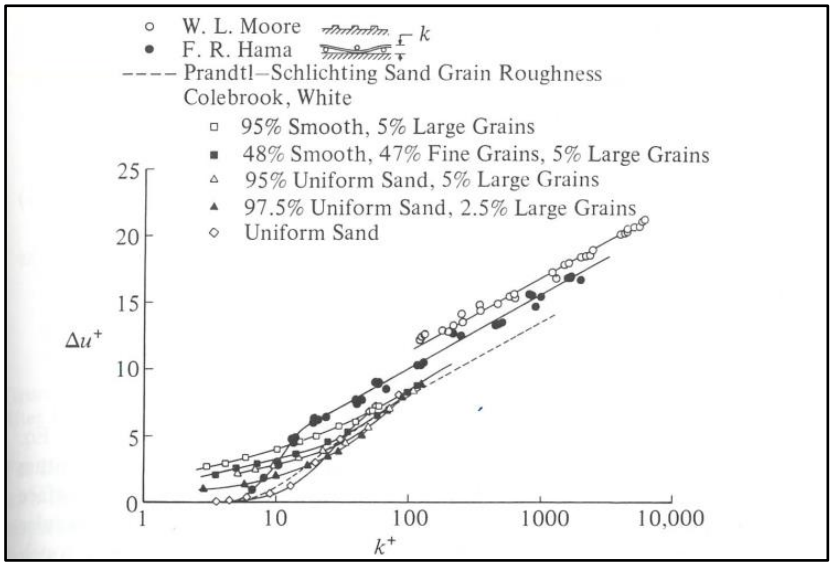

Figure 38 – Effect of wall roughness on universal velocity profiles

The roughness impacts the transition. The height of the protuberances that causes transition in a laminar boundary layer is defined as critical roughness. This has a consequent effect on drag. For bodies whose main contribution to drag is friction, the drag increases because the transition point moves upstream. If the main contribution is due to the drag form, the drag can decrease. The critical value of the roughness is considered to be [74] :

$$\frac{u_\tau \, \kappa_{crit}}{\nu} = 15$$

The skin friction coefficient turns out to be a function of the Reynolds number $Re = \frac{U_\infty l}{\nu}$ and also of the relative roughness l/κ_s with l a characteristic length of the geometry. The drag of bluff bodies, such as cylinder, is very sensitive to roughness. The critical Reynolds number for which the drag of a cylinder has a sudden drop, decreases as roughness increases.

It is possible to define the admissible roughness as the maximum height of roughness elements which does not cause an increase in drag with respect to a smooth wall. For a flat plate, this can be summarized as:

$$\frac{U_\infty \kappa_{adm}}{\upsilon} = 100 \Rightarrow \kappa_{adm} \leq 100 \frac{\nu}{U_\infty}$$

This provides the maximum height of the roughness element that does not depend on the length of the plate. It can be more convenient to introduce a dependence on the length of the plate and in general of the body. This can be simply achieved by introducing the Reynolds number and hence

$$\frac{\kappa_{adm}}{l_{ref}} \leq \frac{100}{R_{l_{ref}}}$$

The roughness of the experiments of Nikuradse can be considered of distributed type with maximum density because the grains of sand were glued as closely to each other as possible. In practical applications, the density is smaller and a correlation with the sand roughness should be made. The correlation is “simple” in the completely rough regime. A given roughness is equivalent to the sand roughness at the value that gives the same coefficient of resistance.

Instead, a localized roughness represents an imperfection concentrated in a given region of hydraulically smooth surface. The effect of this kind of roughness has been extensively studied in the framework of stability theory. A linearization of the roughness element is performed using a Taylor expansion, leading to a non-homogenous boundary condition at the wall. Large Eddy and Direct Numerical Simulations are also employed to study the effect of local roughness on the boundary layer.

Reviews of turbulent flows over rough walls are presented in [83] and [84]. Raupach et al. [85] present a review of rough-wall turbulent boundary layers, drawn from both laboratory and atmospheric data. The former apply mainly to the region above the roughness sublayer (in which the roughness has a direct dynamical influence) whereas the latter resolve the structure of the roughness sublayer in some detail. The authors affirm that there is strong support for the hypothesis of wall similarity. At sufficiently high Reynolds numbers, rough-wall and smooth-wall boundary layers have the same turbulence structure above the roughness (or viscous) sublayer, scaling with height, boundary-layer thickness, and friction velocity.

The main conclusion of the paper from Jiménez [84] is that roughness is far from being fully understood. The experiments are often conflicting due to the industrial emphasis on many experimental investigations, which do not probe into the turbulent structures of the flow. Also part of the problem is the variety of rough surfaces, which strongly influences the dynamics of the roughness layer. In flows where δ/κ is high, the effect of the roughness presumably reaches the outer flow only after a long series of chaotic interactions. The classical result is that the buffer layer can be perturbed without transmitting to the outer flow anything beyond a change in skin friction, but there are indications of deeper interactions [84].

3.2.2.2.2.2 Integral boundary layer approach

In most accretion suites used for certification, the calculations of the heat transfer coefficient h_{tc} are based on a simplified integral boundary layer method, coupled with an inviscid calculation. Since the ice is rough, the calculation takes into account the influence of the wall roughness on the skin friction coefficient C_f and h_{tc}. Generally, it is Makkonen's model [86], adapted from the work of Kays and Crawford [87], which is used in icing codes:

$$\frac{C_f}{2} = \frac{0.1681}{[\ln(864\frac{\theta}{k_s} + 2.568)]^2}$$ *Equation 10*

$$h_{tc} = \rho u_e c_p St \text{ , where } St = \frac{C_f/2}{Pr_t + \sqrt{C_f/2}\mathrm{T}_0^+} \text{ and } T_0^+ = \frac{1}{1.92\left(k_s^+\right)^{-0.45} Pr^{-0.8}} \quad \textit{Equation 11}$$

where *Pr* is the Prandtl number of air and Pr_t=0.9 is the turbulent Prandtl number. ρ is the density of air, c_p its thermal capacity at constant pressure. The main input data are therefore the flow velocity u_e, the momentum thickness in turbulent regime θ (generally calculated using smooth-flat-plate assumptions) and the equivalent sand-grain roughness height k_s. This model is therefore very well suited to integral boundary layer approaches, which provide θ as an output.

3.2.2.2.2.2.1 Description

Regarding roughness parameters, the model only depends on k_s. The RANS approach derived in the PHYSICE project accounts for two additional parameters, as shown in section 3.2.2.2.2.3. The PHYSICE model was thus adapted to an integral boundary layer framework in [88].

The model consists, like Makkonen's model in post-processing dynamic boundary layer calculations on smooth walls to derive the friction coefficient and h_{tc} on rough walls. However, the whole derivation process described in [87] was re-worked to account for the PHYSICE model. The new model, integral AGC (for Aupoix-Grigson-Colebrook), therefore depends on the equivalent sand-grain roughness height and the momentum thickness like Makkonen's model, but also on Aupoix's parameters $k=\alpha k_s$ and S_{corr}:

$$\frac{C_f}{2} = \frac{0.1681}{\left[\ln\left(945.5\frac{\theta}{k_s}/\left(1 + 3.75/k_s^+\right) + 2.568\right)\right]^2} \quad \textit{Equation 12}$$

$$St = \frac{\frac{C_f}{2}}{Pr_t + \sqrt{\frac{C_f}{2}}\left(D_\theta - Pr_t \mathrm{D} + \mathrm{T}_0^+\right)}, \quad \textit{Equation 13}$$

$$T_0^+ = \frac{F\left(k_s^+, S_{corr}\right)}{\kappa} e^{-\frac{y_0^+}{k^+}}\left[Ei\left(-\frac{\delta^+ + y_0^+}{k^+}\right) - Ei\left(-\frac{y_0^+}{k^+}\right)\right],$$

$$y_0^+ = 0.105 + 0.028 k_s^+$$

where δ is the boundary layer thickness, *D* and D_θ are constants for modelling the wake region of the boundary layer.

3.2.2.2.2.2.2 Main results, progress and limitations

On the one hand, the study showed that the friction coefficient model derived from Grigson-Colebrook relationships did not provide any added value over the Makkonen model. On the other hand, the use of Equation 13 seems valuable. The h_{tc} model indeed allows to capture changes in Stanton St number for cases where k_s is unchanged but *k* and S_{corr} are different. For example, in Figure 39, the integral model implemented in the ONERA's BLIM2D integral boundary layer solver ("BLIM2D AGC") captures the decrease of St whereas the standard Makkonen model ("BLIM2D KC") remains unchanged (example of Dukhan flat-plate models 1 and 7 [89]).

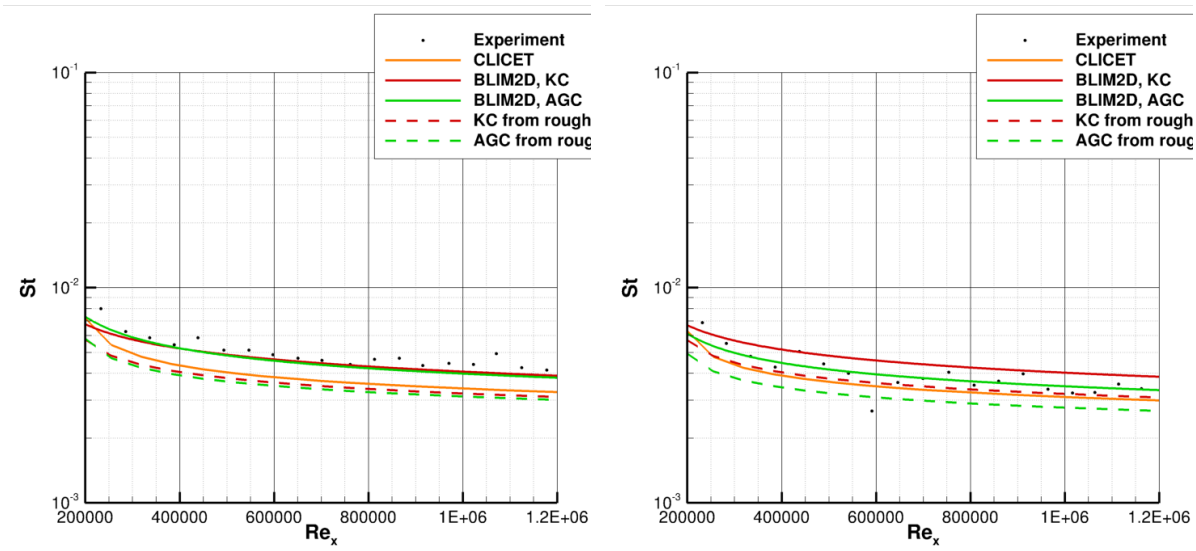

(a) Dukhan model 1, k_s=2.51 mm, S_{corr}=1.22, α=0.749 *(b) Dukhan model 7, k_s=2.25 mm, S_{corr}=1.08, α=0.48*

Figure 39 - Assessment of the integral-AGC model implemented in BLIM2D on Dukhan's flat-plate models 1 and 7. Comparison against Makkonen's model (KC) and the RANS AGC model (implemented in the code CLICET). Comparison between using smooth-wall momentum thickness and rough-wall momentum thickness (from rough). Pictures extracted from [88].

The study also showed that the classical Makkonen model was built to be fed by the smooth-wall momentum thickness, which is easily produced by a simplified integral model. The example in Figure 39(a) is typical: feeding the Makkonen model with rough-wall data "KC from rough" degrades the results compared to the default approach "BLIM2D KC" using smooth-wall data. The same is true for model 3 where the differences between models are more obvious (Figure 40). On the contrary, it usually seems better to feed the integral-AGC model with the rough-wall data. This is not obvious on models 1 and 7, but other models such as model 3 in Figure 40 show a very clear improvement over the experiment. Above all, the integral-AGC model then generally behaves more in accordance with the AGC RANS model implemented in CLICET. This means that the integral-AGC model will have to be implemented in BLIM2D as a closure model that can change the boundary layer thickness.

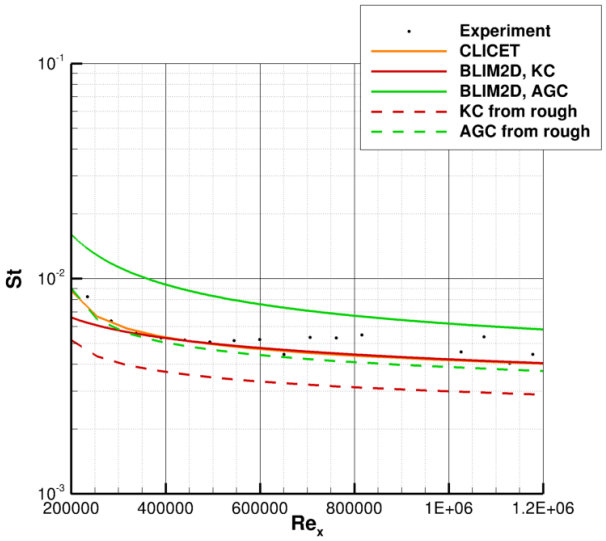

Figure 40 - Assessment of the integral-AGC model implemented in BLIM2D on Dukhan's flat-plate model 3. k_s=15.63 mm, S_{corr}=1.22, α=0.1964. Comparison against Makkonen's model (KC) and the RANS AGC model (implemented in the code CLICET). Comparison between using smooth-wall momentum thickness and rough-wall momentum thickness (from rough). Picture extracted from [88].

Finally, preliminary calculations were presented on a NACA0012 studied by Han and Palacios (Figure 41). In addition to the fact that the integral-AGC model should be more accurate when used as a proper closure model for BLIM2D (which was not done here), several difficulties were identified. First of all, the roughness parameters were measured by Han and Palacios, but only the evolution of *Ra* is available, which does not allow to characterize the three parameters of the integral AGC model. In addition, the problem of the laminar-turbulent transition is tricky. It seems that the transitional area is very large. Han and Palacios "solved" the problem by not directly using the roughness heights they measured but by using a slower growth in roughness size. This approach does not seem satisfactory because it is probably adapted to the case and the roughness model (Makkonen) used. It seems more physical to reproduce a transition model based on intermittence functions. The test case therefore remains to be investigated further.

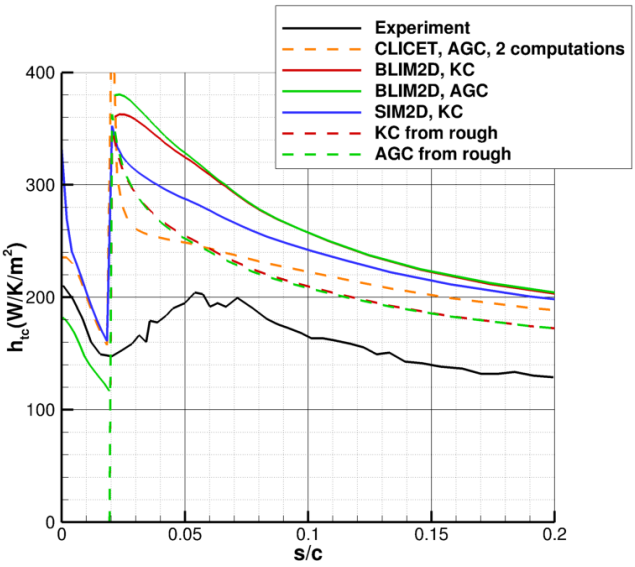

Figure 41 - First test of integral-AGC BLIM2D simulation on Han and Palacios R3 case. Comparison against experiment, (RANS AGC) CLICET, Makkonen's model (BLIM2D KC). Comparison between using smooth-wall momentum thickness and rough-wall momentum thickness (from rough). Picture extracted from [88].

3.2.2.2.2.3 Roughness-effect model for RANS approaches

Several models were recently developed at ONERA to account for the effect of roughness on the skin friction and h_{tc} in RANS approach, especially during the PHYSICE project.

3.2.2.2.2.3.1 Description

In the PHYSICE project, Aupoix developed roughness corrections based on the equivalent sand grain approach and applied to the k-ω turbulence model. The strategy already developed at ONERA to extend a turbulence model to rough walls was reapplied. The idea is that the shift in the logarithmic law of the wall due to roughness must be reproduced (Figure 42). It characterizes the increase of the skin friction. To do so, the solution of the turbulence model is shifted. This leads to non-zero values for the turbulent scalars at the wall (in this case k_w and ω_w), depending on the reduced height of the equivalent sand-grain roughness height k_s^+ [90]. The behaviour of the boundary layer can be analytically modelled for very low or very high values of k_s^+. But the complete laws must be determined numerically, with low- and high-k_s^+ behaviours providing guidelines for deriving an analytical representation of the results. Since there are several representations in the literature of the logarithmic region shift law as a function of k_s^+, two models based on Nikuradse and Colebrook-Grigson laws were developed. Comparisons of the computational predictions against experimental data over a wide range of k_s^+ and pressure gradients led to a preference for the second model, given hereafter, especially for very large roughness.

$$\Delta u^+ = \frac{1}{\kappa}\ln(1+\frac{k_s^+}{e^{1.3325}})$$

$$\Rightarrow \quad k_w^+ = \max\left(0, \frac{1}{\sqrt{\beta^*}}\tanh\left[\left(\log_{10}\frac{k_s^+}{30} + 1 - \tanh\frac{k_s^+}{125}\right)\tanh\frac{k_s^+}{125}\right]\right)$$

$$\omega_w^+ = \frac{300}{k_s^{+2}}\left(\tanh\frac{15}{4k_s^+}\right)^{-1} + \frac{191}{k_s^+}\left(1 - e^{-k_s^+/250}\right)$$

Equation 14

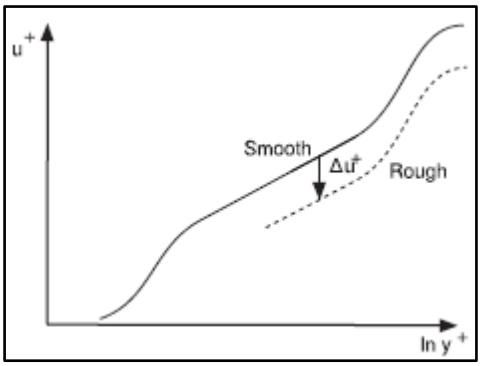

Figure 42 - Velocity profiles over smooth and rough walls, in wall variables [91]

Regarding heat transfer, roughness corrections are often based on a constant turbulent Prandtl number assumption. Therefore, the Reynolds analogy is assumed to remain valid in presence of roughness. However, this usually leads to an overestimation of the wall heat flux. A correction to account for the roughness effect on heat transfer was thus developed to better estimate the wall heat flux [91]. It consists in deriving a modification of the turbulent Prandtl number in the vicinity of the wall as follows:

$$Pr_t = Pr_{ts} + \Delta Pr_t$$

$$\text{where} \quad \Delta Pr_t = F(k_s^+, S_{corr})\, e^{-y/k}$$

$$F(k_s^+, S_{corr}) = A(\Delta u^+)^2 + B\Delta u^+$$

$$A = (0.0155 - 0.0035 S_{corr})\left(1 - e^{-12(S_{corr}-1)}\right) \; B = -0.08 + 0.25 e^{-10(S_{corr}-1)}.$$

Equation 15

The discrete element approach was employed to generate a large database by varying the shape of the rough elements, their spacing and size. This database was then analyzed to derive a model for ΔPr_t. This analysis first confirmed the fact that a second parameter is needed to quantify the thermal effect of roughness, as surfaces leading to the same drag increase may give different wall-heat-flux increases. This led to the introduction of the corrected wetted surface ratio S_{corr}. Additionally, the modification of the turbulent Prandtl number must be restricted to the wall region, characterized by the mean roughness height k, justifying the use of an exponential decay. Whereas the rough-wall model for the dynamic behaviour of the boundary layer depends of the turbulence model, the ΔPr_t correction for the thermal behaviour may be used in conjunction with any turbulence model.

Aupoix model [91] [90] were initially developed in a low-Reynolds number framework, involving fine meshes at walls. A need was identified to complete this approach by developing a wall function that could be used on coarse meshes. Such a development has been made in the SUNSET2 program by Chedevergne [92], relying on principles given by Aupoix and involving the analytical wall function of Craft et al [93]. The rough-wall analytic wall function originally developed by Suga et al [94] was thus adapted to unstructured codes and upgraded from Aupoix model for the thermal boundary layer.

3.2.2.2.2.3.2 Main results, progress and limitations

Several academic databases were investigated to validate Aupoix's (low-Reynolds number) model. Figure 43 presents the model predictions for surface conditions obtained by Dukhan *et al.* on ice surfaces generated in NASA IRT [89]. In each figure, the lowest curve corresponds to the smooth-wall calculation. The results obtained with the Spalart and Allmaras and k-ω SST models, assuming constant turbulent Prandtl number, give significant increases in Stanton number, similar to the increases in the friction coefficient. The proposed correction makes it possible to find a good agreement with experiments.

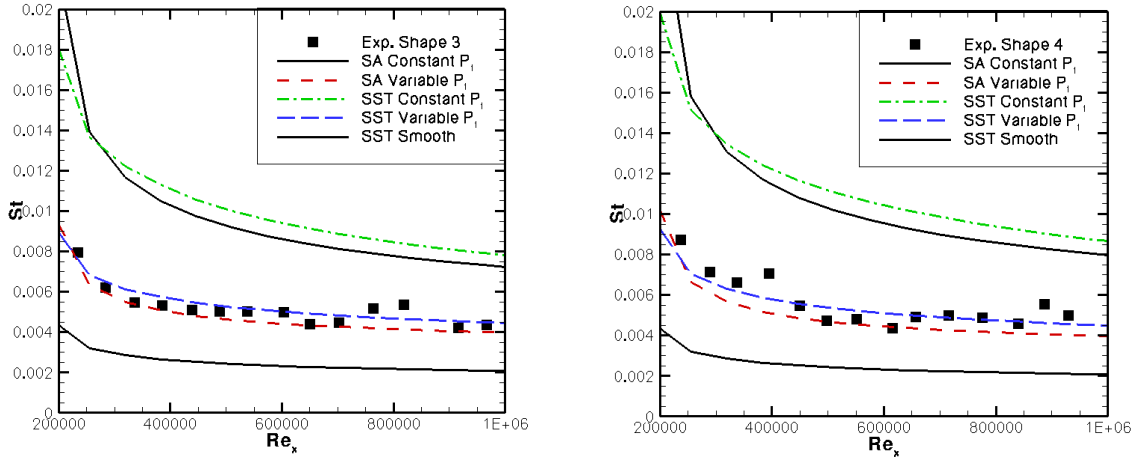

(a) Dukhan model 3 (b) Dukhan model 4

Figure 43 - Comparison between models and experiments on Dukhan database [91]

Figure 44 shows the results obtained for an accelerated flow. The flow is such that the boundary layer is in equilibrium regime, characterized by a constant friction coefficient, on a part of the test section. Figure 44(a) shows that, in this case where the temperature is a passive scalar, the thermal model does not influence the friction coefficient prediction and that the plateau is well captured, slightly overestimated with the k-ω SST model. Figure 44(b) shows again the contribution of thermal correction.

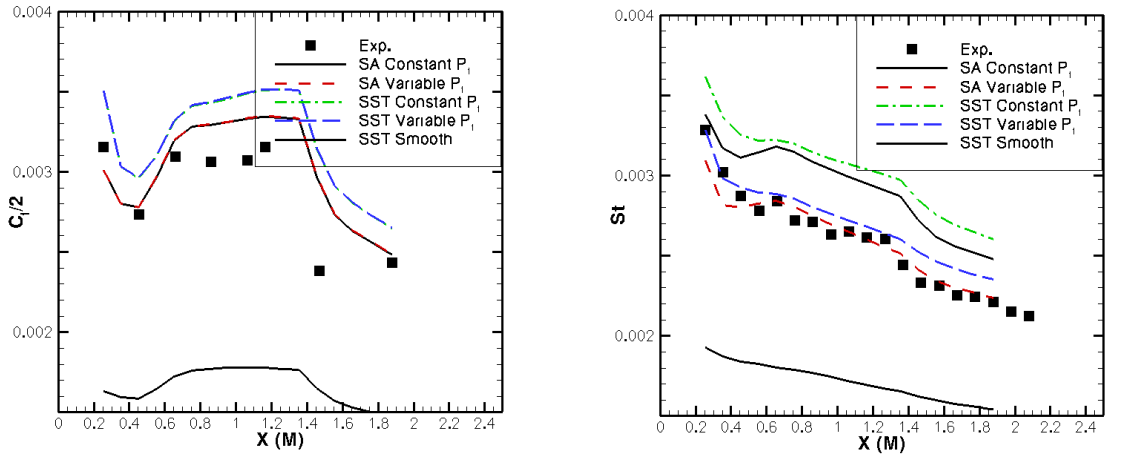

(a) skin friction coefficient C_f (b) Stanton number St

Figure 44 - Comparison between models and experiments on Coleman et al. database [91]

As already mentioned in section 4.1.2.3, the main difficulty is now to determine the rough-wall properties k, k_s and S_{corr} for the ice shape.

A validation work was also made to evaluate the ability of Chedevergne rough-wall analytic wall function approach to provide accurate results in academic icing configurations (Figure 45). The new analytic wall function was proven to enlarge the range of applications of wall laws, compared to the

one initially proposed by Suga, and to make it possible to capture the effect of the increase of the wetted surface due to roughness. Some work remains to be done for more complex icing configurations (airfoil shapes).

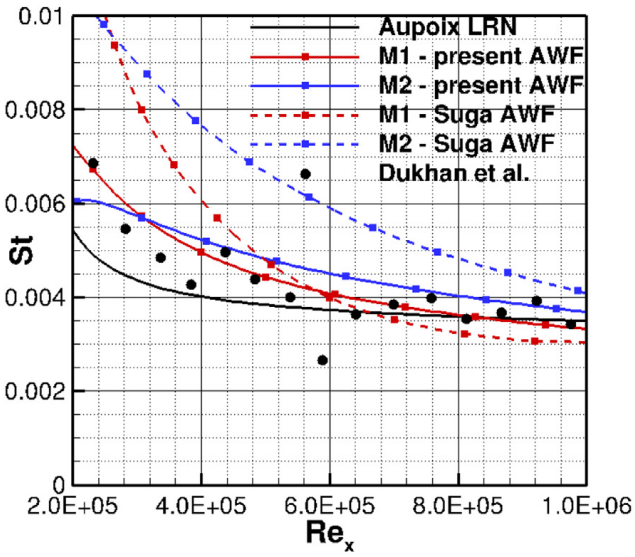

Figure 45 - Validation of Chedevergne's wall-law approach ("present AWF") on Dukhan model 7 test-case. Two levels of grid refinement investigated (M1 and M2). Comparison against Aupoix model with low-Reynolds-number approach ("Aupoix LRN") and against Suga rough-wall analytical wall function ("Suga AWF") [92]

It is also worth noticing that ONERA developed an experimental bench during the PHYSICE project to characterize the effects of rough walls on the dynamic and thermal behaviours of the boundary layer. To that end, both coefficients C_f and C_h are measured. The temperature and velocity profiles were also measured, which is less usual in rough-wall-effect databases (Figure 46). This provides an extended database, investigating in particular k_s^+ up to around 500 and the effect of the shape of rough elements.

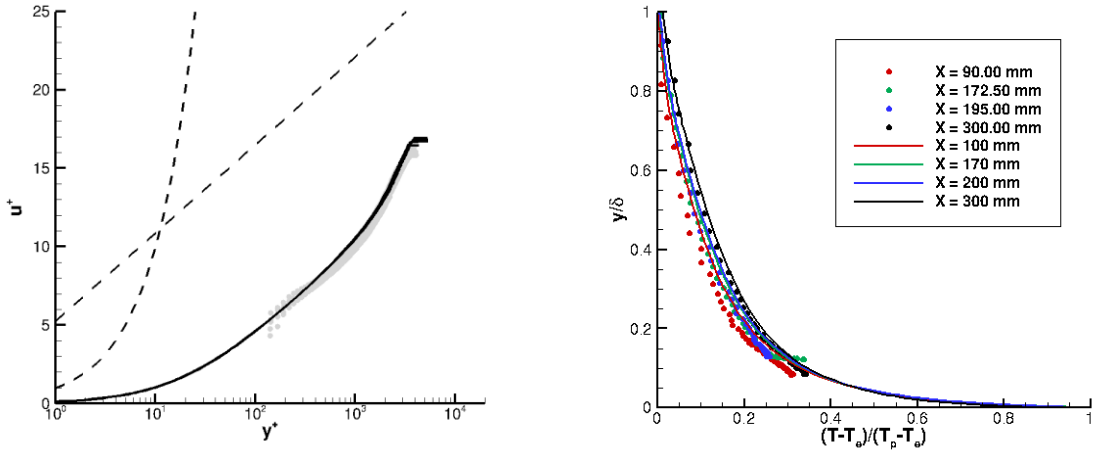

(a) dynamic boundary layer

(b) thermal boundary layers

Figure 46 - Comparison between experiments and CLICET results (low-Reynolds number AGC model) on the ONERA PHYSICE2 test-case number 3.

3.2.2.2.3 Conclusions

Both integral boundary layer and Navier-Stokes approaches are available to deal with rough-wall conditions. The integral boundary layer approach is the usual approach for ice accretion suites. The RANS approach looks more and more interesting, especially for 3D applications. However, the more

recent developments for RANS approaches still need validation for icing applications. Moreover, an advanced characterization of the model inputs is still required. It is also worth mentioning that models for the laminar-turbulent transition on rough walls should also be investigated in the future

3.2.3 Supercooled Large Droplets (SLD)

3.2.3.1 Secondary (re-emitted) droplets [TUDA, ONERA, CIRA, TUBS, POLIMI]

For the prediction of aircraft icing due to SLDs a comprehensive understanding of the drop impact process is essential. This covers not only the behavior of the primary drop and its deposited mass on the cold substrate but also the possible existence of secondary droplets ejected due to the drop impact. The phenomenon of secondary droplets emitting from an impacting drop is called splashing. Various thresholds have been obtained in literature to predict under which conditions splashing occurs and secondary droplets are formed. If the splashing threshold is exceeded and secondary droplets are formed, their characteristics are of particular significance for the icing of the solid substrate. These characteristics cover, among others, the number, sizes and velocities of the secondary droplets. In this section, the most recent literature on these topics is summarized.

3.2.3.1.1 Objectives and issues

With regard to the icing of aircraft, the splashing threshold and the characteristics of secondary droplets have to be investigated for various flight conditions. Due to the advances in modern high-speed cameras drop impacts have been investigated in more detail within the decade. However, most available data corresponds to isothermal drop impacts or heated walls but only little data is available for cold surfaces or supercooled drops. Furthermore, the existing experimental databases on SLDs do not cover all relevant operating conditions of aircraft. Thus, an experimental database covering relevant operating conditions, including shear flow, has to be supplied.

Analogous to the experimental investigations, numerical and theoretical investigations mostly focus on isothermal drop impacts. Moreover, the existing models incorporate a high degree of empiricism. To accurately predict ice accretion, a reliable model for the impact of secondary droplets is needed. Therefore, it must firstly be determined if secondary droplets are emitted and secondly what characteristics these droplets exhibit.

3.2.3.1.2 Literature review

In the following subsections different experimental and numerical studies concerning the characteristics of secondary droplets or its generation are presented. At first, the splashing threshold for wet and dry surfaces is discussed, which is of high relevance since it predicts whether secondary droplets are emitted or not. Subsequently, further studies on splashing and the characteristics (number, size and velocity) of secondary droplets are presented. Since only little research has been conducted on SLD impacts, additionally isothermal impact studies are considered in the following review. Therefore, if not explicitly mentioned in the review the presented studies are for isothermal conditions.

3.2.3.1.2.1 Experimental: Splashing threshold of drops impacting onto wet surfaces

3.2.3.1.2.1.1 Description

The splashing threshold is determined in several experimental studies. Deegan et al. [95] study the drop impingement on a liquid film for various Weber and Reynolds numbers and finds different sources of secondary droplets. An extensive review of different correlations for the splashing threshold of the impact of a drop on a liquid film for isothermal conditions can be found in Liang and Mudawar [96] who also summarize different models for the number of secondary droplets. Okawa et

al. [97] investigated the splashing threshold for moderate impact velocities ($U_0 = 1.4\ to\ 9.6$ m/s.) and for different impingement angles ranging from 11° to 75°.

In the framework of the German research project SFB-TRR 150, several studies concerning the impact of a drop on a liquid film have been performed. Kittel et al. [98] studied the single drop impact onto a thin liquid film of a different liquid. Within this work, viscosities have been varied with the ratio $\kappa = \nu_{film}/\nu_{drop}$ ranging from 10^{-4} to 10^{4}. The impact diameter is in the order of millimeters and the impact velocities varies between $U_0 = 1.7\ to\ 3.2$ m/s.

3.2.3.1.2.1.2 Main results, progress and limitations

A collection of splashing thresholds for drops impinging onto a liquid film given by Liang and Mudawar [96] is shown in Figure 47 for various test conditions. Here the parameter $h^* = h/d_{drop}$ refers to the non-dimensional film thickness. They further notice that correlations based solely on the number $K = We\ Oh^{-0.4}$ are inaccurate to precisely predict the splashing thresholds, since many studies determine that splashing is greatly influenced by gas pressure and gas properties. However, further investigations to improve the accuracy of these correlations are recommended. In addition, the mechanisms of splashing require continuing attention for different operating conditions.

Correlations for critical K required to initiate splashing into small droplets.

Author(s)	Fluids	Test conditions	Correlation(s)
Walzel	Glycerol–water mixtures	$h^* = 0.1$	$K = We\,Oh^{-0.4} = 2500$
Yarin and Weiss	Ethanol, ethanol–glycerol–water mixtures	$d_{drop} = 70$–340 μm, v_{drop} up to 30 m/s	$v_{drop} = \left(\frac{\sigma}{\rho_f}\right)^{1/4} \nu_f^{1/8} f^{3/8}$ simplified to $K = We\,Oh^{-0.4} = 2400$
Cossali et al.	Water, glycerol–water mixtures	$d_{drop} = 3.07 \pm 0.07$–3.51 ± 0.06 mm, $We = 2 \times 10^2$–1.6×10^3, $h^* = 0.1$–1, $Oh > 7 \times 10^{-3}$	$K = We\,Oh^{-0.4} = 2100 + 5880h^{*1.44}$
Marengo and Tropea	Water $\mu_f = 50$ mPa s	– $Oh > 0.01$	$K = We\,Oh^{-0.4} = 2074 + 870h^{*0.23}$ $K = We\,Oh^{-0.4} = 2164 + 7560h^{*1.78}$
Rioboo et al.	Glycerol–water mixtures, hexadecane, $PDMS_5$, $PDMS_{10}$	$We = 28$–890, $h^* > 0.06$, $Oh = 1.14 \times 10^{-2}$–5.48×10^{-2}	$K = We\,Oh^{-0.4} = 2100$
Okawa et al.	Water	$We = 2.5$–980, $h^* = 0.4$–68, $Oh = 1.5 \times 10^{-3}$–7×10^{-3}	$K = We\,Oh^{-0.4} = 2100$
Vander Wal et al.	Heptane, nonane, decane, dodecane, tetradecane, hexadecane, deionized water, 30% glycerol/water, methanol, ethanol, n-propanol and butanol	$Re = 5 \times 10^2$–5×10^3, $Oh = 10^{-3}$–2.2×10^{-3}	$K = Oh\,Re^{1.17} = 63$
Huang and Zhang	Water, oil	$h^* = 0.1$–1, $\rho_f = 854$–998 kg/m^3, $\mu_f = 1$–22.5 mPa s, $\sigma = 0.029$–0.072 N/m	$K = (We\,Re)^{0.25} = 25 + 7h^{*1.44}$
Motzkus et al.	Water, glycerol–water mixtures	$We = 62$–1754, $h^* = 0.3$–1, $Oh = 2 \times 10^{-3}$–1.5×10^{-2}	$K = We\,Oh^{-0.4} = 2100 + 2000h^{*1.44}$
Gao and Li	Water, glycerin–water mixtures	$h^* v_{film} = 0.05$–0.18, $\mu_f = 1$–46.47 mPa s, $\sigma = 0.0657$–0.0714 N/m	$K = We\,Re^{0.5} = 3378(1 + h^* \nu_{film}^{*2})^{-1}(1 + h^* \nu_{film}^{*})^{-0.5}$

Figure 47 - Definitions of splashing thresholds of drop impingements on a liquid film and their test conditions. Taken from Liang and Mudawar [96]. (Permissions are needed)

The results of Okawa et al. [97] on the deposition–splashing limit for oblique drop impacts are presented in Figure 48. Okawa et al. obtained a good prediction of the splashing threshold when calculated with the absolute value of the velocity vector. When the impingement angle was less than $\alpha \leq 50°$ an increase in the impingement angle led to a significant increase in secondary drop size and consequently in the total mass of secondary drops. However, no secondary drop was observed within the experimental ranges tested when the impingement angle exceeded $\alpha > 70°$.

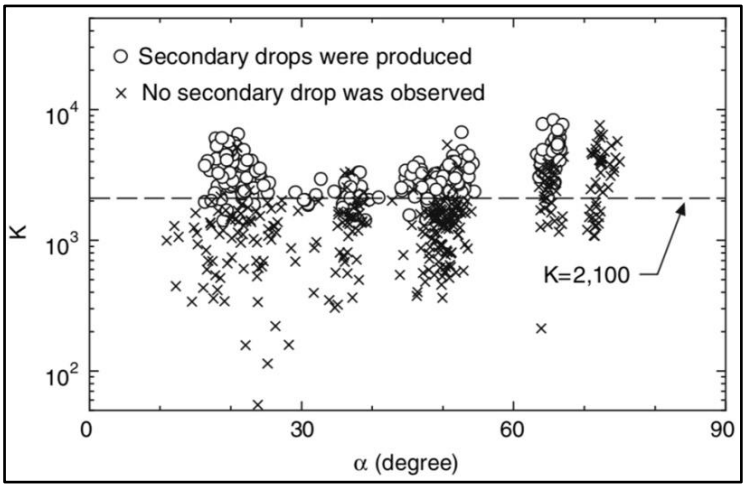

Figure 48 - $K = We\ Oh^{-0.4}$ calculated from the absolute value of the velocity vector for different impact angles. Taken from Okawa [97]. (Permissions are needed)

Kittel et al. [98] determined three regions with splashes when two different liquids were used for drop and film. If the kinematic viscosity of the film is much smaller than the viscosity of the drop the splash is determined by the K number defined by $K = We^{0.5}\ Re^{0.25}$ based on the properties of the wall film. If the viscosity of the film is much larger than the viscosity of the drop, the splash is primarily influenced by the K number based on the properties of the liquid drop. For the third region of the viscosity ratio, it is assumed that the splash is initiated in the liquid with the smaller surface tension. The splashing threshold K^* in this case is proposed as

$$K^* = Re_d^{1/4}\ We^{*1/2}, \quad We^* = \frac{(\rho_f+\rho_d)D_{\text{primary}}\,v_0}{2\ \min(\sigma_d;\sigma_f)},$$

where the subscript d denotes the liquid of the drop and f the liquid of the film. As seen in Figure 49 the critical K^* number the splashing threshold is found to be a function of the term $(\kappa-1)\kappa^{-3/5}$ with the viscosity ratio $= \nu_f/\nu_d$. The scaling is proposed based on the assumption that splash is initiated in the liquid layer with smaller surface tension.

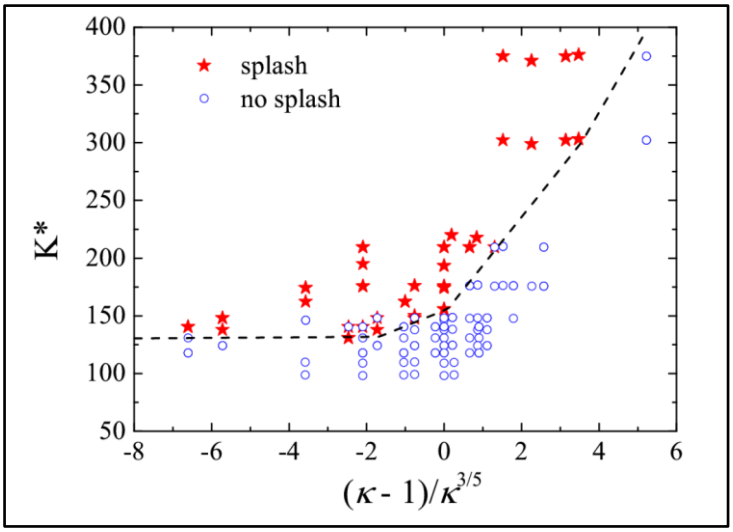

Figure 49 - Map of the experimentally observed outcomes of drop impact onto a liquid pool, when the viscosities of the drop and wall film liquids are comparable. Taken from Kittel et al. [98] (Permissions are needed)

3.2.3.1.2.2 Experimental: Splashing threshold of drops impacting onto dry surfaces

3.2.3.1.2.2.1 Description

As concluded by Yarin [99] the impact of drops onto a dry surface exhibits a more complicated behaviour since the effects of roughness and wettability of the substrate have to be taken into account. Tang et al. [100] performed investigations on single drop impingement on a dry wall under isothermal conditions and paid special attention to the influence of the roughness of the wall.

Within the framework of the German research project SFB-TRR 75, Li [101] performed experiments on high speed drop impacts (10 m/s – 63 m/s) onto inclined surfaces (0° – 75°). Within the same project, Roisman et al. [102] performed investigations on the influence of roughness and porosity.

In the framework of the German research project SFB-TRR 150, Kittel et al. [103] investigated the impact of a drop on a solid substrate covered by a thin soft visco-elastic PDMS layer. The elastic and viscous properties of the thin layer were varied in a wide range.

In the framework of the French research project PHYSICE2, the splashing threshold for SLD impact for very high impact velocities has been studied [104] [105]. The main objective of the experiment was to define the threshold between the bouncing and splashing regimes for very low impact angles. This aspect was partially addressed in PHYSICE1 but no progress was made at that time due to a lack of technical solution. The difficulty of accurately locating the droplets before impact makes it difficult to visualize the impact. In the PHYSICE2 measurement campaign, the flat wall previously used was replaced by a cylinder with a large diameter relative to the drops, so the variation in the position of the drop results in a variation in the impact angle (Figure 50).

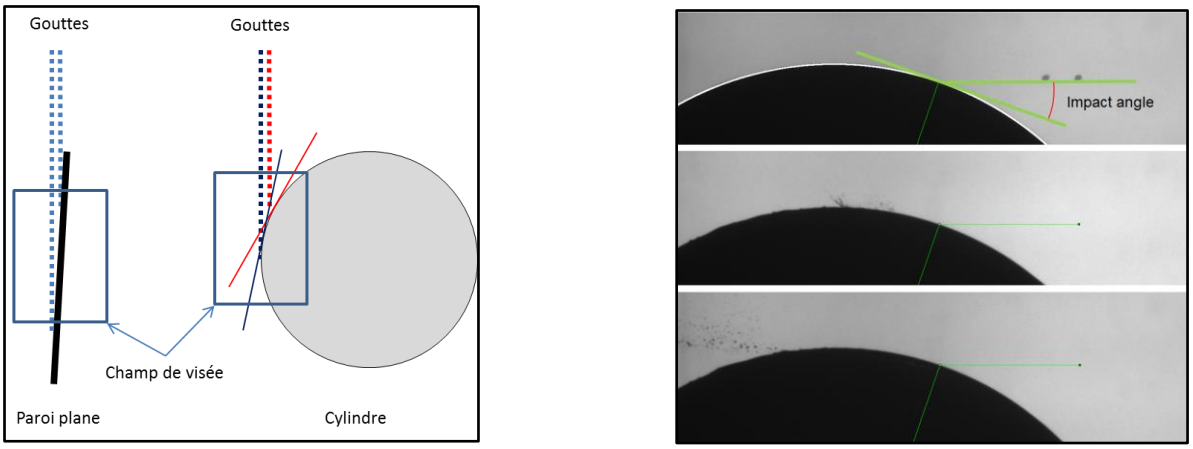

Figure 50 - Installation for the characterization of the bouncing threshold

A parametric study was carried out by varying the impact conditions:

- air velocities (40 m/s, 60 m/s and 80 m/s);
- drop diameters (250 µm and 400 µm);
- wall materials (aluminum and Teflon).

3.2.3.1.2.2.2 Main results, progress and limitations

A summary of previous empirical models for the splashing threshold onto dry surfaces given by Tang et al. [100] is shown in Figure 51. The authors mainly addressed the influence of the surface roughness for the splashing threshold.

Previous empirical models regarding the splashing threshold.

Refs.	Droplet, surface combination, roughness range, if specified	Splashing threshold criterion
Stow and Hadfield (1981)	Water, with stainless steel and aluminum surface R_a 0.05–12	$D_0\ U_0^{1.69} \sim R_a$
Mundo et al. (1995)	Ethanol, water, water-sucrose-ethanol, with stainless steel surface, R_t= 2.8&78μm	$K = OhRe^{1.25} = 57.7$
Cossali et al. (1997)	Data from Stow and Hadfield (1981) and Mundo et al. (1995)	$K = (WeOh^{-0.4}) = 649 + 3.76(R_a/D_0)^{-0.63}$
Range and Feuillebois (1998)	Water-glycerol mixtures, and ethanol, with paper, glass, plexiglas, and aluminum surfaces with different roughness	$^{\#}We_{cr} = a\ \log^b(R_0/R_a)$.

[#] The values of fitting constants a and b depend on their droplet -solid surface combinations.

Figure 51 - Empirical models for the splashing threshold with a focus on the influence of surface roughness. Taken from Tang et al. [100]. (Permissions are needed)

For their own experimental data, they proposed the following empirical correlation for the critical K number:

$$K_{\mathrm{cr}} = \left(\frac{We}{Oh}\right)^{\frac{1}{2}}_{\mathrm{cr}} = c + d\ \ln\frac{R_a}{D_0}.$$

Here, the critical splashing threshold is expressed as a function of the mean roughness R_a of the dry impact surface, which is the arithmetic average of the absolute values of the roughness profile ordinates, and the initial drop diameter with two fitted parameters c and d, depending on different liquids. The proposed correlation shows reasonably good agreement with different literature data.

Roisman et al. [102] noticed that the splashing threshold is mainly influenced by the Weber number of the impinging drop and the characteristic slope of the substrate morphology, $\mathrm{Rpk}/\mathrm{Rsm}$, where Rpk is the average height of peaks above roughness core profile and Rsm the mean width of the profile elements. However, no significant influence of the pore size of the porous targets was observed. Roisman et al. [102] further showed a map of drop impact onto a dry wall for various literature data under isothermal conditions, depicted in Figure 52.

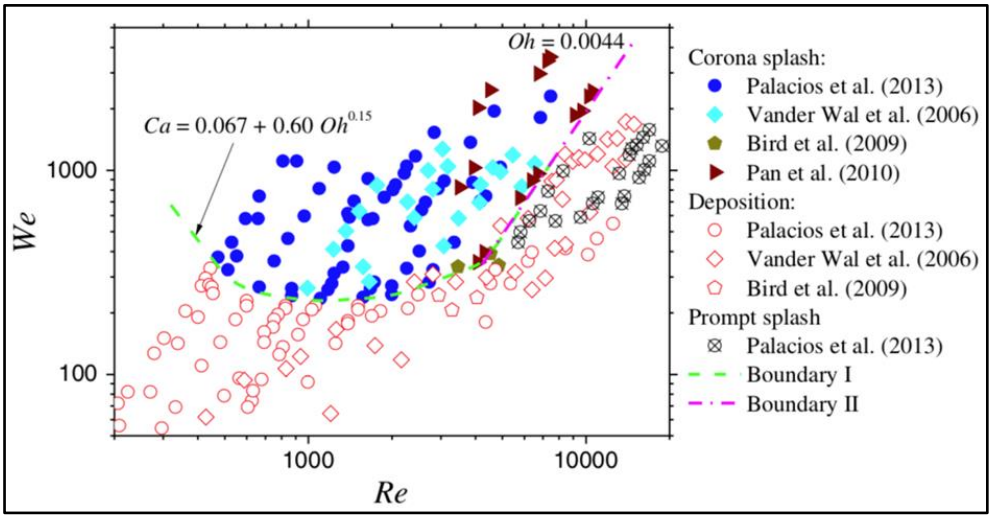

Figure 52 - Collection of different literature experiments to determine the splashing threshold. Taken from Roisman et al. [102]. (Permissions are needed)

Noteworthy is the fact, that different definitions of the K number are used in literature. A short summary of the various definitions is given by Moreira et al. [106] and shown in Figure 53. According to Roisman et al. [102], the K number defined by $K = We^{0.5}\ Re^{0.25}$ does not describe the splashing threshold well. Further formulations of the splashing threshold were examined in Marengo et al. [107] indicating that no adequate formulation is known at this time and that some formulations contradict each other.

Xu et al. [108] noticed a dependency of the splashing threshold on ambient pressure which was also confirmed by Roisman et al. [102] who noticed that not only the threshold for corona splash increases with decreasing pressure, but also the threshold for a prompt splash.

Kittel et al. [103] found that the critical K number defined by $K = We\ Re^{-2/5}$ is higher for impacts on the deformable substrate than on a rigid wall.

Summary of the disintegration criteria proposed in the literature.

Reference	$K_c = A\,Oh^a We^b$			Boundary conditions	Observations
	A	a	b		
Stow and Hadfield	1	−0.37	1	Dry surfaces with different roughness.	$K_c = f(R_a)$ – the parameters a and b were adjusted as a function of R_a in a logarithmical empirical adjustment. It is not explicit of which disintegration mechanism is being considered because the correlation is also adjusted to measurements of Stow and Stainer [66] who considered a wide range of data for impacts onto liquid films. Overall it is interpreted that the correlation was developed for prompt splash.
Wu	1	0	1	Dry surfaces with different roughness.	Took the correlation of Stow and Hadfield [60], considering that for their experimental conditions Oh could be neglected. $K_c = We_c = f(R_a) = A_1 \log(R_a/R_0)^{b_1}$ where $A1$ and b_1 depend on the properties of the liquid and on the nature of the surface [36,47].
Mundo et al.	1	−0.4	1	Wetted surfaces with different roughness.	The authors compared 2 surfaces with very different roughness but did not observe relevant differences so that for them K_c does not depend on R_a. Later, Mundo et al. [67] recognized the presence of a liquid film over the surfaces which should explain the minor importance of the surface roughness.
Bai and Gosman	Depends on surface roughness	0.36	0	Dry surfaces.	The correlation for dry surfaces was adjusted to the data of Stow and Hadfield [60].
Gavaises et al.	1	0	1	–	$K_c = We_c = 100$ – major limitation is to consider a constant value for the threshold. Care must be taken before neglecting viscous effects [36,69].
Randy et al.	1	0.4	−0.3	Dry smooth surfaces.	The correlation fits well the experimental data for high Reynolds numbers (Re > 7000) but larger discrepancies with the experimental data are found as the inertial forces become less important (Re < 3000).

Figure 53 - Expressions for the splashing threshold of impingement on a dry wall. Taken from Moreira et al. [106].

In PHYSICE2 observations [104] [105], no influences of the drop diameter or the surface material were observed on the threshold between bouncing and splashing regimes. The main influencing parameter on the splashing threshold seems to be the normal impact velocity. Figure 54 presents the rebound probability as a function of the impact angle for different impact velocities. The figure gathers all the experimental data including two diameter values (250 µm and 400 µm) and two material surfaces (aluminum and Teflon). Transition between splashing and bouncing occurs between 9° and 15° regardless of droplet impact velocity and diameter.

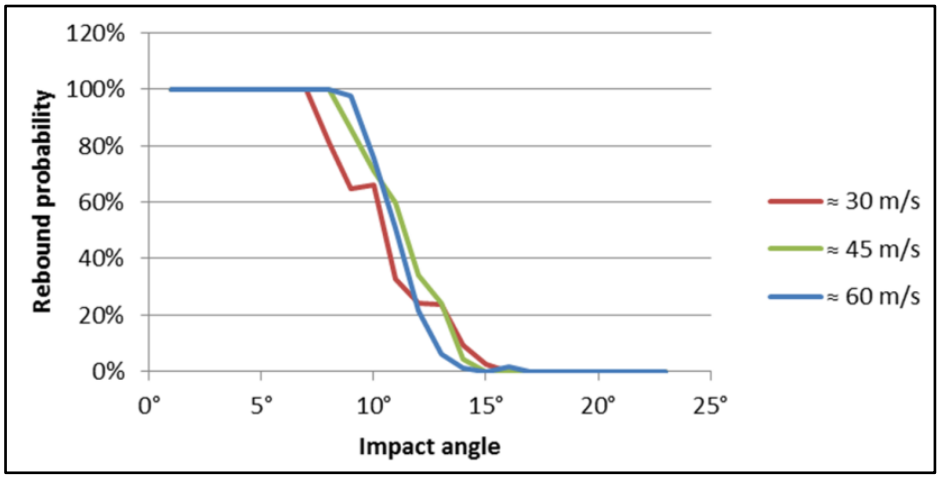

Figure 54 - Impact regime vs. the impact angle for different impact velocities.

3.2.3.1.2.3 Numerical: Computation of splashing and bouncing phenomena in a Eulerian frame

3.2.3.1.2.3.1 Description

Due to the nature of the Eulerian approach, modelling water reinjection due to droplet splashing and bouncing is less straightforward than in the Lagrangian case. Indeed, while the primary impingement flow can be still conceived as a continuous medium, the secondary particle flow generated by particle impacts is inherently discrete as the continuity is broken and re-emitted particles with different size, velocity and angle are generated. Nevertheless, the advantages of an Eulerian framework can still be kept by defining a conservative model which takes into account either the mass loss at the wall and the re-impingement of ejected particles further back.

The approach allows to separate the transport of the primary cloud from the secondary emission. Indeed, the latter computation is only needed to evaluate re-impingement effects on downstream part of the bodies due to particle mass emission from the fore part of the body. The model operates a decoupling of pre- and post-impact droplet boundary conditions and neglects any interaction between rebounding droplets and particles on their primary impingement trajectories. The pre-impact solution considers the airfoil surface as an outflow boundary by enforcing Neumann boundary conditions. On the other hand and from the point of view of the re-emitted or secondary particles, the post-impact solution models each face on the airfoil surface (on which primary impingement occurred) separately as an inflow boundary, while the other regions of the airfoil where primary impingement is null are treated as an exit boundary. Secondary droplets may impinge on the airfoil and produce ternary particles. The inflow and exit boundaries are re-defined according to the impingement of the secondary droplets and a post-model calculation calculated for the ternary ones and so on and so forth. By decoupling the pre- and post-impact simulations, the boundary condition duality of trying to model the surface as both inlet and exit simultaneously is avoided.

The simulation of droplet impingement with splashing, bouncing, and reinjection in a conservative Eulerian framework can be described as follows:

1. The primary incoming droplet impingement locations and mass caught are computed in the classical Eulerian manner;
2. The primary impingement solution is post-processed to determine the mass of water to remove due to splashing/bouncing (thanks to an impact model), and then the average diameter, angle, velocity, and concentration of the droplets to be reinjected are computed. The water remaining in the post-processed primary impingement solution contains the mass of water that sticks/spreads on the surface, and requires no additional treatment;
3. The droplets in the splashing/bouncing regions are reinjected after converting individual facets of the surface mesh to inlet boundaries;
4. The overall impingement coefficient distribution is the sum of the post-processed and corresponding reinjected droplet solutions. It is computed as follows:

$$\beta_{final} = \frac{LWC_{final} V_{n,final}}{LWC_{\infty} V_{\infty}},$$

$$LWC_{final} = LWC_i - LWC_s + LWC_{reimpinge},$$

where LWC_i denotes the primary impinging LWC, LWC_s is computed from an impact model and $LWC_{reimpinge}$ is the mass-weighted summation of the reinjection solutions.

3.2.3.1.2.3.2 Main results, progress and limitations

The group of Habashi [109] [110] [111] conducted a preliminary validation of the proposed approach by comparing numerical solutions to the experimental data of Papadakis et al. [112] on the clean and three ice-contaminated geometries of a NACA 23012 airfoil, and a clean MS(1)-0317 airfoil. The flow solver used for all the calculations is FENSAP, a finite element formulation of the Navier–Stokes

equations, with the Spalart–Allmaras turbulence model. Droplet impingement was computed with DROP3D, also a finite element formulation corresponding to the water-mass and momentum conservation equations. The contaminated geometries considered were the NACA 23012 after a 5 min glaze-ice buildup period, the NACA 23012 after a 45 min glaze-ice buildup resulting in a leading-edge double-horn glaze-ice shape, and the NACA 23012 after a 45 min rime-ice buildup period. Figure 55 and Figure 56 show an example of the beneficial correction introduced by the reinjection method on the impingement curve prediction. Figure 57 depicts the primary and secondary clouds as LWC contour map.

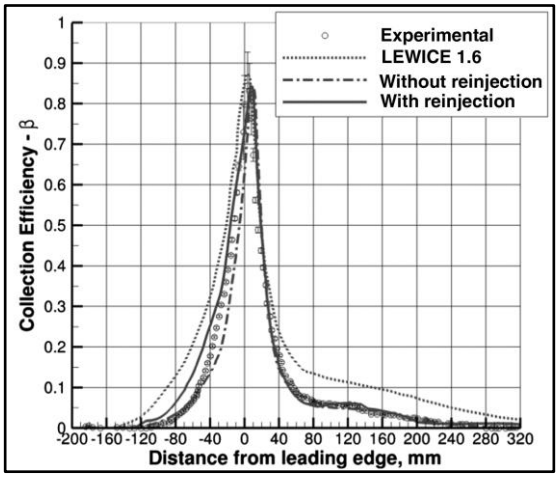

Figure 55 - NACA 23012 airfoil @ MVD=111 µm

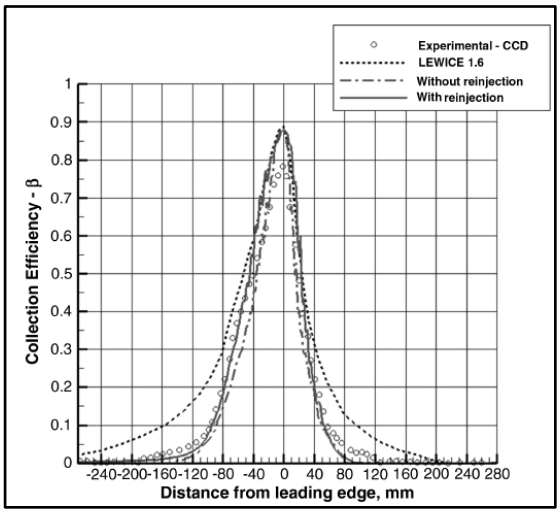

Figure 56 - MS(1)-317 airfoil @ MVD=137 µm

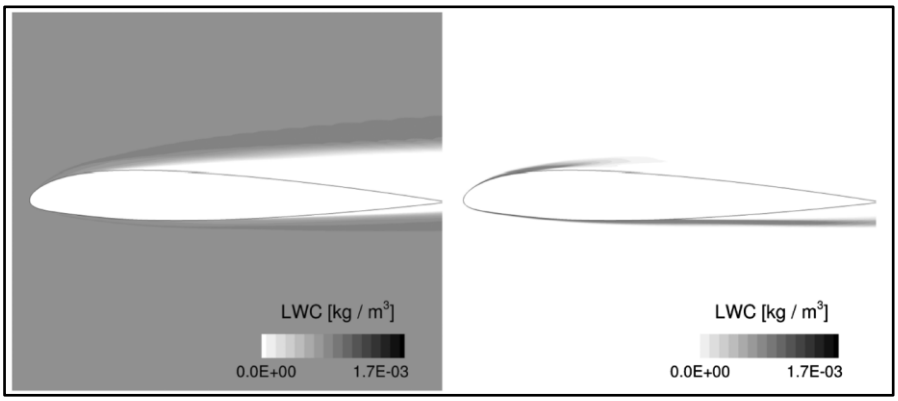

Figure 57 - LWC contours for the primary (left) and reinjected (right) droplet solutions

Almost simultaneously, Iuliano et al. [113] [114] developed a similar methodology to take into account splashing/bouncing (for liquid particles) and shattering (for solid particles) effects on the impingement simulation in a Eulerian frame. The idea is to realize a “cascade” of mass from larger to smaller bins by means of the releasing-receiving bin mechanism. Similarly to Habashi et al., the boundary conditions are automatically changed in order to switch the impingement walls into inlet patches, while the far-field inlet values are turned to null. Finally, the overall impingement coefficient is computed as the mass-weighted summation of the reinjection solutions. Figure 58 shows the volume fraction and particle trajectories of both primary and re-injected ice crystals clouds around a wedge airfoil for three bin sizes (namely 60, 220 and 380 µm from top to bottom). The solution will depend upon the particle type and the impact model that provides the ejected mass, particle size and velocity.

However, a general frame is provided where different scenarios (SLD, glaciated and mixed-phase conditions) can be simulated.

Of course, the major limitation of such methods is the computational cost. Given *n* the number of bins in the particle distribution, the simulation requires 2*n* Eulerian simulations in order to compute the mass-weighted impingement coefficient. As done by Habashi's group, the computational cost can be lowered by limiting the computational domain of the reinjected droplets and defining smaller subgrids. However, even with the use of local subgrids, the solution cost increases significantly as the simulation of secondary particles is stiffer. An average increase of five to nine times the cost of the primary impingement solution has been observed.

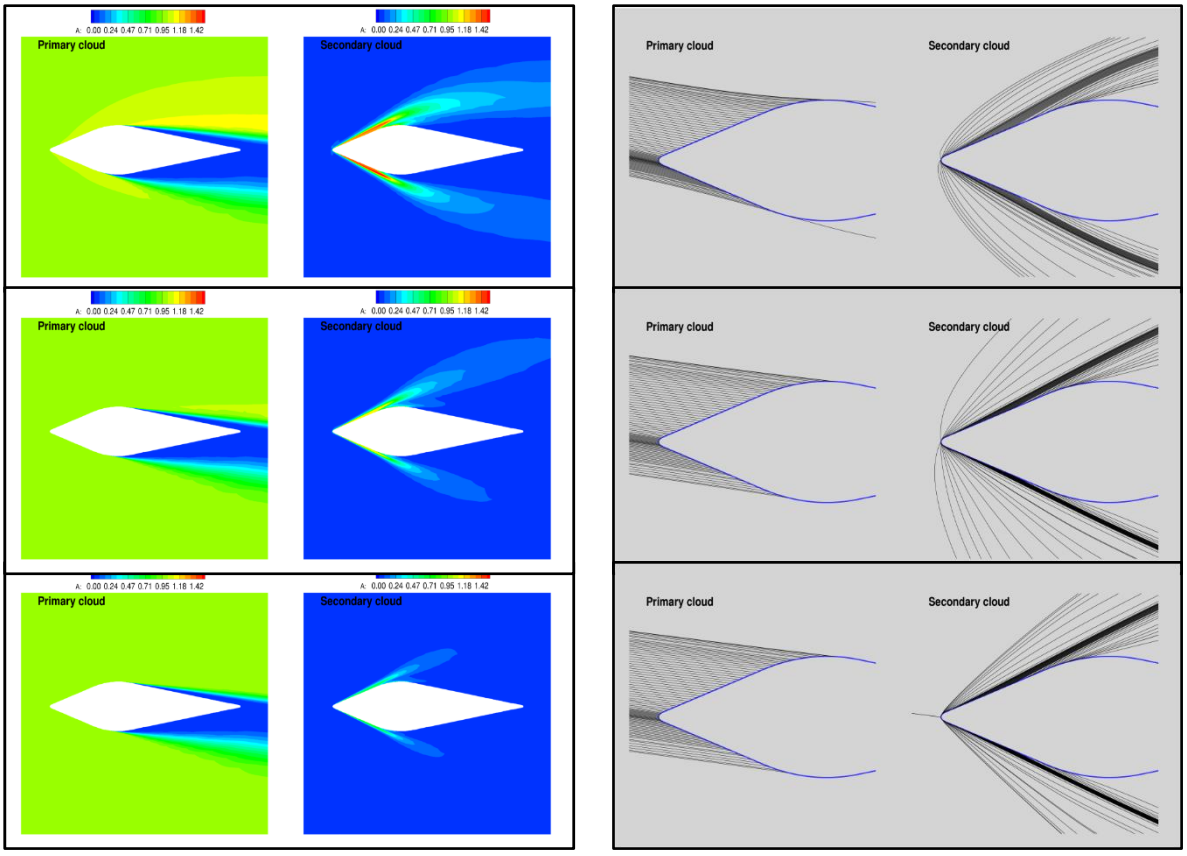

Figure 58 - Volume fraction (left) and trajectories (right) of primary and re-injected clouds

3.2.3.1.2.4 Experimental: Observations of the impact of a high-velocity droplets

3.2.3.1.2.4.1 Description

In the framework of the French project PHYSICE2, detailed experimental description of the impact of a high-velocity droplet has been obtained. The objective is to improve the observation of the droplet impingement. An optical method of triggering for image acquisition has been developed to capture different moments from the initial time [104]. The introduction of a variable delay time (using a delay generator) between drop detection and the start of image acquisition allowed the recording of instantaneous images of the impact over a wide range of instants. The impact dynamics was described by sorting the instantaneous images corresponding to different drops with the same size and speed characteristics. This made it possible to capture the different phases of the impact and thus, to reconstruct the entire dynamic of the phenomenon.

The conditions are the following:

- Injected droplet diameter between 250 and 650 µm;
- Air velocity between 30 and 110 m/s (at the convergent exit);
- 3 substrates: polished and rough aluminum, blotting paper.

3.2.3.1.2.4.2 Main results, progress and limitations

Figure 59 represents the droplet size and velocity distribution for different air velocities.

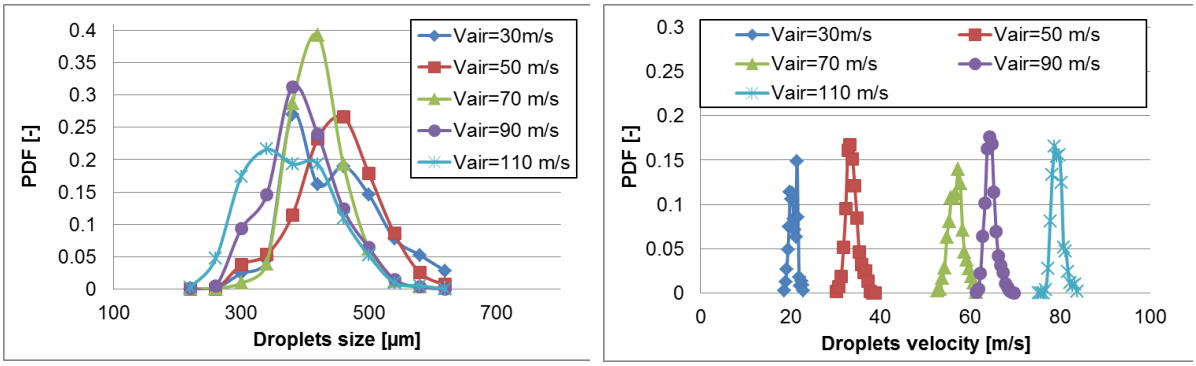

Figure 59 - Droplet diameter and velocity before the impact.

The visualization of the normal impact of SLDs on the polished aluminum, rough aluminum and blotting paper (resp. Figure 60, Figure 61 and Figure 62) revealed a clear difference between a wall made of rigid aluminum surface and a wall covered by an absorbent surface (blotting paper). In the first case (rigid wall), the formation of the characteristic structures of the "corona splash" is clearly observed: a crown that detaches itself from the wall and is then transformed into small secondary droplets further dispersed in the carrying flow. At high impact velocities, the crown is no longer present. The liquid film generated at the contact line with the wall disintegrates rather by a mechanism close to the "prompt splash" regime which is associated with the appearance of a larger number of secondary droplets. Regarding the impact on the blotting paper, no characteristic splash mechanism was found. The number of secondary drops is very low and the drop is quickly absorbed into the wall.

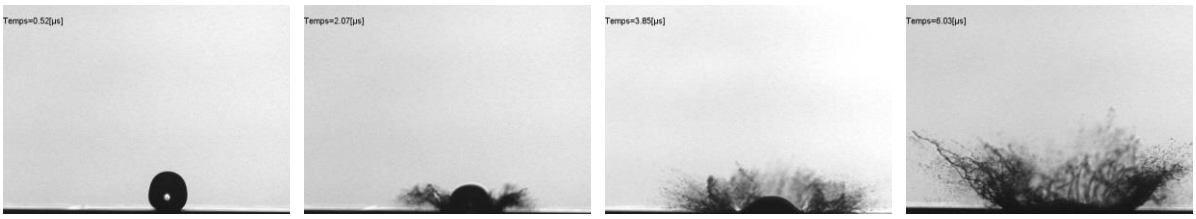

Figure 60 - normal impact on a polished aluminum surface. We=33300 ; D=375µm ; Vd=80m/s

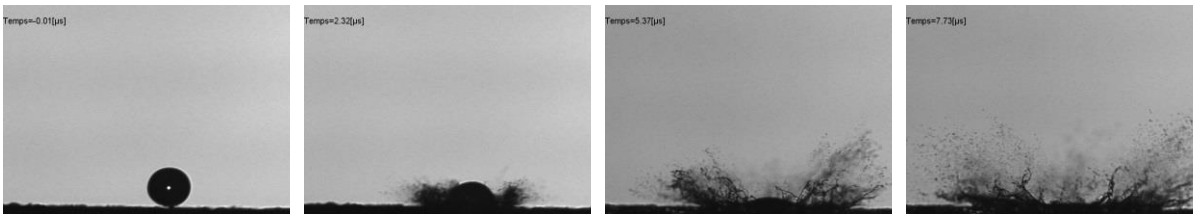

Figure 61 - normal impact on a rough aluminium surface. We=22000 ; D=375µm ; Vd=65m/s

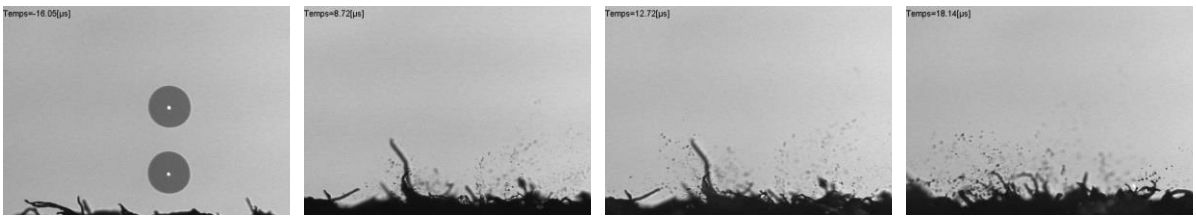

Figure 62 - normal impact on a surface covered by a blotting paper. We=17500 ; D=375µm ; Vd=58m/s

3.2.3.1.2.5 Numeric: Direct numerical simulation of the high speed drop impact

3.2.3.1.2.5.1 Description

In the framework of the French research project PHYSICE2 the SLD impact is also studied numerically. The objective is the direct numerical simulation (DNS) of the wall impact of SLDs to understand the detailed physical mechanisms and capture the smallest time and space scales that cannot be measured by experimental means [104] [115]. The methodology was tested firstly for the impact on dry and wet walls at low velocity. For higher velocities, the parameters are:

- Droplet diameter = 420 µm
- Impact velocity = 20 m/s
- Density ratio $\frac{\rho_L}{\rho_g}$ between 100 and 1000

leading to a Reynolds number of $\sim 10^4$ and a Weber number of $\sim 2.0 \times 10^3$ based on the droplet diameter, the impact velocity and the water density.

3.2.3.1.2.5.2 Main results, progress and limitations

On the dry wall, no splash was observed with the level-set method. On the other hand, with the CLSVOF method [116], prompt splash is observed (with secondary droplet ejection at the first steps of the impact) but without the expected liquid corona. The influence of parameters such as density ratio (Figure 63) and wall pre-filming thickness (Figure 64) wall was studied. Tricks like decreasing the density ratio were necessary to observe droplet breakup [117]. The thickness of the film on the wall seems to have a great influence on the impact dynamics.

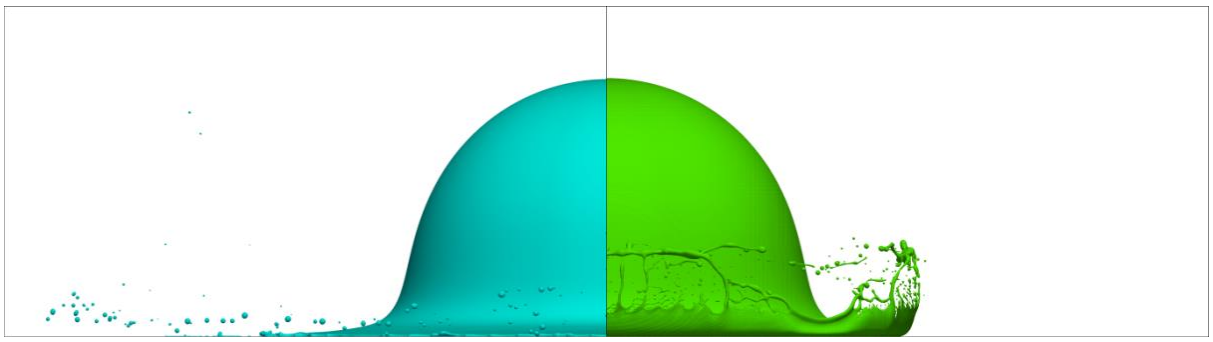

Figure 63- Influence of the density ratio $\frac{\rho_L}{\rho_g}$. Left: $\rho_g = 1.2\ kg/m^3$. Right :$\rho_g = 12\ kg/m^3$. A corona is observed with high air density, contrary to the lower air density. V=20 m/s. D=420 µm.

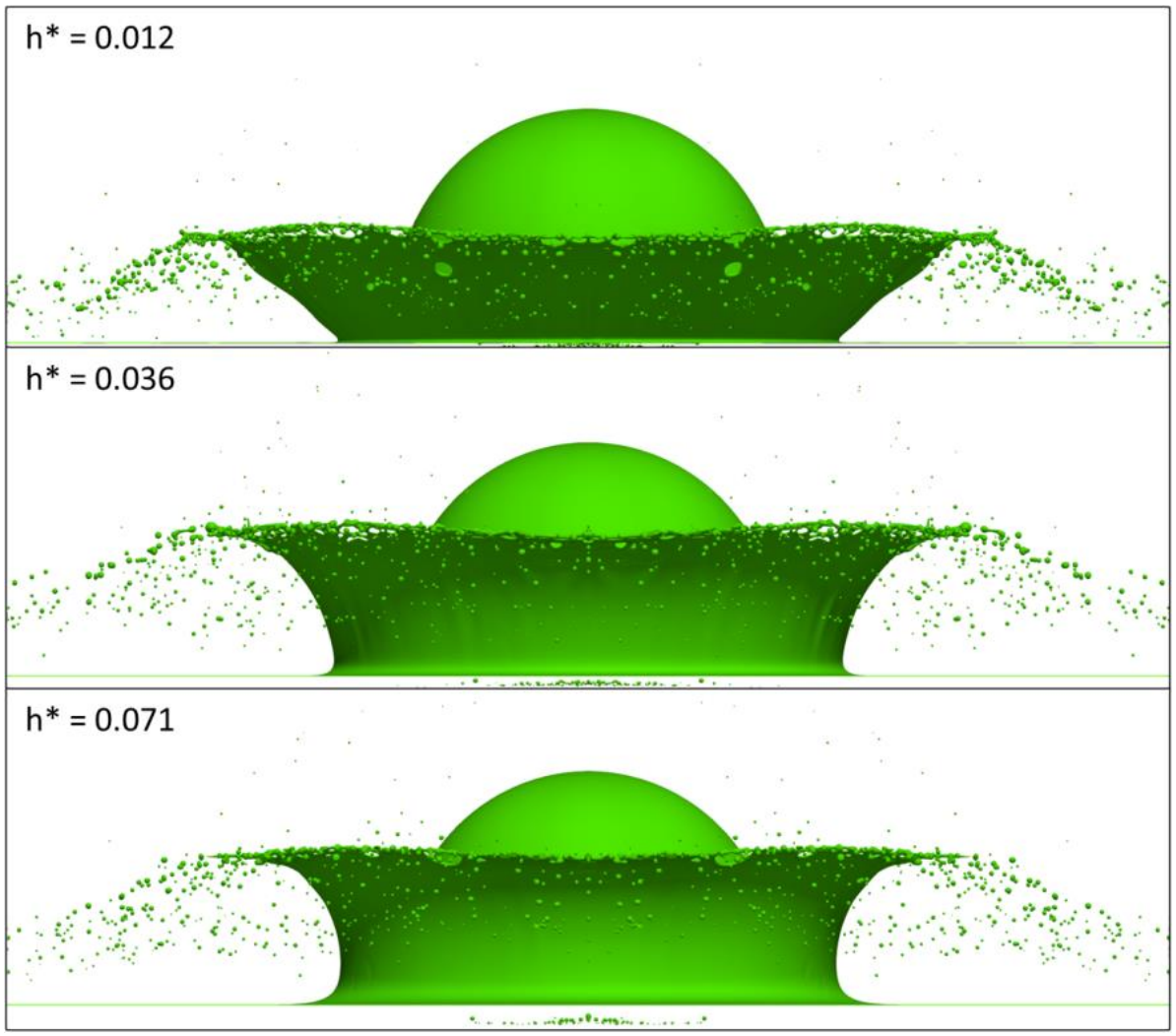

Figure 64 - Droplet impact for different pre-filming thicknesses. See Figure 63 for the numerical parameters.

3.2.3.1.2.6 Experimental: Characteristics of the secondary droplets due to drop splashing onto dry and wetted walls

3.2.3.1.2.6.1 Description

Riboux and Gordillo [118] experimentally investigated the impact of drops of different liquids onto a dry wall and developed a model describing various characteristics of the splash. They build their theory on a previously developed model for the splashing threshold [119], which may not be limited to low velocities as shown by Burzinsky and Bansmer [120].

Besides the splashing threshold, Okawa et al. [97] also investigated the effect of impact angle on the total mass of secondary drops produced during drop impact onto a water surface. The authors performed experiments of single water drop impact onto a plane water surface with an inclined impact angle ranges from 11° to 75°. The impact velocity is in the range from $U = 1 - 10$ m/s.

In the framework of the German research project DFG BA4953-3, the droplet impact onto dry and wet surfaces at high Weber numbers (We>2000) is currently being investigated by Burzynski and Bansmer [121] [120] [122]. The main goals of the project are to understand the underlying physics of secondary droplet generation at high impact velocities, and to generate a useful database for engineering applications that includes a full description of the impact. Some of those aspects in the database are: the total number of ejected droplets, their size and velocity distributions, and the mass loss ratio.

3.2.3.1.2.6.2 Main results, progress and limitations

A collection of models for the number of secondary droplets forming after impact onto a wetted surface was given by Liang and Mudawar [96]. They are shown in Figure 65 and only valid for drops impacting onto a liquid film.

Correlations for number of secondary droplets.

Authors	Fluids	Test conditions	Correlation
Yarin and Weiss	Ethanol, mixtures of ethanol, glycerol and water	d_{drop} = 70–340 μm, v_{drop} up to 30 m/s	$N = \frac{15\pi D^2}{4.5}$
Cossali et al.	Water	d_{drop} = 3.82 ± 4% mm, v_{drop} = 2.3–4.4 m/s, h = 1.1–4.3 mm, h^* = 0.29–1.13	$N = C\tau^n$, n increases with increasing We
Okawa et al.	Water	We = 2.5–980, Oh = 1.5 × 10^{-3}–8.4 × 10^{-3}, h^* = 0.43–68	$N = 7.84 \times 10^{-6} K^{1.8} h^{*-0.3}$, where $K = We\ Oh^{-0.4}$

Figure 65 - Correlations for the number of secondary droplets forming after an impact on a liquid film. Taken from Liang and Mudawar [96].

Riboux and Gordillo [118] divide the geometry of the splash into different regions. In the first region the inflow from the drop to the lamella is decelerated at its root due to viscosity. In the second region the liquid sheet detaches from the wall. This point marks the beginning of the second region where the radial velocity is conserved until the liquid enters the rim. In this third region the rim is accelerated due to the inflow of liquid and decelerated due to capillary forces. Secondary droplets are then ejected due to capillary and Rayleigh-Taylor instabilities. The authors specify the time instance at which secondary droplets are ejected as the time at which the ratio of characteristic times of growth of the rim thickness and of capillary instabilities reaches its minimum. The diameters of the secondary droplets are assumed to be equal to the thickness of the rim. Similarly, the velocity of the secondary droplets is taken to be the velocity of the rim. The authors noticed limitations of their model when considering liquids with higher viscosities. However, good agreement of theoretical and experimental data was observed as can be seen in Figure 66.

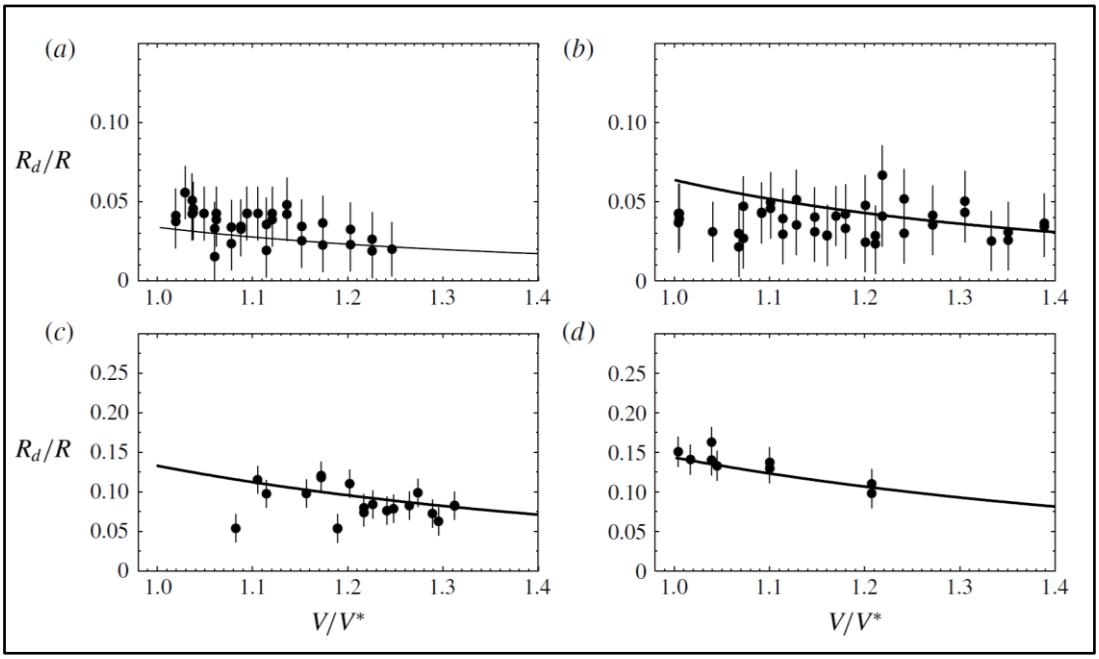

Figure 66 - Comparison of the predicted radius of the secondary droplets ejected with experimentally measured values for (a) ethanol, (b) decamethyltetrasiloxane, (c) poly(dimethylsiloxane) and (d) 10 cP silicone oil. On the vertical axis the ratio of the radius of the secondary droplet to the primary droplet is shown and on the horizontal axis the ratio of the impact velocity to the critical velocity for splashing to occur is given. Taken from Riboux and Gordillo [118]. (Permission to reprint required).

Okawa et al [97] summarized the findings for the influence of impact angle on the total mass of secondary drops as follows:

- If the angle is not very large (10° – 50°) the secondary droplet size increases significantly with the angle while the number of secondary droplets is rather insensitive;
- At higher angles (50° – 70°) the size of the secondary droplets decreases slightly and their number decreases significantly;
- For even higher angles (>70°) no secondary droplets can be observed and the authors followed that the drop's energy contributes to a flow in the liquid film.

Experiments within the German research project DFG BA4953-3 conducted by Burzynski and Bansmer [121] for the impact on dry surfaces have shown that the amount of produced secondary droplets increases with the impact velocity; however, some parameters seem to be not affected by this velocity increment. The high speed images taken in their study show that at $\tau = \frac{D_0}{U_0} = 2$ the majority of the secondary droplets were already generated, indicating that the total volume is ejected until ~ 0.6 ms after impact. Undergoing investigations are showing that the secondary droplet size depends only on the Reynolds number. This result leads to a very accurate prediction of the droplets size and is going to be published soon. Preliminary results for the characteristics of secondary droplets and the influence of the surrounding gas (work in progress) are shown in Figure 67 [122].

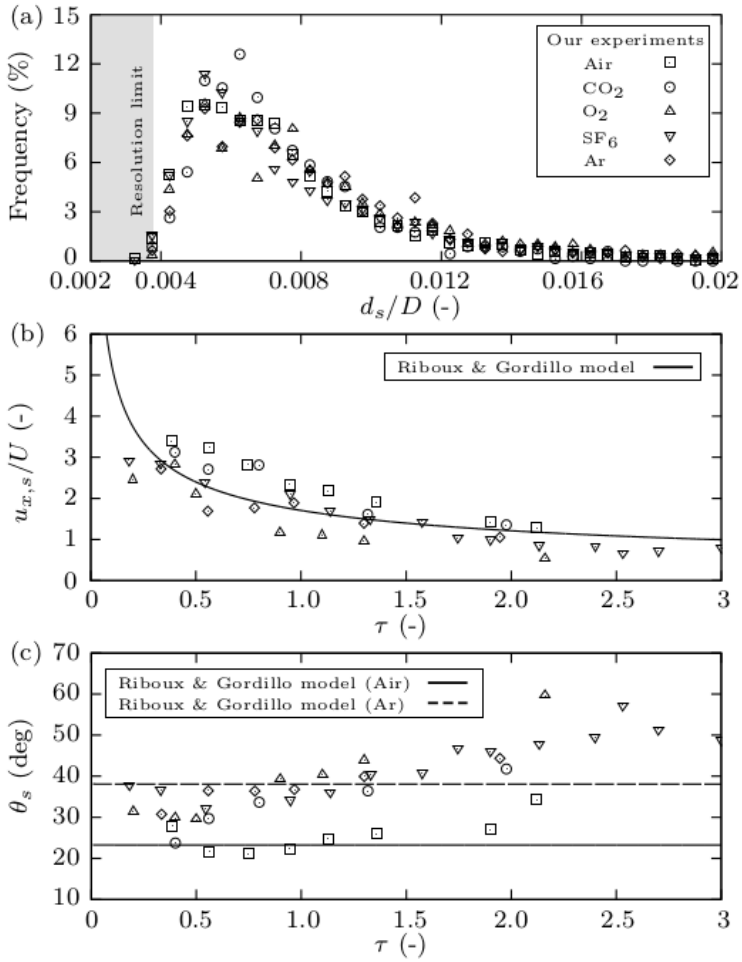

Figure 67 - The ejected secondary droplets during drop impact. (a) shows the droplet size distribution, which is independent of the surrounding gas. (b) shows the horizontal velocity as a function of time, which is also independent of the gas. (c) shows the angle of the droplets relative to the surface as a function of time. Taken from Burzynski and Bansmer [122]. (Permission to reprint required).

To investigate the impact of droplets onto wetted surfaces, Burzynski & Bansmer [120] additionally designed a new recirculation system in the experiment that allows for the generation of a thin moving film during the rotation of the flywheel. In their work, they described the effect of the film velocity on the crown geometry and observed that the crown completely destroys itself due to two instabilities: hole formation and crown base separation. This combined crown breakup generates more secondary droplets than the one produced by rim instabilities. It has also been shown that this crown breakup is delayed by increasing the film velocity. They also provided an estimation of the crown thickness showing that it is constant and approximatively equals to 30 µm. Their description of the crown geometry and its thickness can be used to estimate the total volume ejected due to crown breakup; because the crown geometry is completely transformed into secondary droplets. The upcoming investigations at TUBS will continue with the description and modelling of the impact outcome for several parameters.

3.2.3.1.2.7 Numeric: Characteristics of the secondary droplets due to high speed drop impact

3.2.3.1.2.7.1 Description

Cimpeanu and Papageorgiou [123] conducted three-dimensional numerical simulations on high speed water drop impacts (78.44 m/s) at various angles and amongst other things, analyze the size of secondary droplets. The authors utilize the software Gerris for their simulations, which solves the

incompressible Navier-Stokes equations (DNS) with the volume-of-fluid method and allows adaptive mesh refinement. This kind of simulation is similar to the previous one shown in PHYSICE project. They simulate the impingement for drop sizes below 1 mm transported by an oblique stagnation point flow.

3.2.3.1.2.7.2 Main results, progress and limitations

Cimpeanu and Papageorgiou [123] obtained from their simulations that the average number of secondary drops increases with the size of the primary drop. Droplets detach from the rim in all directions but with a preference towards the direction of impact. The number of secondary droplets is illustrated on the left side in Figure 68 for different primary drop sizes: 20 µm, 52 µm, 111 µm and 236 µm. The drop size distribution for the 236 µm case is shown on the right side of the figure for two time instants. It should be noted, that the primary drop is initialized at $t = 0$ and impacts at the dimensionless time $t \approx 20$. The authors state that the volume of the emitted secondary droplets can be approximately represented by a log-normal distribution.

Due to interaction with the surrounding air further break-ups of the secondary droplets can be observed leading to the second local maximum visible in the distribution at t_2. At this time larger droplets primarily reside on the surface while smaller droplets are mostly airborne.

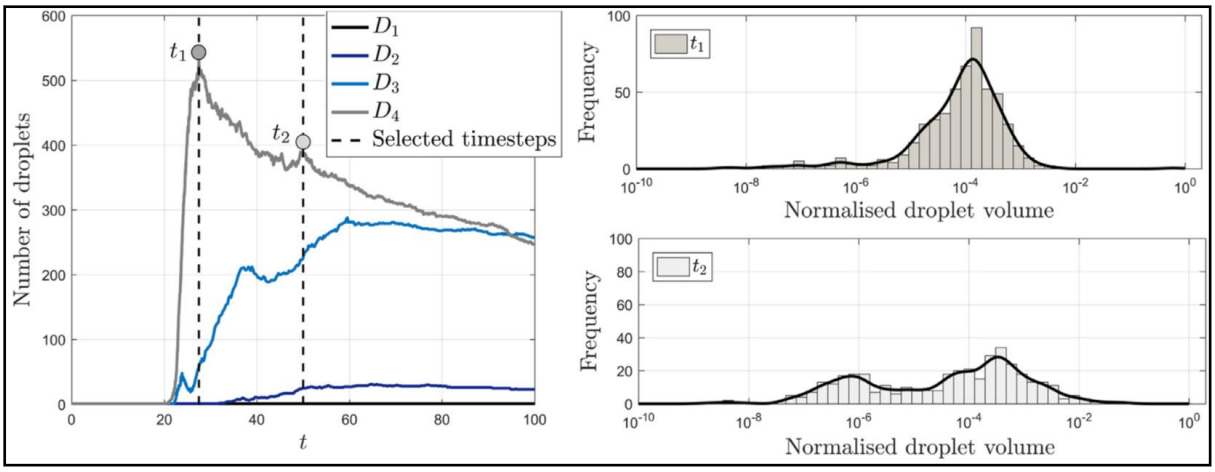

Figure 68 - On the left: Number of secondary droplets as a function of dimensionless time for different initial drop sizes (20 µm, 52 µm, 111 µm and 236 µm) resulting from an impact with an angle of incidence of 60°. On the right: Distribution of secondary droplet volumes normalized by the primary drop volume for an initial drop diameter of 236 µm for the two different times shown in the left panel. Taken from Cimpeanu and Papageorgiou [123]. (Permission to reprint required).

3.2.3.1.3 Conclusions

Although numerous studies on drop impacts and splashing have been performed in the past, secondary droplets originating from SLDs have not been investigated exhaustively. Previous studies can be classified into impacts on dry or wet surfaces. For both classes the splashing threshold, which determines whether secondary droplets are formed, has been studied thoroughly. However, still questions remain, regarding for example the influence of properties of the surrounding gas. Numerical studies have been performed both on the microscopic level by simulating single drops and on the macroscopic level of airfoils by incorporating models for single drop impacts. The characteristics of secondary droplets have gained attention due to the advances in modern high-speed cameras within the last decades. However, the studies mostly focus on temperatures above freezing and therefore might not be directly applicable to SLDs.

Following this literature review it can be concluded that further research on the splashing threshold and the characteristics of secondary droplets of SLDs is required. The existing investigations on drop impacts with temperatures above freezing have to be extended by possible effects due to supercooling. Furthermore, simple models have to be introduced and implemented in the numerical tools.

3.2.3.2 Partial deposit, sticking efficiency [ONERA, CIRA, TUDA, TUBS, POLIMI]

3.2.3.2.1 Objectives and issues

In order to estimate as precisely as possible the mass of accreted ice, its shape and the local heat transfer, an accurate estimation of the partial deposition is necessary. Such an estimate is introduced through an evaluation of the so-called sticking efficiency coefficient.

3.2.3.2.2 Literature review

3.2.3.2.2.1 PHYSICE2: revisited experiment for SLD impact. Sticking efficiency at small angle of incidence.

3.2.3.2.2.1.1 Description

The main objective of this experiment conducted in the framework of PHYSICE2 is the measurement of the droplet sticking efficiency at small (grazing) angles of incidence. The measurement system enables to study impacts at low angles of incidence with increased impact velocities up to 70 or 80 m/s (instead of 55 m/s previously in PHYSICE). A wide range of velocities, angles of incidence and diameters for the droplets has been proposed. The following ranges have been used:

- Air velocity from 40m/s to 80m/s;
- Angle of incidence from 10° to 90°;
- Droplet diameter from 200µm to 450µm.

Standard pressure conditions were respected. The temperature was set to ~20°C. Different coatings were studied: polished aluminium plate and blotter paper.

3.2.3.2.2.1.2 Main results, progress and limitations

Figure 69 presents the sticking efficiency ε as a function of the angle of incidence θ. The results obtained from the database of Papadakis [112] [124] [125] [126] have been superimposed with the ones obtained with PHYSICE2 by ONERA [127]. The main conclusions are the following ones:

- Two regimes can be defined. The first one for small angles of incidence (grazing impacts) where ε seems to be an increasing function of θ. The second regime appears at large angles of incidence (quasi-normal impacts), where a kind of plateau is observed for the sticking efficiency [126] [128] [129];
- The two regimes are observed whatever the database;
- However, the characteristics of each regime (slope of the function $\varepsilon(\theta)$ for small angles of incidence and limit value for the plateau) depend on the database and the substrate characteristics.

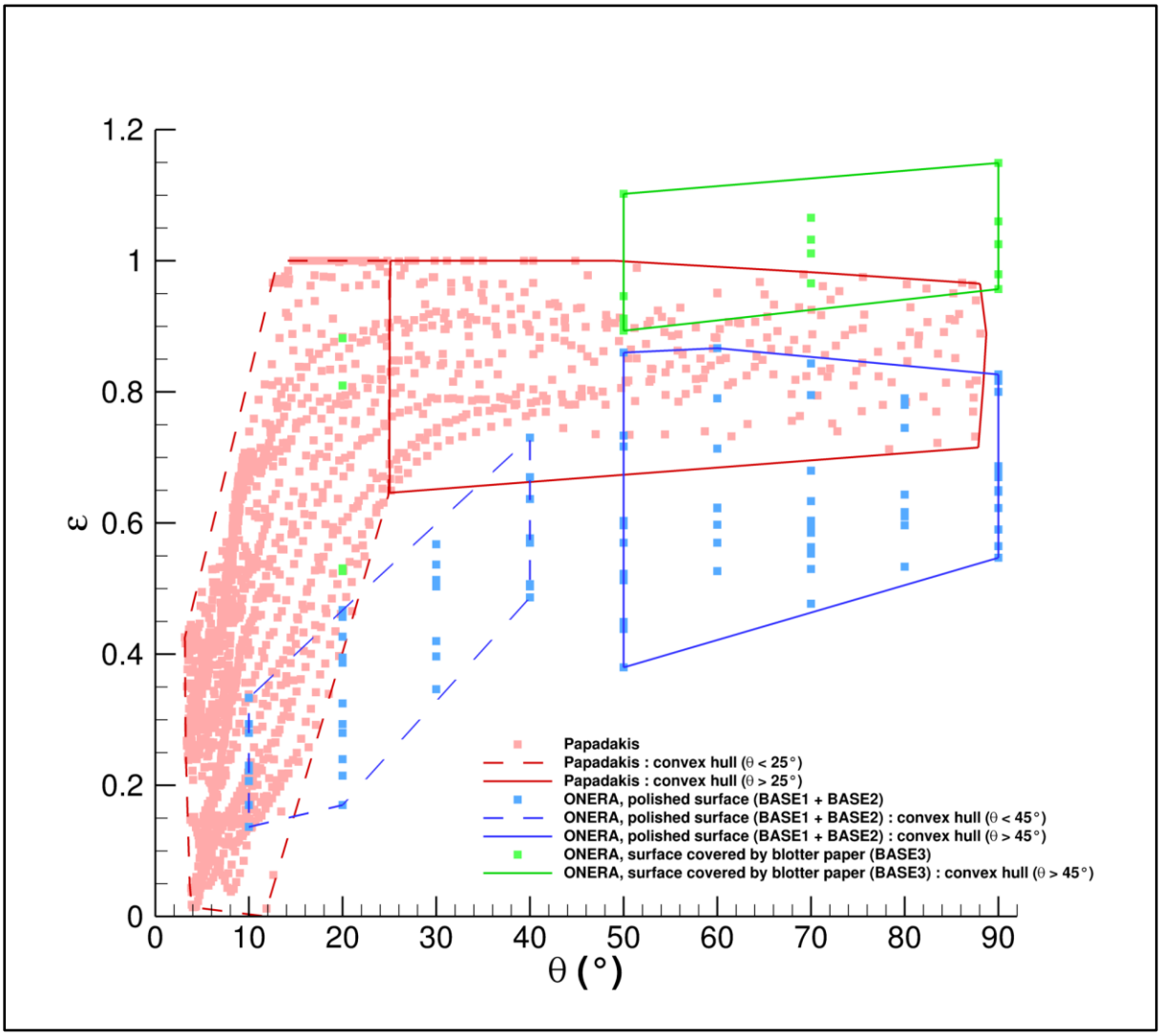

Figure 69 - sticking efficiency ε as a function of the angle of incidence θ. The results obtained from the database of Papadakis have been superimposed with the ones obtained by the ONERA within PHYSICE2.

3.2.3.2.2.2 SLD impact onto an ice surface: Ice layer thickness [130]

3.2.3.2.2.2.1 Description

In the scope of the German collaborative research project SFB-TRR 75, the interaction of phase change and fluid flow during the impact of supercooled water drops has been experimentally examined. Although this study did not directly aim onto sticking of the impinging drop, the study may be relevant for the prediction of sticking and resulting ice accretion.

Supercooled water drops have been investigated during normal impact onto an ice surface, which ensures immediate freezing of the drop after first contact with the impact surface, without any stochastic influence of nucleation. The final outcome of such an impact, i.e. the thickness of the residual ice layer resulting from freezing of the impinging drop has been studied for varying impact velocity and drop size. Based on the analytical description of the flow in the spreading drop and using experimental data for the solidification velocity of supercooled water, a semi-empirical model for the prediction of the residual ice layer thickness depending on the impact conditions has been developed.

3.2.3.2.2.2.2 Main results, progress and limitations

- The residual ice layer thickness decreases with increasing drop impact velocity and decreasing drop supercooling.
- The temperature of the impact surface does not affect the residual ice layer thickness, which primarily depends on the initial drop supercooling.
- For the examined range of impact velocities, growing dendrites do not break due to the shear flow in the spreading drop.
- The dimensionless impact condition $P = d_d^3 \eta \, v_f^5 / \nu^3 v_d^2$ has a unique influence on the dimensionless residual ice layer thickness (see Figure 70). Here d_d is the impact diameter, v_d is the impact velocity, v_f is the front velocity of the ice dendrite cloud, ν is the liquid kinematic viscosity and η is a dimensionless constant

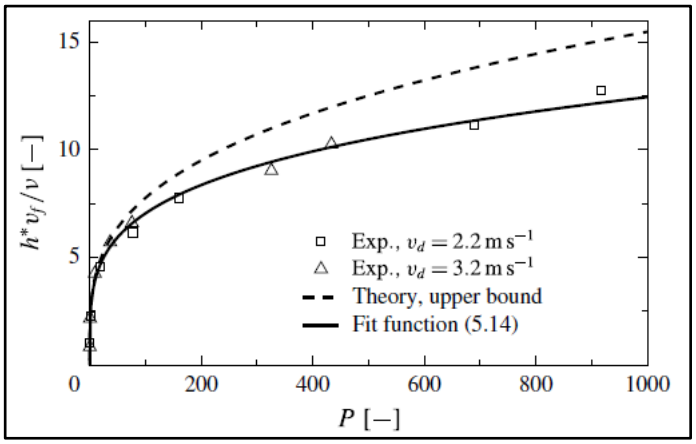

$$P \equiv \frac{d_d^3 \eta v_f^5}{\nu^3 v_d^2}$$

$$h^* v_{f,z}/\nu = 2.26 \left(\frac{d_d^3 \eta v_f^5}{\nu^3 v_d^2} \right)^{0.247}$$

Figure 70 - Dimensionless residual ice layer thickness depending on the dimensionless scaling of the impact conditions, P.

3.2.3.2.2.3 Shedding of water drops for different wettabilities under icing conditions [131] [132]

3.2.3.2.2.3.1 Description

An experimental investigation of a sessile drop exposed to an air flow has been conducted within the German research project SFB-TRR 75. The criterion for shedding is examined with a focus on icing conditions and wettability. The temperature range covers the interval from -8 °C up to -1 °C and wettabilities range from hydrophilic to superhydrophobic surfaces. Although no measurements on drop impingements were performed the study is relevant to determine if the drop sticks to the surface or is dislodged by the shear flow.

The test surface is placed in a temperature controlled wind tunnel and observed with a high-speed camera. Utilizing a micropipette a drop of the desired volume is placed in the test section. Starting the airflow and increasing the velocity gradually allows observing the drop shedding process. Drop volumes range from 5 to 100 µL, which is equivalent to a droplet of 2 to 6 millimeters.

3.2.3.2.2.3.2 Main results, progress and limitations

The critical air velocity required for the drop to shed is found to increase for decreasing temperature, i.e. drop shedding is hindered under icing conditions. The results are depicted in Figure 71. This is explained by a flattening of the drop going along with a decreasing temperature. The wettability of a surface is affected by low temperatures and causes the drop to flatten which decreases the drag coefficient of the drop and the adhesion force increases. However, the increase in critical air velocity

is different for different surfaces with different wettabilities. The model developed within the project is able to describe the critical velocity well.

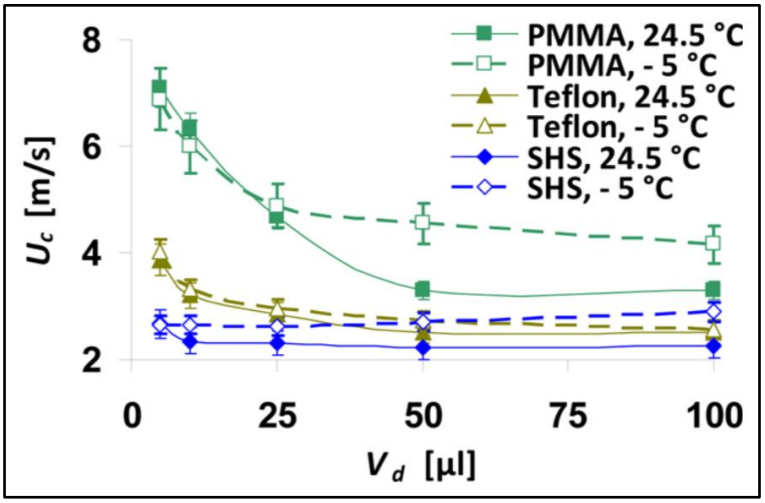

Figure 71 - Experimentally determined critical velocity required for drop to shed as a function of the drop volume for different wall materials and temperatures. Taken from Mandal et al. [132].

3.2.3.2.2.4 SLD impact on cold solid substrates: Sticking and partial deposition

3.2.3.2.2.4.1 Description

Within the German research project SFB-TRR 75, an experimental study has been performed to analyse the impact of single SLDs on a cold surface [133] [134]. The surfaces included superhydrophobic and partially wettable substrates. The drop impact, spreading and rebound were observed regarding to sticking and partial deposition of the drop. The SLD impact has been observed using a high-speed camera. The drop falls through a chilling passage cooled with liquid nitrogen. The temperature of the supercooled drop has been estimated to be between 0°C and -8°C. The substrate temperature ranged from 0°C to -20°C.

In another part of Li study [133], the high speed drop impact at room temperature has been analysed. Drop diameter ranged from 130 µm to 200 µm with a normal impact velocity from 10 m/s to 43 m/s. The drop impact outcome is observed by shadowgraph imaging. Furthermore, the mass-loss coefficient is measured using image post-processing. The mass-loss coefficient is defined as the ratio of the mass of the secondary droplets to the primary drop and is therefore directly related with the sticking efficiency.

3.2.3.2.2.4.2 Main results, progress and limitations

Figure 72 displays drop rebound of the impinging drop onto a superhydrophobic surface. The initial diameters of the drop were 1.6 mm and the impact velocities were almost 3.4 m/s. The images were taken when the diameter of the drop bottom reached its minimum. At lower substrate temperatures, the central part of the drop appeared to be frozen on the solid surface, and consequently prevented the total rebound. Furthermore, it is seen that the minimum diameter decreases for higher surface temperatures. This parameter is important since it correlates with the mass of ice deposited on the wall and thus indicates the sticking efficiency. The trend of the diameter with decreasing wall temperature is quantified and depicted in Figure 73.

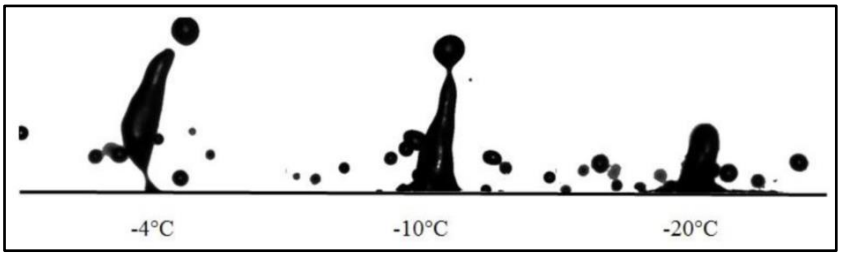

Figure 72 - Influence of the wall temperature on the rebound of water drops onto a superhydrophobic surface. Displayed are the minimum diameters at the end of the receding phase. Taken from Li et al. [134]

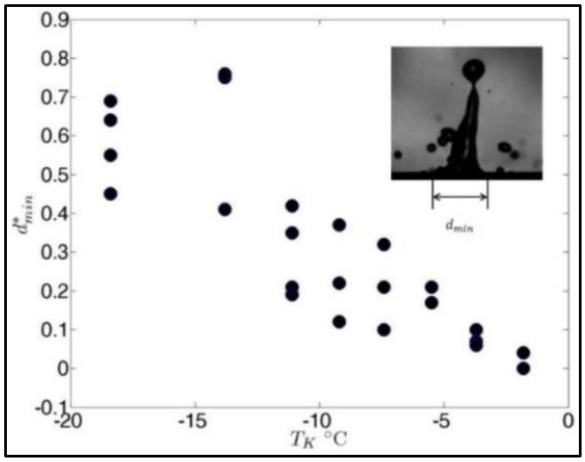

Figure 73 - Minimum receding diameter scaled by the maximum spreading diameter and its dependency on the contact temperature. Taken from Li et al. [134]

As seen in Figure 73, the frozen area increases with decreasing contact temperature indicating an increase in sticking efficiency, which results in a rising deposit mass of the impinging SLD onto the superhydrophobic surface. This suggests that superhydrophobic coatings cannot prevent freezing when the wall temperature is below 0 °C.

The measured mass-loss coefficients for the high speed drop impacts at room temperature are illustrated in Figure 74. Strong deformations of secondary droplets result in uncertainties in their mass and therefore cause large error bars for the mass-loss coefficient. Nevertheless, a clear trend in the collected data can be recognized. As expected, increasing K-number $K = We^{0.5}Re^{0.25}$ leads to an increase in mass-loss coefficient since splashing is promoted.

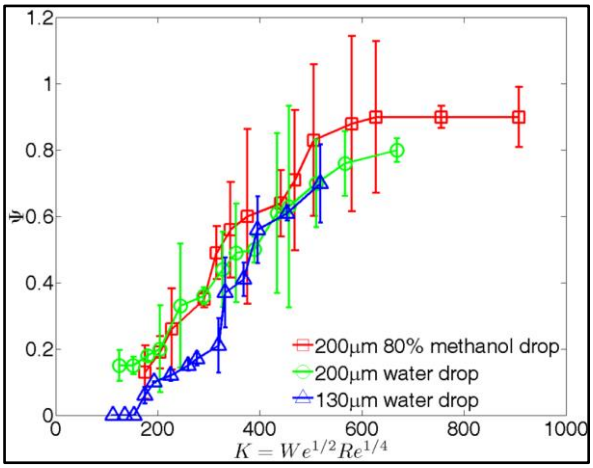

Figure 74 - Mass-loss coefficient as a function of the K-number for different drop sizes and fluids. Error bars are mainly due to large deformation of secondary droplets. Taken from Li [133].

3.2.3.2.2.5 Spray splashing mass ratio

3.2.3.2.2.5.1 Description

Roisman et al. [135] and Opfer [136] both investigated the impact of spray and analysed the secondary droplets. Roisman et al. obtained their data by performing PDA measurements whereas Opfer directly collected and characterised the deposited liquid. Although both studies investigate sprays, they can be related to single drops in the sparse spray regime.

3.2.3.2.2.5.2 Main results, progress and limitations

The results of both investigations have been collected and reviewed by Breitenbach et al. [137]. They are shown in Figure 75 for the spray splashing mass flux ratio as a function of the dimensionless number $\mathrm{K}_b = We^{4/5}Re^{2/5}$. The corresponding correlation represented by the dashed red line is given by

$$j_{ma}/j_{mb} = 0.5 - 0.616\exp\left[-\mathrm{K}_b\right].$$

Here j_m is the normal component of the mass flux density, where the index *a* corresponds to secondary droplets "*after*" the impact and the index *b* corresponds to primary droplets "*before*" the impact. As expected, with increasing K-number the fraction of the mass flux re-emitted as secondary droplets increases since splashing is promoted. Interestingly after a certain K_b number ($\mathrm{K}_b > 1500$) the mass flux ratio shows almost an asymptotic behaviour.

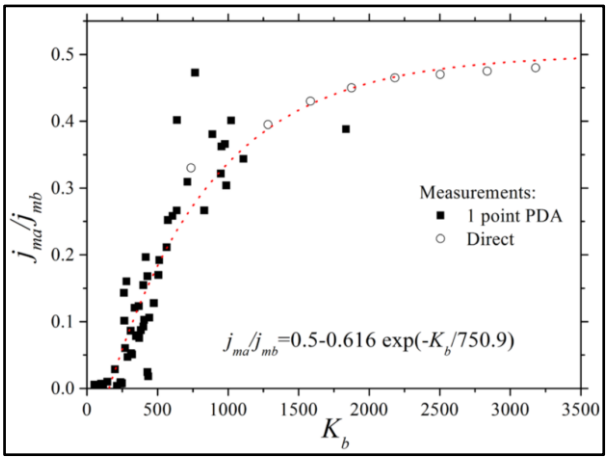

Figure 75 - The ratio of mass fluxes of secondary and primary sprays as a function of $K_b = We^{4/5}Re^{2/5}$. Taken from Breitenbach et al. [137] with data from Roisman et al. [135] and Opfer [136].

3.2.3.2.3 Conclusions

Studies were proposed to measure the sticking efficiency coefficient from different techniques: determination of the liquid water mass deposited on the wall or analysis of the complementary part made up of the re-emitted water droplets. Different substrates were investigated like cold solid substrates including superhydrophobic and partially wettable substrates. Superhydrophobic coatings were found to be unable to prevent freezing when the wall temperature is below 0 °C. A comparison between polished surfaces vs. surfaces covered by blotter paper was proposed showing that the blotter paper covering the walls greatly influences the sticking efficiency coefficient. This conclusion should be kept in mind since many current models for the sticking efficiency coefficient are based on the Papadakis databases which use blotter paper as a means of characterizing deposited liquid water. Both droplet trains and sprays were proposed as a means of injecting droplets. Universal trends are observed for several experiments: an increase of the sticking efficiency coefficient with the droplet diameter and velocity (more precisely with the K number), followed by a threshold. More fundamental studies were proposed as well. From the analytical description of the flow in the spreading droplet, a semi-empirical model for the prediction of the residual ice layer thickness was proposed. Moreover, shedding of sessile water droplets for different wettabilities was studied. Although no measurements on drop impingements were performed, this may help us better understanding the spreading phase of the droplet after impact.

3.2.3.3 Conclusions from EXTICE [CIRA]

Within EXTICE project [138], synergy between basic experiments, wind tunnel test, flight test and numerical simulation was realized in SLD conditions. EXTICE was an European funded project with the participation of CIRA, Alenia Aeronautica, ATR, DGA Aero-engine Testing (former CEPr), Cranfield University, Dassault, Technische Universität Darmstadt, INTA, ONERA, Piaggio, University of Naples, University of Twente, Airbus and Eurocopter. In the following, a summary of the main conclusions is presented with a particular focus on SLD experiments and simulations.

3.2.3.3.1 MODELING OF THE BASIC SLD PHYSICS

3.2.3.3.1.1 Main results

Basic experimental tests have been performed by ONERA/DGA Aero-engine Testing, University of Cranfield and TUDA to understand and eventually propose some modelling the physics of large droplet impact. The main outcome of this work package was the development of a mathematical model to describe the SLD droplet break-up, bouncing, splashing and droplet drag characteristics [133] [139] [140].

At first, main results from DGA Aero-engine Testing/ONERA basic tests can be summarized as follows:

- the size (mean diameter) of ejected drop remains constant equal to around 40 µm for normal impact;
- the size of ejected droplets increases with the impact angle;
- the velocity of drops after the impact is very low regarding incident velocity.

Secondly, three major areas of investigation have been undertaken by TUDA [133]: high speed droplet impact, single drop impact with solidification and spray impact in cross flow. Droplet spread consists in the deformation of the droplet shape during and after the impact with a solid wall or a liquid interface. Inertial, viscous, gravitational forces, interfacial tension and the contact angle of the solid–liquid–fluid system act to determine the evolution of the spreading phenomenon. The spread factor is defined as the diameter of the outer rim of the water (after impact) divided by the droplets equivalent spherical diameter. An example of some data is shown in Figure 76. The graphs show experimental data plotted in terms of droplet spread at a given time and time for a given droplet spread for droplet impact onto a target room temperature and at a sub-zero temperature vs. theoretical results.

The theoretical analysis which helps to formulate the drop collision model includes:

- Theoretical analysis of the rim instability. The model accounts for the inertia of the liquid in the rim and for the liquid flow entering the rim from the sheet, surface tension and viscous stresses. The governing equations are derived from the mass, momentum and moment-of-momentum-balance equations of the rim [141];
- Theoretical analysis of a single drop impact onto a dry substrate with solidification. It is based on the analysis of a fast forced non-axisymmetric spreading of a liquid film generated by inclined drop impact onto a solid flat substrate. A similarity solution for the combined full Navier–Stokes equations and energy equations is obtained which allows to predict the viscous flow and the temperature distribution in the film even if the thermophysical parameters of the liquid and solid materials depend on the temperature [142];
- Theoretical analysis and numerical simulations of single drop impact onto a liquid layer. The dynamics of the crater formed upon the impact of a single drop onto a liquid film was investigated using experimental measurements and numerical simulations. The dynamics of

drop impact on liquid surfaces is analyzed, focusing on the evolution of the crater formed beneath the surface upon the impact [143].

The theoretical analysis of drop impact and its splash leads to the assumption that the dimensionless diameter of the secondary drops, scaled by the diameter of the primary drops, has to be proportional to the $Re^{-1/2}$ if the aerodynamic effects are negligibly small. Here, the Reynolds number is based on the average diameter D30 and average velocity of the primary drops. This assumption is confirmed by the comparison with the experimental data from the ONERA/DGA Aero-engine Testing test campaign. The agreement between the predictions $D_{sec}/D_{prim} = 20\ Re^{-1/2}$ and the experiments is rather good (see Figure 76). The analogous result $D_{sec}/D_{prim} = 24\ Re^{-1/2}$ has been obtained for the low-velocity water spray (third item previously mentioned). Figure 77 clearly demonstrates that the effect of the air flow on the size of the secondary drops is very significant. Therefore, the relative air velocity has to be accounted for in the drop collision model relevant to the flight conditions.

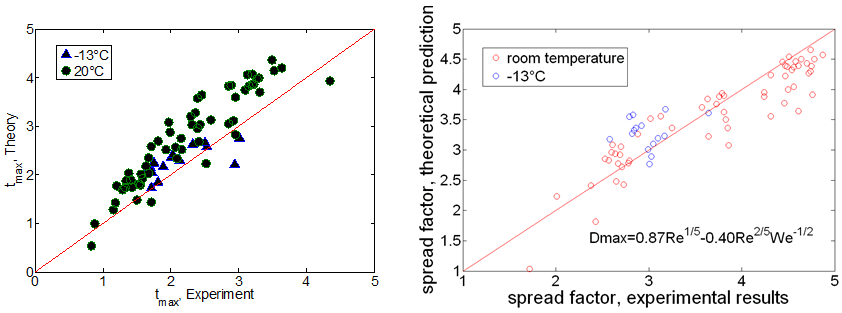

Figure 76 - Experimental droplet spread at room temperature and at a sub-zero temperature

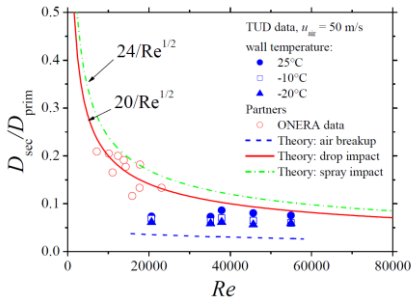

Figure 77 - Diameter of the secondary drops. ONERA and TUDA experiments - TUDA model

Finally, researchers from Cranfield University combined both the experimental and observation data with numerical modelling of the splashing process [139]. They built a conceptual framework to evaluate the effect of the water film thickness on the splashing features in SLD conditions. First of all, a series of images were captured by using a simple CCD camera and a single chip LED driven by a short high current pulse. By analyzing these images, important features of the splashing phenomenon can be measured, e.g. the corona angles, the speed and the distance at which the annular jet deflects and, finally, breaks up into free droplets. Main observations and conclusions are:

- droplet size is the most influential factor in determining the scale and velocity of the corona in the initial stages of its development;
- droplet impact onto thinner water films produces higher corona jet speed;
- impact angle strongly influences corona wall angle distribution.

The elements of greatest uncertainty in modeling SLD splash at the fine scale are the nature of the surface (of which the water film thickness plays a major role) and the breakup of the corona in the flow. The latter may be modelled numerically with a 2D Navier-Stokes Volume-Of-Fluid based flow

solver (VOF solver) which, according to Cranfield researchers, is quite accurate in predicting the general form and velocity of the corona wall which forms when a droplet strikes a film of water for the early stages of the splash In the later stages of the splash, the aerodynamic drag on the corona becomes significant, eventually resulting in the breakup of the corona into ligaments and droplets.

Hence, the nature of the surface and, in particular, the influence of the water film thickness are identified as the main source of uncertainty: as such, this topic has been further investigated at Cranfield. A series of experiments have been conducted to explore the impact of the water film thickness for the following conditions:

- Air velocity: 50 m/s to 80 m/s;
- Droplet size: 300 μm to 500 μm;
- LWC: 0.17 kg/m3 to 1.84 kg/m3;
- Impact angle: 45° and 70°.

The water film velocity has been measured as main output and a correlation function has been extracted with respect to the input parameters. By applying the lubrication theory, the water film velocity can be used to obtain an estimation of the water film thickness.

Besides, a series of numerical simulation have been performed using a 2D Navier-Stokes multiphase flow solver (VOF approach) to get data about corona angles and jet speed. Each simulation models the impact of a single droplet of given size, speed and direction onto a water layer of given thickness. Numerical correlations are then established for splashing mass loss coefficient, re-emitted angles and speed.

Finally, a general semi-empirical approach is proposed to combine the aforementioned data and models in an icing code and is summarized in the workflow of Figure 78. The box “Measurement and Theories” contains the water film experimental data and lubrication theory, which gives an estimation for water film thickness in output. The box “Splash parametric model”, instead, encloses the numerically-driven correlations obtained with the VOF model which takes the estimation of the water film thickness as input. The procedure can be then integrated within an icing solver to estimate the splashing mass loss as well as the re-emitted cloud characteristics for re-impingement simulation.

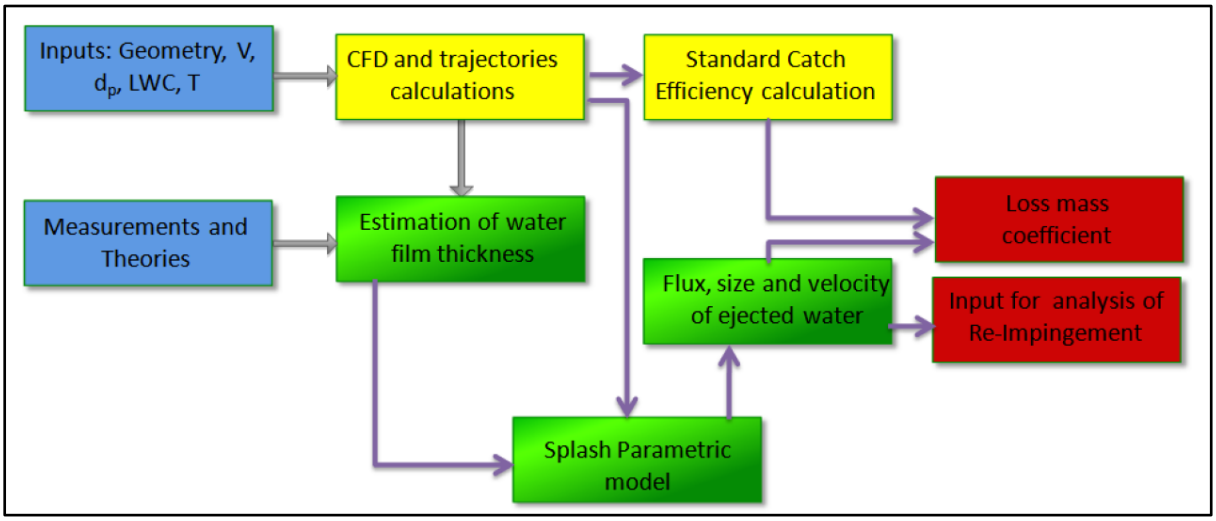

Figure 78: Cranfield numerical/experimental model for predicting splashing in SLD conditions

3.2.3.3.1.2 Lessons learned, limitations and perspectives

Although progress has been made on the modeling of the basic SLD physics during this project, additional work is still needed to understand the phenomena and extend the models. During the ICE-GENESIS project, we expect to characterize droplet impact at high velocity since the present data is restricted to small to moderate droplet velocity, to keep on characterizing the influence of the surface nature, the effect of the heated/unheated wall, …

3.2.3.3.2 SLD ICING TEST ON AIRCRAFT COMPONENTS

In CIRA icing wind tunnel, the model was the 3D full scale external section of the Dassault Falcon 7X wing provided by Dassault itself. Dassault modified the already available wind tunnel model used in past icing tests at IWT in 2005 to make it best fit to EXTICE objective.

The following conclusions can be drawn from performed tests:

- At medium and intermediate temperature, feathers and scallops have been accumulated;
- At very low temperature smooth ice shapes, no scallops but small feathers are present;
- At high incidence ice is accumulated also on lower flap surface.

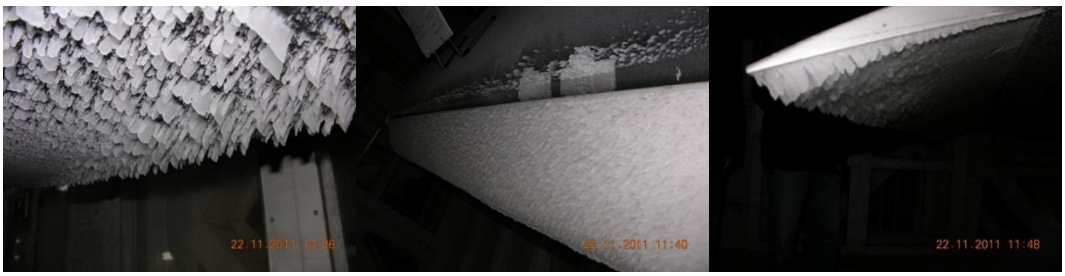

Figure 79 - Typical ice shapes in CIRA IWT wind tunnel

DGA Aero-engine Testing facility is the S1 icing altitude test facility (ATF). Previously designed for ramjet testing in simulated flight conditions, the S1 test bench has been modified to reach its current main configuration as an icing test bench. The test article used for EXTICE campaign is a steel made NACA 0012 airfoil of 800 mm chord and 700 mm span. This airfoil is equipped with 31 pressure taps for pressure distribution measurement. For all the test conditions, the three ice accretion shapes measured along the spanwise direction were very close. These results confirm the uniformity of the icing cloud for drop size distribution and LWC. Ice shapes data are important for CFD validation but the analysis of the aerodynamic loads (lift, drag) is also of interest to determine the critical shapes. During injection, lift decreases slightly. The maximum variation is about 10 %. Drag penalties increases between 70 and 200 % depending on test point conditions.

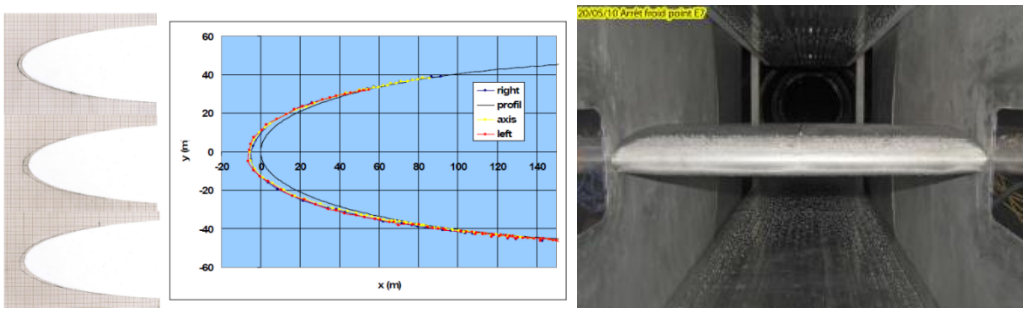

Figure 80 - Typical ice shapes in DGA S1 ATF wind tunnel

3.2.3.3.3 SLD SIMULATION IN ICE ACCRETION

3.2.3.3.3.1 Main results

Many partners had the availability of a numerical tool which could evaluate the ice accretion for conditions inside the envelope of Appendix C. The partner effort consisted in improving their existing software to deal with the SLD treatment with different strategies (water mass loss due to droplet re-emission, droplet drag, re-impingement …). Figure 81**Error! Reference source not found.** shows the impingement predictions on two public literature cases for SLD mass loss models validation: NACA 23012 and MS(1)-317 airfoils. For both cases, the theoretical vs experimental comparison has shown that new SLD developments are significantly effective in predicting realistic impingement levels. However, some discrepancies have been noticed, especially in terms of mass loss models behavior around the stagnation region.

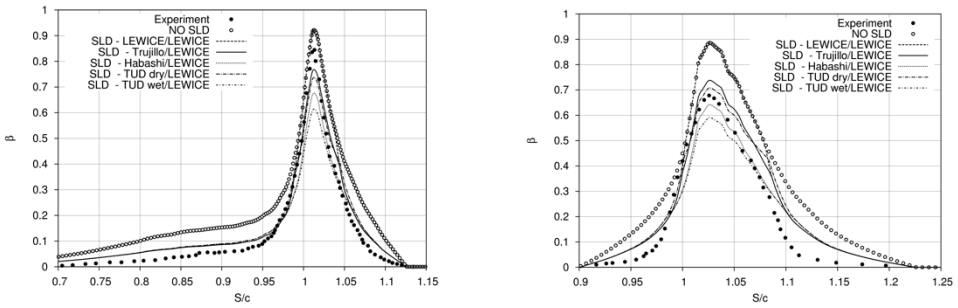

Figure 81 - SLD models verification within CIRA 2DICE code

Since DGA Aero-engine Testing 2D tests have been completed quite soon with respect to the EXTICE project start, each code developer/user (CIRA [138] [144], ONERA [145], UTW [146] [147], UNINA, Alenia Aeronautica, Piaggio, INTA) performed icing computations on the complete 2D test matrix. Both monomodal and bimodal droplet distributions have been considered to match the experimental conditions. Results show that the new modelling is effective in narrowing the gap between numerical and experimental data, but large discrepancies, especially at high MVDs, are still evident. At high Mach number (Figure 82), the comparison is highly improved by applying the SLD correction but important differences with the experimental data still exist. Figure 83 is an example of high temperature condition. In this case, significant improvements were obtained by applying the SLD correction but small horns are evident in the numerical simulation that do not appear in the experimental data. Figure 84 shows a case in which the SLD correction, at low speed and low temperature, is very effective.

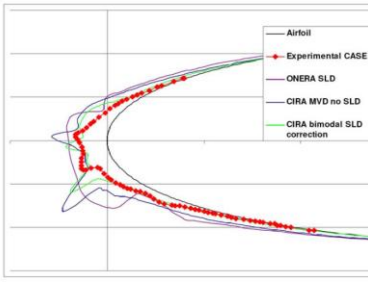

Figure 82 - Mach 0.65, 450 sec., LWC 0.3 g/m3, Temp. −25 °C, MVD 104 bimodal

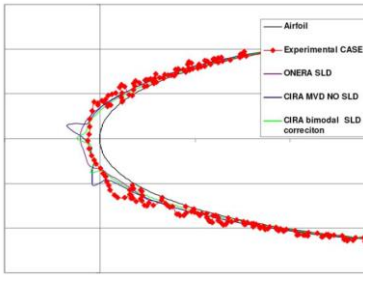

Figure 83 - Mach 0.2, 450 sec., LWC 0.4 g/m3, Temp. −10 °C, MVD 104 bimodal

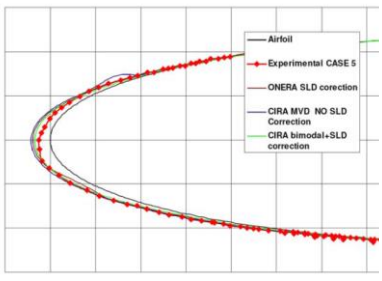

Figure 84 - Mach 0.2, 450 sec., LWC 0.3 g/m3, Temp. −25 °C, MVD 104 bimodal

Three-dimensional experimental data were produced closely to the project end, therefore only a selected number of test cases was identified for a detailed analysis and are presented below (Figure

85, Figure 86, Figure 87). In the three-dimensional cases 3, 6 and 8 (wing case, Figure 85), it has been observed that the numerical prediction generally overestimates the amount of deposited ice when the cloud droplet diameter is well within the SLD ranges and, as a consequence, the predicted mass loss levels seem insufficient. However, it must be underlined that some odd issues have been found when comparing the ice shapes from cases 6 and 8, as the ice thickness differ too much even if the two cases present very similar conditions. This might suggest an error in the wind tunnel LWC measurement, especially for case 8. For the three-dimensional case 19, there is a poor agreement in warm conditions (Ts=-5°C) whatever the slat position (Figure 86), highlighting some potential impact of the re-impingement phenomenon. Finally, some good agreement between experiments and computed shapes has also been obtained with extended or stowed slat configurations (case 20, Figure 87**Error! Reference source not found.**) in cold conditions (Ts= -25°C).

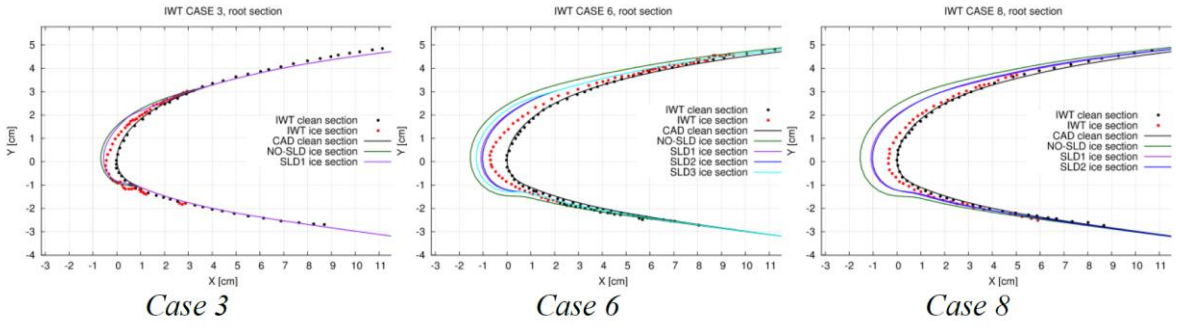

Figure 85 - CIRA 3D ice accretion simulations, clean wing configuration

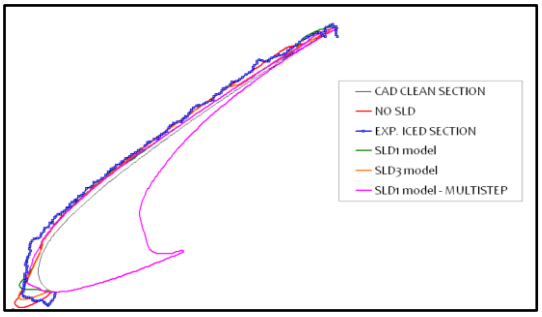

Figure 86 - CIRA 3D ice accretion simulations, wing + slat configuration, Case 19

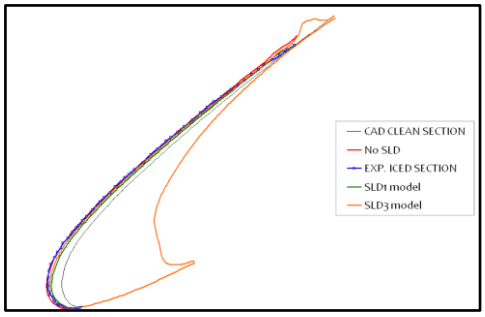

Figure 87 - CIRA 3D ice accretion simulations, wing + slat configuration, Case 20

3.2.3.3.3.2 Lessons learned, limitations and perspectives

The inclusion of SLD main physical features in the existing ice accretion model was addressed. Compared to models currently used for Appendix C, results show that the new modelling is effective in narrowing the gap between numerical and experimental data, but large discrepancies, especially at high MVDs, are still evident. A possible explanation is probably due to droplet splashing. At the end of this project, a first set of tools was made available to help aircraft manufacturers determining SLD impact on their products in order to comply with new regulations guidelines (Appendix O). Nevertheless, further work is still needed to improve the analysis tools and ground tests capabilities (icing wind tunnel quality and freezing rain domain).

More specifically, some following considerations have been resumed from numerical-experimental comparison:

- Mass loss formulation and splashing threshold are clearly identified as the primary factors in the splashing regime effects;
- Comparisons for splashing are not conclusive, current situation is that some models (NASA/Lewice) predict no splashing or little splashing at leading edge tending to zero when the impact is perpendicular to the wall, when others (Trujillo, Habashi, TUD) predicts a significant amount of splashing in the same conditions;
- NASA/Lewice bouncing model seems to perform quite well improving collection efficiency prediction in the impingements limits for all cases;
- More attention should be paid to the dependence of SLD models on empirical calibrations using databases. Indeed, the Lewice model has been calibrated on a NASA database but this model overestimates the mass loss near the leading edge with EXTICE data. On the other side, the Habashi model matches quite well with the EXTICE 3D database, but if it is used on the NASA database tests cases, it significantly underestimates the mass loss. In the future, in addition to the global need to refine the models, some efforts have to be put on a more "universal" SLD model by taking into account the whole available databases and establish a set of reference test cases which will be the core for a true general SLD model assessment;
- A comprehensive database for impingement analysis and code validation describing the whole App O remains necessary;
- The numerical/experimental comparison have also raised up the needs for better accuracy on tunnel parameters, like LWC or cloud uniformity, and deliveries of uncertainties attached to LWC measurements. Moreover, some doubts about true supercooling regime achievement for the larger drops have been identified in case of warm temperature (-5°C).

3.2.4 Ice density [POLIMI]

3.2.4.1 Description

Ice density data are of paramount importance to link the ice mass accreted on the surface, which depends on the water mass impinging on the aircraft, to the ice shape profiles. Unfortunately, scarce measurements are available and only simple, empirical models are presented in the open literature regarding ice density.

3.2.4.2 Main results, progress and limitations

The review presented by Rios in [148] identifies two models: the Macklin model [149] of 1961 and the Jones model [150] of 1988.

The Macklin model concerns rime ice accretion. The accreted ice density (in g.cm^{-3}) correlates to a parameter R, which is a function of a so-called effective mean volumetric droplet radius (approximately 50% of the MVD of the water droplets in the cloud), the droplet impact velocity Vr and the surface temperature Ts (in °C). Macklin model reads

$$\rho_i = 0.110\, R^{0.76} \qquad R \leq 17$$
$$\rho_i = 0.9 \qquad R > 17$$
$$R = -\frac{r_{EMVD}\, V_r}{T_s}$$

Foster and Bartlett identified the MVD as the parameter having the greatest effect on test uncertainty. Therefore, the EMVD should not be assumed to be the cloud MVD but should be calculated as a function of surface distance to minimize the uncertainty. The EMVD will be greater than the MVD, therefore, by employing MVD instead of EMVD higher densities would be predicted. The actual droplet impact velocity varies along with the flow around the surface of the aerodynamic body, from freestream velocity at the stagnation point to values greater than freestream velocity along the surface to the impingement limits. Thus, lower densities will be predicted near the accretion limits.

The Jones model [150] relies on measurable ambient variables including the MVD, the flow field velocity, the LWC, the ambient temperature and the Mean Cylinder Diameter. The latter refers to the measurement technique, which involves rotating cylinder. For airfoil, Jones suggests to use the airfoil chord or the leading edge radius times two as follows:

$$S = \frac{d_{MVD}^{0.82}\, V_\infty^{0.59}\, LWC^{0.21}}{D_{av}^{0.48}\left(-T_{air}^{0.23}\right)}$$
$$\ln \rho_i = -0.15\,(1 + 6043\, S^{-2.65})$$

In the previous relationships, the variables are expressed as: d_{MVD} in micrometers, V_∞ in meters per second, LWC in grams per cubic meter, D_{av} in centimeters and T_{air} in Celsius degrees. Jones model provides constant density given its macrophysical nature, but it can be improved by assigning a value to the mean cylinder diameter other than the chord length or twice the leading edge radius. For example it can be considered as the instantaneous radius of curvature for each accreting segment of the airfoil. This approach is used in order to take advantage of the fact that ice accretion is more dense along the leading edge (where the radius of curvature is small), than along the impingement limits (where the radius of curvature is greater), as probably already implemented in LEWICE.

The work of Fortin and Perron [151] on spinning rotor blades refers to the work of Laforte [152] for a rotating frame. The Laforte model delivers the following expression for the ice density:

$$\rho_i = 917 \left(\frac{MVD \sqrt{V_\infty + r^2\omega^2}}{MVD \sqrt{V_\infty + r^2\omega^2} + 2.6 * 10^{-6} \left[T_f - T_\infty \right]} \right)$$

where: ω = Blades angular velocity, r = radial distance from the rotor hub, T_f = freezing temperature. Recent measurements by Potapczuk [153] in the SLD regime include both ice shape and ice mass on a NACA0012 airfoil. Ice mass was found to decrease as a function of drop size, possibly due to splashing, though the ice shapes did not change. Therefore, the authors concluded that ice density decreases with increasing drop size. An empirical relation was given for the mass density as a function of the droplet diameter.

3.2.4.3 Conclusions

Available data for ice density are mainly available for rime ice, with the notable exception of the work by Potapczuk [153], which present an empirical relation for the ice density for the SLD regime. It is not easy to measure the ice density or to numerically simulate the ice accretion mechanism to compute it. Moreover, ice density is outside the scope of the ICE GENESIS project. Nevertheless, variable ice density should be considered in the numerical code to be devised in ICE GENESIS, at least at a qualitatively level, to perform sensitivity analysis when comparing to experiments.

3.3 Conclusions

This report presents the state of the art and the main conclusions of the works prior to the ICE GENESIS project. The addressed topics are the numerical methods for meshing, roughness, supercooled large droplets (SLD) and ice density. The main conclusions, gaps and future objectives to be achieved within the framework of ICE GENESIS are identified. This bibliographic review is a starting point for WP9 (Numerical capability development for liquid icing conditions) where the models and the dedicated numerical tools presented will be improved and validated with respect to Appendix C and O conditions. Taking into account the conclusions of the report dedicated to the requirements for the 3D numerical tools, the models and methods presented here will then be integrated and validated in industrial environment (WP11).

3.4 Bibliography

[1] E. Radenac, G. Linassier, C. Laurent, J. Pavlova and F. Petrosino, "STORM D4.8 - Public report on accretion and runback models for engine environment," STORM-FP7-605180, WP4, 2017.

[2] P. Trontin, A. Kontogiannis, G. Blanchard and P. Villedieu, "Description and assessment of the new ONERA 2D icing suite IGLOO2D," in *9th AIAA Atmospheric and Space Environments Conference, AIAA AVIATION Forum*, Denver, 2017.

[3] E. Berberović, M. Schremb, Ž. Tuković, S. Jakirlić and C. Tropea, "Computational modeling of freezing of supercooled water using phase-field front propagation with immersed points.," *International Journal of Multiphase Flow,* vol. 99, pp. 329-346, 2018.

[4] P. Rauschenberger, A. Criscione, K. Eisenschmidt, D. Kintea, S. Jakirlić, Ž. Tuković, I. Roisman, B. Weigand and C. Tropea, "Comparative assessment of Volume-of-Fluid and Level-Set methods by relevance to dendritic ice growth in supercooled water," *Computers & Fluids,* vol. 79, pp. 44-52, 2013.

[5] A. Criscione, D. Kintea, Ž. Tuković, S. Jakirlić, I. V. Roisman and C. Tropea, "Crystallization of supercooled water: A level-set-based modeling of the dendrite tip velocity.," *International Journal of Heat and Mass Transfer,* vol. 66, pp. 830-837, 2013.

[6] A. Criscione, I. V. Roisman, S. Jakirlić and C. Tropea, "Towards modelling of initial and final stages of supercooled water solidification.," *International Journal of Thermal Sciences,* vol. 92, pp. 150-161, 2015.

[7] J. Langer and H. Müller-Krumbhaar, "Stability effects in dendritic crystal growth.," *J. Crystal Growth,* vol. 42, 1977.

[8] F. Capizzano, "Turbulent wall model for immersed boundary methods," *AIAA Journal,* vol. 49, no. 11, pp. 2367-2381, 2011.

[9] F. Capizzano, "Coupling a Wall-Diffusion Model with an Immersed Boundary Technique," *AIAA Journal,* vol. 54, no. 2, pp. 2367-2381, 2016.

[10] F. Capizzano, "Automatic generation of locally refined Cartesian meshes: data management and algorithms," *International Journal of Numerical Methods in Engineering,* vol. 113, no. 5, pp. 789-813, 2018.

[11] E. A. Fadlun, R. Verzicco, P. Orlandi and Mohd-Yusof, "Combined Immersed-Boundary Finite-Difference Methods for Three-Dimensional Complex Flow Simulations," *Journal of Computational Physics,* vol. 161, pp. 35-60, 2000.

[12] Y. H. Tseng and J. H. Ferziger, "A Ghost-Cell Immersed Boundary Method for Flow in Complex Geometry," *Journal of Computational Physics,* vol. 192, pp. 593-623, 2003.

[13] J. Yang and E. Balaras, "An Embedded-Boundary Formulation for Large-Eddy Simulation of Turbulent Flows Interacting With Moving Boundaries," vol. 215, pp. 12-40, 2006.

[14] I. E. Capizzano F., "A Eulerian Method for Water Droplet Impingement by means of an Immersed Boundary Technique," *Journal of Fluids Engineering,* vol. 136, no. 4, pp. 1-8, 2014.

[15] L. Wutschitz and N. Nikiforakis, "A Cartesian Cut-Cell Approach for Modelling Air and Water Droplet Flow," in *AIAA SciTech, 54th AIAA Aerospace Sciences Meeting*, San Diego, California, USA., 2016.

[16] A.-K. A., P. D., H. Y., L. E. and M. R., "Multi-Step Level-Set Ice Accretion Simulation with the NSMB solver," in *23ème Congrès Français de Mécanique*, Lille, France, 2017.

[17] S. Osher and R. Fedkiw, "Level Set Methods and Dynamic Implicit Surfaces," *Science & Business Media,* vol. 153, 2006.

[18] H. Beaugendre, F. Morency, F. Gallizio and S. Laurens, "Computation of ice shedding trajectories using cartesian grids, penalization, and level sets," *Modelling and Simulation in Engineering,* 2011.

[19] D. Pena, Y. Hoarau and E. Laurendeau, "A single step ice accretion model using Level-Set method," *Journal of Fluids and Structures,* vol. 65, p. 278–294, 2016.

[20] P. Frolkovič, K. Mikula et J. Urbán, «Semi-implicit finite volume level set method for advection motion of interface in normal direction,» *Applied Numerical Mathematics,* 2014.

[21] P. Lavoie, G. Blanchard, E. Radenac, E. Laurendeau and P. Villedieu, "A Penalization Method for 2D Ice Accretion Simulations," in *proposed to SAE International Conference on Icing of Aircraft, Engines, and Structures*, Minneapolis, 2019.

[22] S. Peron, T. Renaud, I. Mary, C. Benoit and M. Terracol, "An Immersed Boundary Method for preliminary design aerodynamic studies of complex configurations," in *23rd AIAA Computational Fluid Dynamics Conference*, 2017.

[23] T. Renaud, C. Benoit, S. Peron, I. Mary et N. Alferez, «Validation of an immersed boundary method for compressible flows,» chez *AIAA SciTech Forum*, 2019.

[24] D. Sheppard, "A two-dimensional interpolation function for irregularly-spaced data," *Proceedings of the 1968 ACM National Conference,* 1968.

[25] P. George and H. Borouchaki, Delaunay Triangulation and Meshing, 1998.

[26] T. J. Baker, "Mesh deformation and modification for time dependent problems," *Int. Journal Numerical Methods for Fluids,* vol. 43, pp. 747-768, 2003.

[27] C. Dapong, C. Dobrzynski and P. Frey, "Three-dimensional adaptive domain remeshing, implicit domain meshing, and applications to free and moving boundary problems," *Journal of Computational Physics,* vol. 262, p. 358–378, 2014.

[28] B. Re, C. Dobrzynsky and A. Guardone, "An interpolation-free ALE scheme for unsteady inviscid flows computations with large boundary displacements over three-dimensional adaptive grids," *Journal of Computational Physics,* vol. 340, pp. 26-54, 2017.

[29] D. M. Kintea, «Hydrodynamics and Thermodynamics of Ice Particle Accretion,» *Phd Thesis, Technische Universität Darmstadt,* 2016.

[30] D. M. Kintea, J. Breitenbach, V. Thammanna Gurumuthi, I. V. Roisman et C. Tropea, «On the influence of surface tension during the impact of particles on a liquid-gaseous interface,» *Physics of Fluids,* vol. 28.1 012108., 2016.

[31] A. Bender, P. Hanichen, P. Stephan and T. Gambaryan-Roisman, "Modeling Crystallization and Heat Transfer in Evaporation Urea-Water Drop," 2016.

[32] S. Jakobsson et O. Amoignon, «Mesh deformation using radial basis functions for gradient-based aerodynamic shape optimization,» *Comput. Fluids,* 2007.

[33] A. de Boer, M. van der Shoot and H. Bijl, "Mesh deformation based on radial basis function interpolation," *Comput. Struct.,* 2007.

[34] C. Sheng and C. B. Allen, "Efficient Mesh Deformation Using Radial Basis Functions on Unstructured Meshes," *AIAA J.,* 2012.

[35] M. E. Biancolini, "Fast Radial Basis Functions for Engineering Applications," *Springer International Publishing,* 2017.

[36] T. C. S. Rendall and C. B. Allen, "Efficient mesh motion using radial basis functions with data reduction algorithms," *J. Comput. Phys.,* 2009.

[37] T. C. S. Rendall and C. B. Allen, "Reduced surface point selection options for efficient mesh deformation using radial basis functions," *J. Comput. Phys.,* 2010.

[38] T. Gillebaart, D. S. Blom, A. H. van Zuijlen and H. Bijl, "Adaptive radial basis function mesh deformation using data reduction," *J. Comput. Phys.,* 2016.

[39] M. E. Biancolini, I. M. Viola and M. Riotte, "Sails trim optimisation using CFD and RBF mesh morphing," *Comput. Fluids,* 2014.

[40] RBF4AERO Project, "'Innovative benchmark technology for aircraft engineering design and efficient design phase optimisation.," [Online]. Available: http://www.rbf4aero.eu/.

[41] E. Costa, C. Groth, M. E. Biancolini and G. Travostino, "RBF based mesh morphing approach to perform icing simulations in the aviation sector," in *4th EASN Association International Workshop on Flight Physics and Aircraft Design*, 2014.

[42] K. Hasanzadeh, "REYNOLDS-AVERAGED NAVIER-STOKES BASED ICE ACCRETION FOR AIRCRAFT WINGS," Ecole Polytechnique de Montreal, 2015.

[43] D. S. Thompson and B. K. Soni, "ICEG2D: A Software Package for Ice Accretion Prediction," in *AIAA Paper 2003-1070*, 2003.

[44] K. Hasanzadeh, E. Laurendeau and I. Paraschivoiu, "Grid-Generation Algorithms for Complex Glaze-Ice Shapes Reynolds-Averaged Navier–Stokes Simulations," *AIAA JOURNAL,* vol. 54, no. 3, 2016.

[45] K. Hasanzadeh, D. Pena, Y. Hoarau and E. Laurendeau, "Multi-time Step Icing Calculations Using a 3D Multi-block Structured Mesh Generation Procedure," in *SAE Technical Paper 2015-01-2161*, 2015.

[46] W. M. Chan and J. Steger, "Enhancements of a three-dimensional hyperbolic grid generation scheme," *Applied Mathematics and Computation,* vol. 51, no. 2, pp. 181-205, 1992.

[47] F. Vuillot, F. De La Puente, S. Landier, T. Renaud, C. Benoit and L. Sanders, ". "New Unstructured Grid Strategies for Applications to Aeroacoustic Computations of the LAGOON, Landing Gear Model, Using the CEDRE Unstructured Flow Solver," in *23rd AIAA/CEAS Aeroacoustics Conference*, Denver, 2017.

[48] M. Liou and K. Kao, "Progress in grid generation: from Chimera to DRAGON grids," NASA, 1994.

[49] S. Landier, «Boolean operations on arbitrary polygonal and polyhedral meshes,» *Computer-Aided Design,* vol. 85, pp. 138-153, 2017.

[50] F. Vuillot, S. Landier, T. Renaud, C. Benoit et L. Sanders, «Intersected Octree Conformal Grid Strategies for Applications to Aeroacoustic Computations of the LAGOON, Landing Gear Model, using the CEDRE Unstructured Flow Solver,» chez *25th AIAA/CEAS Aeroacoustic Conference*, Delft, the Netherlands, 2019.

[51] D. Rettenmaier, D. Deising, Y. Ouedraogoe, E. Gjonaje, H. De Gersem, D. Bothe, C. Tropea and H. Marschall, "Load Balanced 2D and 3D Adaptive Mesh Refinement in OpenFOAM," *Submitted to SoftwareX,* 2019.

[52] S. Hill, D. Deising, T. Acher, H. Klein, D. Bothe and H. Marschall, "Boundedness-preserving implicit correction of mesh-induced errors for VOF based heat and mass transfer," *Journal of Computational Physics,* vol. 2018, pp. 285-300, 2018.

[53] D. Deising, H. Marschall and D. Bothe, "A unified single-field model framework for Volume-Of-Fluid simulations of interfacial species transfer applied to bubbly flows," *Chemical EngineeringScience,* vol. 139, pp. 173-195, 2016.

[54] S. Batzdorf, "Heat transfer and evaporation during single drop impingement onto a superheated wall," Ph.D. Thesis, Technische Universität Darmstadt, 2015.

[55] A. Rothmayer and H. Hu, "A low-order model of the interaction between air-driven water films and sub-grid surface roughness," in *SAE Conference*, Prague, 2015.

[56] T. Hedde and D. Guffond, "ONERA three-dimensional icing model," *AIAA Journal,* p. 1038–1045, 1995.

[57] G. Ruff and B. Berkowitz, "User's manual for the NASA ice accretion prediction code (LEWICE)," NASA Contractor Report 185129, 1990.

[58] W. Olsen, R. Shaw and J. Newton, "Ice shapes and the resulting drag increase for a NACA 0012 airfoil," in *22nd AIAA Aerospace Sciences Meeting*, Reno, 1984.

[59] J. Shin and T. Bond, "Experimental and computational ice shapes and resulting drag increase for a NACA0012 airfoil," in *5th Symposium on Numerical and Physical Aspects of Aerodynamic Flows*, Long Beach, 1992.

[60] J. Shin, "Characteristics of surface roughness associated with leading edge ice accretion," in *32nd AIAA Aerospace Sciences Meeting and Exhibit*, Reno, 1994.

[61] W. Wright, "User's manual for LEWICE version 3.2," NASA Contractor Report 2008-214255, 2008.

[62] D. Anderson and J. Shin, "Characterization of ice roughness from simulated icing encounters.," in *35th AIAA Aerospace Sciences Meeting and Exhibit*, Reno, 1997.

[63] D. Anderson, D. Hentschel and G. Ruff, "Measurement and correlation of ice accretion roughness," in *36th AIAA Aerospace Sciences Meeting and Exhibit*, Reno, 1998.

[64] S. McClain, M. Vargas, J.-C. Tsao, A. Broeren and S. Lee, "Ice accretion roughness measurements and modeling," in *7th European Conference for Aeronautics and Space Sciences (EUCASS)*, Milan, 2017.

[65] R. Hansman Jr and S. Turnock, "Investigation of surface water behavior during glaze ice accretion," *Journal of Aircraft,* p. 140–147, 1989.

[66] Y. Han and J. Palacios, "Transient heat transfer measurements of surface roughness due to ice accretion," in *6th AIAA Atmospheric and Space Environments Conference - AVIATION 2014*, Atlanta, 2014.

[67] S. Bansmer and J. Steiner, "Ice roughness and its impact on the ice accretion process," in *8th AIAA Atmospheric and Space Environments Conference - AVIATION*, Washington DC, 2016.

[68] R. Hansman Jr, A. Reehorst and J. Sims, "Close-up analysis of aircraft ice accretion," in *30th AIAA Aerospace Sciences Meeting and Exhibit*, Reno, 1992.

[69] Y. Han and J. Palacios, "Surface roughness and heat transfer improved predictions for aircraft ice-accretion modeling," *AIAA Journal,* p. 1318–1331, 2017.

[70] S. McClain, M. Vargas and J.-C. Tsao, "Characterization of ice roughness variations in scaled glaze icing conditions," in *8th AIAA Atmospheric and Space Environments Conference - AVIATION*, Washington DC, 2016.

[71] S. McClain, M. Vargas et J.-C. Tsao, «Ice roughness and thickness evolution on a swept NACA0012 airfoil,» chez *9th AIAA Atmospheric and Space Environments Conference - AVIATION*, Denver, 2017.

[72] S. McClain, "Manual point cloud registration for combined ice roughness and ice thickness measurements," in *8th AIAA Atmospheric and Space Environments Conference - AVIATION*, Washington DC, 2016.

[73] EASA, "Acceptable means of compliance for large aeroplanes," CS-25, Amendment 18, 2016.

[74] H. Schlichting, Boundary layer Theory, McGraw Hill.

[75] D. Wilcox, Turbulence modeling for CFD, DCW Industries, 3rd edition, 2006.

[76] S. McClain and R. Kreeger, "Assessment of ice shape roughness using a self-organizing map approach," in *5th AIAA Atmospheric and Space Environments Conference*, 2013.

[77] S. McClain, M. Vargas and J. Tsao, "Ice roughness and thickness evolution on a swept NACA 0012 airfoil," in *9th AIAA Atmospheric and Space Environments Conference*, 2017.

[78] S. McClain, D. Reed, M. Vargas and e. al, "Ice roughness in short duration SLD icing events," in *6th AIAA Atmospheric and Space Environments Conference*, 2014.

[79] A. Braslow and R. Harris, "Use of grit-type boundary-layer transition trips on wind-tunnel models," NASA TN D-3579, 1966.

[80] M. Kerho et M. Bragg, «Airfoil boundary-layer development and transition with large leading-edge roughness,» *AIAA Journal,* vol. 35, n° %11, pp. 75-84, 1997.

[81] M. Bragg, M. Kerho and M. Cummings, "Effect of initial ice roughness on airfoil aerodynamics," in *32nd Aerospace Sciences Meeting and Exhibit*, Reno, 1994.

[82] J. Nikuradse, "Law of Flows in Rough Pipes," NASA-TM-1292, 1933.

[83] M. Raupach, R. Antonia et S. Rajagopalan, «Rough-Wall Turbulent Boundary Layers,» *Appl. Mech. Rev,* vol. 44, n° %11, pp. 1-25, 1991.

[84] J. Jiménez, «Turbulent flows over rough walls,» *Annual review of Fluid Mechanics,* vol. 36, pp. 173-196, 2004.

[85] M. Raupach, R. Antonia and S. Rajagopalan, "Rough-Wall Turbulent Boundary Layers," *Appl. Mech. Rev,* vol. 44, no. 1, pp. 1-25, 1991.

[86] L. Makkonen, "Heat transfer and icing of a rough cylinder," *Cold regions science and technology,* 1985.

[87] W. Kays et M. Crawford, Convective heat and mass transfer, McGraw-Hill, 1993.

[88] E. Radenac, A. Kontogiannis, C. Bayeux and P. Villedieu, "An extended rough-wall model for an integral boundary layer model intended for ice accretion calculations," in *Atmospheric and Space Environments Conference, AIAA AVIATION*, 2018.

[89] N. Dukhan, K. Masiulaniec, K. De Witt and G. van Fossen, "Experimental heat transfer coefficients from ice-roughened surfaces for air deicing design," *J. Aircraft,* vol. 36, no. 6, p. 948–956, 1999.

[90] B. Aupoix, "Roughness Corrections for the k-omega Shear Stress Transport Model : Status and Proposals," *Journal of Fluids Engineering,* vol. 137, 2015.

[91] B. Aupoix, "Improved heat transfer predictions on rough surfaces," *International Journal of Heat and Fluid Flows,* vol. 56, p. 160–171, 2015.

[92] F. Chedevergne, "Analytical wall function including roughness corrections," *International Journal of Heat and Fluid Flow,* 2018.

[93] T. Craft, A. Gerasimov, H. Iacovides and B. Launder, "Progress in the generalization of wall-function treatments," *Int. J. Heat Fluid Flows,* vol. 23, p. 148–160, 2002.

[94] K. Suga, T. Craft and H. Iacovides, "An analytical wall-function for turbulent flows and heat transfer over rough walls," *Int. J. Heat Fluid Flows,* vol. 27, no. 5, p. 852–866, 2006.

[95] R. D. Deegan, P. Brunet and J. Eggers, "Complexities of splashing," *Nonlinearity,* vol. 21, no. 1, pp. C1-C11, 2008.

[96] G. Liang and I. Mudawar, "Review of mass and momentum interactions during drop impact on a liquid film," *International Journal of Heat and Mass Transfer,* vol. 101, pp. 577-599, 2016.

[97] T. Okawa, T. Shiraishi and T. Mori, "Effect of impingement angle on the outcome of single water drop impact onto a plane water surface," *Experiments in Fluids,* vol. 44, no. 2, pp. 331-339, 2008.

[98] H. Kittel, I. V. Roisman et C. Tropea, «Splash of a drop impacting onto a solid substrate wetted by a thin film of another liquid,» *Physical Review Fluids,* vol. 3, n° %17, p. 073601, 2018.

[99] A. Yarin, "Drop Impact Dynamics: Splashing, Spreading, Receding, Bouncing...," *Annual Review of Fluid Mechanics,* vol. 38, 2006.

[100] C. Tang, M. Qin, X. Weng, X. Zhang, P. Zhang, J. Li and Z. Huang, "Dynamics of droplet impact on solid surface with different roughness," *International Journal of Multiphase Flow,* vol. 96, pp. 56-69, 2017.

[101] H. Li, Drop Impact on Dry Surfaces With Phase Change, Darmstadt: Technische Universität Darmstadt, 2013.

[102] I. V. Roisman, A. Lembach and C. Tropea, "Drop splashing induced by target roughness and porosity: The size plays no role," *Advances in Colloid and Interface Science,* vol. 222, pp. 615-621, 2015.

[103] H. Kittel, E. Alam, I. V. Roisman, C. Tropea et T. Gambaryan-Roisman, «Splashing of a Newtonian drop impacted onto a solid substrate coated by a thin soft layer,» *Colloids and Surfaces A: Physiocochemical and Engineering Aspects,* vol. 553, pp. 89-96, 2018.

[104] V. Bodoc, P. Berthoumieu, T. Xavier, D. Zuzio and P. Trontin, "Projet PHYSICE2. Rapport de synthèse final des travaux du lot 2. ONERA RT.," Toulouse, 2018.

[105] P. Berthoumieu and B. Déjean, "Experimental investigation of SLD impact phenomena," in *EUCASS*, Milan, 2017.

[106] A. L. N. Moreira, A. S. Moita and A. Panão, "Advances and challenges in explaining fuel spray impingement: How much of single droplet impact research is useful?," *Progress in Energy and Combustion Science,* vol. 36, pp. 554-580, 2010.

[107] M. Marengo, C. Antonini, I. V. Roisman and C. Tropea, "Drop collisions with simple and complex surfaces," *Current Opinion in Colloid & Interface Science,* vol. 16, pp. 292-302, 2011.

[108] L. Xu, W. W. Zhang and S. R. Nagel, "Drop Splashing on a Dry Smooth Surface," *Physical Review Letters,* vol. 94, p. 184505, 2005.

[109] R. Bilodeau, W. G. Habashi, M. Fossati and G. S. Baruzzi, "Eulerian Modeling of Supercooled Large Droplet Splashing and Bouncing," *Journal of Aircraft,* vol. 52, pp. 1611-1624, 2015.

[110] R. Bilodeau, W. G. Habashi, G. S. Baruzzi and M. Fossati, "An Eulerian Re-impingement Model of Splashing and Bouncing Supercooled Large Droplets," 2013.

[111] R. Honsek, W. G. Habashi and M. S. Aubé, "Eulerian Modeling of In-Flight Icing Due to Supercooled Large Droplets," *Journal of Aircraft,* vol. 45, pp. 1290-1296, 2008.

[112] M. Papadakis, K. Hung, G. Vu, H. Yeong, C. Bidwell, M. Breer and T. Bencic, "Experimental investigation of water droplet impingement on airfoils, finite wings and an S-duct engine inlet," 2002.

[113] E. Iuliano, "Modeling of Particle Impingement in Presence of Ice Crystals," *SAE Tech. Pap.,* vol. 2015, 2015.

[114] E. Iuliano, G. Mingione, F. Petrosino and F. Hervy, "Eulerian modeling of large droplet physics toward realistic aircraft icing simulation," *Journal of Aircraft,* vol. 48, pp. 1621-1632, 2011.

[115] T. Xavier, D. Zuzio, P. Trontin and J. Estivalezes, "Direct numerical simulation of drop impacts on a solid surface.," in *Euromech Colloquium 596*, San Servolo, Venice, Italia, 9-11/05/2018.

[116] A. Orazzo, I. Lagrange, D. Zuzio and J.-L. Estivalezes, "A VOF-based consistentmass-momentum transport for two-phase flow simulations.," in *ASME Fluids Engineering Division Summer Meeting*, Waikoloa, Hawaii, USA, 30/07-03/08/2017.

[117] Y. Guo, Y. Lian and M. Sussman, "Investigation of drop impact on dry and wet surfaces with consideration of surrounding air.," *Phys. of Fluids,* vol. 28, no. 7, p. 073303, 2016.

[118] G. Riboux et J. Gordillo, «The diameters and velocities of the droplets ejected after splashing,» *Journal of Fluid Mechanics,* vol. 772, pp. 630 - 648, 2015.

[119] G. Riboux and J. Gordillo, "Experiments of drops impacting a smooth solid surface: a model of a critical impact speed for drop splashing," *Physical Review Letters,* vol. 113, p. 024507, 2014.

[120] D. A. Burzynski and S. E. Bansmer, "Droplet splashing on thin moving films at high Weber numbers," *International Journal of Multiphase Flow,* vol. 101, pp. 202-211, 2018.

[121] D. A. Burzynski and S. E. Bansmer, "High Speed Visualization of Droplets Impacting with a Dry Surface at High Weber Numbers," *New Results in Numerical and Experimental Fluid Mechanics,* vol. XI, pp. 511-521, 2018.

[122] D. A. Burzynski and S. E. Bansmer, "The Role of Surrounding Gas in the Outcome of Droplet Splashing," *Physical Review Fluids,* vol. 'Under Review', 2018.

[123] R. Cimpeanu and D. Papageorgiou, "Three-dimensional high speed drop impact onto solid surfaces at arbitrary angles," *International Journal of Multiphase Flow,* vol. 107, pp. 192-207, 2018.

[124] M. Papadakis, A. Rachman and S. Wong, "Water droplet impingement on simulated glaze, mixed and rime ice accretion," 2007.

[125] M. Papadakis, S. Wong and A. Rachman, "Large and small droplet impingement data on airfoils and two simulated ice shapes," 2007.

[126] P. Trontin and P. Villedieu, "Revisited Model for Supercooled Large Droplet Impact," *Journal of Aircraft,* vol. 54, no. 3, pp. 1189-1204, 2017.

[127] V. Bodoc, P. Berthoumieu, T. Xavier, D. Zuzio et P. Trontin, «Projet PHYSICE2. Rapport de synthèse final des travaux du lot 2,» ONERA RT., Toulouse, 2018.

[128] P. Villedieu, P. Trontin, D. Guffond and D. Bobo, "SLD Lagrangian modeling and capability assessment in the frame of ONERA 3Dicing suite.," in *4th AIAA Atmospheric and Space Environments Conference*, New Orleans, Louisiana, USA, 25-28/06/2012.

[129] P. Trontin et P. Villedieu, «A revisited model for SLD impact onto a solid surface.,» chez *8th AIAA Atmospheric and Space Environments Conference, AIAA Aviation.*, Washington DC, USA, 13-17/06/2016.

[130] M. Schremb, I. V. Roisman and C. Tropea, "Normal impact of supercooled water drops onto a smooth ice surface: experiments and modelling.," *Journal of Fluid Mechanics,* vol. 835, pp. 1087-1107, 2018.

[131] I. Roisman, A. Criscione, C. Tropea, D. Mandal and A. Amirfazli, "Dislodging a sessile drop by a high-Reynolds-number shear flow at subfreezing temperatures," *Phys. Rev. E 92,* vol. 023007, 2015.

[132] D. Mandal, A. Criscione, C. Tropea and A. Amirfazli, "Shedding of Water Drops from a Surface under Icing Conditions.," *Langmuir,* vol. 31, no. 34, pp. 9340-9347, 2015.

[133] H. Li, «Drop impact on dry surfaces with phase changes,» PhD thesis, 2013.

[134] H. Li, I. Roisman and C. Tropea, "Impact of Supercooled Liquid Drops onto Cold Solid Substrates," in *SAE Technical Paper 2015-01-2101*, 2015.

[135] I. Roisman, K. Horvat and C. Tropea, "Spray impact: rim transverse instability initiating fingering and splash, and description of a secondary spray.," *Phys. Fluids,* vol. 18, pp. 102-104, 2006.

[136] L. Opfer, "Controlling Liquid Atomization using Dilute Emulsions: Mitigation of Pesticide Spray drift.," Ph.D. thesis. Technische Universität Darmstadt. Darmstadt, Germany., 2014.

[137] J. Breitenbach, I. Roisman and C. Tropea, "From drop impact physics to spray cooling models: a critical review.," *Experiments in Fluids,* vol. 59, no. 55, 2018.

[138] E. Iuliano, E. Mingione, F. Petrosino and F. Hervy, "Eulerian Modeling of Large Droplet Physics Toward Realistic Aircraft Icing Simulation," *Journal of Aircraft,* vol. 48, no. 5, pp. 1621-1632, 2011.

[139] J. Alzaili and D. Hammond, "Experimental Investigation of Thin Water Film Stability and Its Characteristics in SLD Icing Problem," in *SAE Technical papers*, 2011.

[140] A. Feo, M. Vargas and S. Sor, "Rotating rig development for droplet deformation/breakup and impact induced by aerodynamic surfaces.," in *SAE Technical paper series*, 2011.

[141] I. V. Roisman, «On the instability of a free viscous rim,» *J. Fluid Mech. ,* vol. 661, pp. 206-228, 2009.

[142] I. V. Roisman, «Fast forced film spreading on a substrate: flow, heat transfer and phase transition,» *J. Fluid Mech,* vol. 656, pp. 189-204, 2009.

[143] N. P. Van Hinsberg, M. Budakli, E. Berberović, I. V. Roisman, T. Gambaryan-Roisman, C. Tropea et P. Stephan, «Dynamics of the cavity and the surface film for impingements of single drops on liquid films of various thicknesses,» *J. Colloid Interface Sci.,* vol. 350, pp. 336-343, 2010.

[144] E. Iuliano, F. Mingione, F. Petrosino et F. Hervy, «Eulerian modeling of SLD physics towards more realistic aircraft icing simulation,» chez *AIAA Atmospheric and Space Environments Conference*, 2010.

[145] F. Dezitter, "ONICE2D and DROP3D SLD capability assessment.," in *SAE International Conference on Aircraft and Engine Icing and Ground Deicing*, Chicago, USA, 2011.

[146] J. Hospers and H. Hoeijmakers, "Numerical simulation of SLD ice accretions.," in *AIAA, 27th International Congree of the Aeronautical Sciences*, Reno, Nevada, USA, 2005.

[147] E. Norde, J. Hospers, E. van der Weide and H. Hoeijmakers, "Splashing model for impact of supercooled large droplets on a thin liquid film," in *52nd AIAA Aerospace Sciences Meeting*, National Harbor, Maryland, USA, 2014.

[148] M. Rios, "Icing Simulations using Jone's Density Formula for Accreted Ice," in *AIAA Paper 91-0556, 29th Aerospace Science Meeting*, Reno, 1991.

[149] W. C. Macklin, "The Density and Structure of Ice Formed by Accretion," *Quart. J. of the Royal Met. Soc.,* vol. 88, pp. 30-50, 1961.

[150] K. F. Jones, «The Density of Natural Ice Accretions,» chez *4th International Conference on Atomspheric Icing of Structures*, 1988.

[151] G. Fortin and J. Perron, "Spinning Rotor Blade Tests in Icing Wind Tunnel," in *AIAA Paper 2009-4260, 1st AIAA Atmospheric and Space Environments Conference*, San Antonio, 2009.

[152] J.-L. Laforte et M. Allaire, «Evaluation du Givromètre d'Hydro Québec à différentes intensités de givrage sec et humide,» Hydro-Québec, Etudes et Normalisation Equipement de Transport, Rapport HQ-92-02, Québec, 1992.

[153] M. G. Potapczuk, "Ice Mass Measurements: Implications for the Ice Accretion Process," in *AIAA Paper 2003-387*, 2003.

4 Numerical tools requirements

4.1 Introduction

This part focuses on requirements from industrial partners that have to be achieved at the end of the project. These requirements are provided in order to develop numerical tools capabilities which will allow the end-users (fixed or rotary wing manufacturers, engine manufacturers, suppliers …) to certify their products in the SLD domain as prescribed by CS-25 App O.

Table 1 sums up all the different requirements that have to be achieved, then each requirement is further detailed with subsequent attributes given the context, application, priority, physical modelling…

4.2 Requirements from aeronautical industries

4.2.1 Scope

This part describes the expectations in terms of requirements for numerical tools development and use in the framework of ICE-GENESIS. These requirements cover different fields of application like airframe manufacturers, engines application, aeronautical components suppliers and rotorcraft.

4.2.1.1 Definition of categories

In order to establish a set of requirements for numerical tools which would fulfil the expectations, each requirement is associated with some attributes. Those attributes are meant to provide some guidelines to experimenters and model developers to prioritize their work, to set experiments and to design numerical models that will be able to capture the accurate level of information and to reduce misunderstandings. These attributes are:

- Priority level
- Expected level of accuracy when relevant
- Elementary models that are thought to be involved
- Description of numerical features
- Computational performances
- Others
- Comments

For each of these attributes, further explanations follow. All of these attributes are grouped in tables included in the sub-paragraphs called in the sum up table 1

4.2.1.1.1 Scope of ICE GENESIS

It should not be necessary to use specific tools for super cooled droplets, SLD, mixed phase & glaciated icing conditions or snow. Therefore, the present document lists all the requirements of an ideal icing tool [1]; the developments mandatory for ICE GENESIS are underlined through a dedicated grey background column.

Hence, the tables should be read as follow:

- “Importance” is the importance of the criteria for a complete “ideal” icing tool
- “Development required in ICE GENESIS” states whether the criteria is applicable to ICE GENESIS or not

Note that the aim of ICE GENESIS is not to have one unified tool. Hence, some criteria listed here below may be developed on one tool but may not concern the others.

4.2.1.1.2 Priority Level

Depending on its importance, key functions have a priority level chosen among three possible levels defined as follows:

- **Essential**: Achieving this requirement is necessary (but it does not mean that the related function is in the scope of ICE-GENESIS)
- **Important**: Achieving this requirement will improve the performance and value of the end products
- **Desirable**: Achieving this capability may improve the speed/efficiency of the calculation and will improve the results
- **Nice to have**: Achieving this requirement could be useful but is not too much important for the calculations.

4.2.1.1.3 Expected Level of Accuracy

The specified level of accuracy refers to the “ideal code” and will not necessarily have to be achieved in ICE GENESIS, sometimes being greater than the uncertainty associated to benchmark experimental data.

4.2.1.1.4 Elementary Models

If applicable, this attribute will describe a list of elementary models to be applied in order to capture specific phenomena in the future 3D numerical tools, so that the associated requirement is achieved.

Since a requirement shall not specify the modelling strategy that will have to be adopted, this attribute is mainly indicative and the experimenters and modellers’ expertise is the essential key by which the requirement will be achieved

4.2.1.1.5 Numerical features

This attribute will describe the expected numerical features of the associated requirement.

4.2.1.1.6 Computational performances

This attribute will state the expected computational performance related to the associated requirement. It will be expressed in terms of CPU time on a certain amount of cores.

4.2.1.1.7 Other comments

This attribute will contain any additional comment related to the associated requirement.

4.2.1.2 Top Level User Requirements

The numerical tools delivered in ICE-GENESIS (called the software in the following) should address the requirements listed in table 1:

Req.	Statement	See paragraph
1	The software shall encompass arbitrary 2D objects	§4.1.2.1
2	The software shall encompass arbitrary 3D objects	§4.1.2.2
3	The software shall be compliant with FAR-25/CS-25 Appendix O conditions (SLD) as well as Appendix C conditions (incl. FAR/CS 29)	§4.1.2.3
4	The software shall compute liquid droplets trajectories	§4.1.2.3
5	The software shall compute droplet temperature equilibrium along its trajectory	§4.1.2.3
6	The software shall compute the droplet particle size distribution at a given location in the flow	§4.1.2.3
7	The software shall take into account droplet/wall interactions	§4.1.2.3
8	The software shall be able to handle Lagrangian and/or Eulerian approach	§4.1.2.3
9	The software shall be able to compute heat transfer coefficient on iced surfaces (smooth and rough)	§4.1.2.4
10	The software shall compute liquid mass transfer between the impacted wall, the impacting droplets and/or the water/ice layer	§4.1.2.5
11	The software shall compute ice accretion prediction on unheated surfaces	§4.1.2.5
12	The software shall estimate ice layer roughness	§4.1.2.5
13	The software shall estimate accreted ice density	§4.1.2.5
14	The software shall compute thermal balance in presence of an activated ice protection system (heated wall)	§4.1.2.6
15	The software shall handle steady state behaviour	§4.1.2.5 §4.1.2.6
16	The software shall handle the time evolution of the ice shape.	§4.1.2.5 §4.1.2.7
17	The software shall be compatible and comply with industrial simulation environment and platforms	§4.1.2.8
18	The software shall be delivered with a documented user guide, a theoretical manual, a non-regression/validation database and associated Best Practices	§4.1.2.8
19	The software shall be structured with independent modules that could be interfaced with external modules	§4.1.2.8
20	The software shall be able to handle unstructured meshes and/or structured meshes (tetrahedral, prisms, hexahedra, pyramids)	§4.1.2.8

Table 1: Synthesis of the requirements

4.2.1.2.1 2D configurations

- Req #1 : The software should encompass arbitrary 2D objects

4.2.1.2.1.1 Attributes description

As there is a huge background on ice shapes computations with 2D tools, the software developed in ICE-GENESIS shall be able to deal with the following 2D configurations:

- 2D single element aerofoils
- 2D multi-element aerofoils
- 2D axi-symmetric nacelles
- 2D compressor blades or struts
- 2D axi-symmetric splitter nose
- Arbitrary 2D non-lifting shapes

See also 4.1.2.2.2 for performances and user interface

4.2.1.2.2 3D configurations

- Req #2: The software should encompass arbitrary 3D objects.

4.2.1.2.2.1 Attributes description

The software developed in ICE-GENESIS shall be able to deal with the following 3D configurations:

- Swept, tapered, twisted wings, e.g. wing, winglet, HTP and VTP
- Wings with deployed high lift systems
- Any other 3D aerodynamic surfaces, typical of those used on aircraft
- Non-lifting objects: e.g. fuselage, fairings, protuberances, instruments (such as pitot tubes)
- Components with internal mass flow: e.g. NACA ducts, pitot intakes, nacelles, flush intakes, scoops etc.
- Rotating components: e.g propellers, RAT, engine fan blades, compressor blades, with one or several stages rotating at different velocities, rotors, Fenestron (shrouded rotor).
- Any other engine components exposed to the flow: e.g. splitter nose, probes etc.
- For turbomachinery applications, the software shall be able to handle typical constraints as:
- Periodicities
- Rotating boundaries
- Relative movement of boundaries
- Multi-domain (e.g. mixing plane)

4.2.1.2.2.1.1 Others

Tool design characteristic/capability		Development required for ICE-GENESIS	Importance				Notes
			Essential	Important	Desirable	Nice to have	
	Easy data pre-processing			X			e.g. GUI
Efficiency and user-interface	Automatic positioning of droplets for the trajectory analysis.			X			
	Automatic monitoring of potential errors and inaccuracies.			X			Produces warnings/errors when sufficient accuracy is not obtained.
	Automatic control of potential errors and inaccuracies.			X			Automatically adjusts trajectory analysis to obtain desired accuracy.
	Fully automatic calculations of water catch on a specified surface.			X			No user interaction or checking required.
	Automatic positioning of droplets re-emission injection points			X			
Performances 2D	CPU (running time) < 30 minutes	X	X				These characteristics are to reflect the need to have a tool that is reasonably practicable to use. They refer to 'standard' test cases, in steady state
	CPU time < 10 minutes	X		X			
	CPU time < 5 minutes	X			X		

Tool design characteristic/capability		Development required for ICE-GENESIS	Importance				Notes
			Essential	Important	Desirable	Nice to have	
	CPU time < 1 minutes	X				X	conditions, among the configurations cited in 4.2.1.2.1.1 and on a standard office computer (local 4cores, 64 bits, 16Gb Memory).
Performances 3D	CPU time < 1 day (24 hours)		X				These characteristics are to reflect the need to have a tool that is reasonably practicable to use. They refer to 'standard' test cases, in steady state conditions, among the configurations cited in 4.2.1.2.1.1 and on a standard office computer (local 4 cores , 64 bits, 16Gb Memory).
	CPU time < 6 hours	X		X			
	CPU time < 30 minutes				X		
	CPU time < 10 minutes					X	
Inter-operability	Common format file for each input and output files of the tools shall be defined	X	X				At least be able to read/convert flow fields from and to CGNS format.
Accuracy	Skin Temperature for accretion tools +/- 2°C	X	X				
	Skin Temperature for Anti-icing tools +/- 5°C	X	X				
	Local concentration +/- 2%	X	X				Collection efficiency as well as LWC (α parameter)
	Ice thickness +/-10%	X	X				Target at least 20%
	Ice mass +/- 10%	X	X				
	Ice shape definition +/- 10%	X	X				Ice shape features: horn angle, ice chordwise extension…
Robustness	User inputs checks, error tracking and Mesh control	X		X			This requirement applies to all developments done in ICE-GENESIS

Nota: some key functions in the table above (performance, accuracy, robustness) which will be improved during the project are not necessarily new features developed during the project. Nevertheless, any development done in the project which could impact them should take into account these needs to avoid any regression. Furthermore, any improvement is welcomed

4.2.1.2.3 Droplets trajectories and impingement

- Req #3: The software shall be compliant with FAR25/CS-25 Appendix O conditions (SLD) and Appendix C conditions for FAR25/CS-25 and FAR29/CS-29
- Req #4: The software shall compute liquid droplets trajectories
- Req #5: The software shall compute droplet temperature equilibrium along its trajectory
- Req #6: The software shall compute the droplet particle size distribution at a given location in the flow
- Req #7: The software shall take into account droplet/wall interactions
- Req #8: The software shall be able to handle Lagrangian and/or Eulerian approach

4.2.1.2.3.1 Attributes description

Tool design characteristic/capability		Development required for ICE-GENESIS	Importance				Notes
			Essential	Important	Desirable	Nice to have	
Icing environment	App. C	X	X				
	App.O Freezing Drizzle	X	X				
	App. O Freezing Rain	X		X			Lack of experimental validation data in ICE-GENESIS
Frameworks	Both Eulerian and Lagrangian	X	X				
Models	Consider Coriolis and centrifugal forces for a rotating frame of reference for steady-state calculations.		X				Not in the scope of ICE-GENESIS
	Droplet/particle trajectory periodicity in rotation or translation for steady-state calculations		X				
	Mixing planes for steady state droplets and particles trajectory analysis of different, serial rotating frames		X				
	Able to model crossing of droplet trajectories.	X		X			Available with Lagrangian approach
Pre/post processing	Able to model spectrum of droplet sizes: Manual interaction required.	X	X				
	Able to model spectrum of droplet sizes: Fully automatic.	X	X				
	Manual Ability to determine the local concentrations, or 'α' parameter on planes that are not surfaces.	X	X				Need for post-processing on basic surface/volume (e.g. annular spheres (desirable)
	Able to model droplet trajectories passing through an actuator disc	X	X				SLD development should be compatible with an actuator disk model

Pre/post processing (cont.)	Manual Ability to determine local water catch efficiency along a surface for a given type of particles (diameter, phase…)		X				Not in the scope of ICE-GENESIS
Physical model for small droplet motion and impingement	Consider aerodynamics forces on the droplet motion		X				Not in the scope of ICE-GENESIS
	Droplets start at local air velocity		X				
Physical model for large droplet motion and impingement	Consider gravitational forces on the droplet motion	X	X				Not in the scope of ICE-GENESIS
	Increment applied to initial droplet velocity to account for the droplet terminal velocity	X	X				Not specific to ICE-GENESIS
	Able to model droplet deformation due to high relative velocities.		X				Investigated via a Boeing collaboration. No need to be addressed in ICE GENESIS.
	Able to model droplet break-up due to high relative velocities.	X	X				See above
	Able to model droplet bounce from impact on the surface (increment to catch only, assuming no re-impingement).	X	X				
	Able to model droplet splashing from impact on the surface (increment to catch only, assuming no re-impingement).	X	X				
	Able to model secondary trajectories and subsequent re-impingement of rebounded or splashed droplets.	X		X			
	Able to compute the droplet change temperature along its trajectory	X		X			Issue with thermal equilibrium for the large droplets in icing wind tunnel. Super cooled state for large droplets is challenging in some IWT.
	Able to take into account wall surface features for large droplet wall impact (roughness, presence of liquid film, temperature for Ice Protection System application…)	X	X				
	Able to take into account local air flow for large droplet wall impact (crossflow, …)	X	X				

4.2.1.2.4 Heat Exchange

- Req #9: The software shall be able to compute heat transfer coefficient on iced surfaces (smooth and rough)

4.2.1.2.4.1 Attributes description

Tool design characteristic/capability		Development required for ICE-GENESIS	Importance				Notes
			Essential	Important	Desirable	Nice to have	
Surface type compatibility	Calculation of accurate HTCs on iced (rough) surfaces.	X	X				ICE GENESIS will provide new semi-empirical models for the prediction of roughness parameters depending on icing conditions.
	Calculation of accurate HTCs on smooth surfaces, or ability to read in HTCs from CFD.		X				For anti-icing purposes. HTCs could be obtained either by setting wall roughness height very low or using a specific method for smooth surfaces is desirable. Not addressed in ICE-GENESIS
	Calculation of HTCs on surfaces with a mixture of iced and smooth regions.		X				This requirement is to be able to accurately model HTCs on mixed smooth and rough surfaces, not necessarily used different methods for each type of surface (i.e. the results, not the methodology). Not addressed in ICE-GENESIS
	Calculation of accurate HTCs on heated wall (heat transport through boundary layer...)		X				Useful for thermal ice protection systems Not in the scope of ICE-GENESIS
Physical model for External heat transfer coefficient (HTC) calculation	Able to compute natural laminar-turbulent transition over smooth surface (unheated wall)		X				Not specific to ICE-GENESIS
	Able to compute natural laminar-turbulent transition over smooth surface (heated wall)				X		Useful for thermal ice protection systems but not addressed in ICE-GENESIS
	Able to compute laminar-turbulent transition over rough surface		X				Including modelling of transition region Not addressed in ICE-GENESIS.

4.2.1.2.6 Water flow and ice accretion modelling

- Req #10: The software shall compute liquid mass transfer between the impacted wall, the impacting droplets and/or the water/ice layer
- Req #11: The software shall compute ice accretion prediction on unheated surfaces
- Req #12: The software should estimate ice layer roughness
- Req #13: The software should estimate accreted ice density
- Req #15: The software shall handle steady state behaviour
- Req #16: The software shall handle the time evolution of the ice shape

4.2.1.2.6.1 Attributes description

In the framework of ICE GENESIS, runback water models and droplet re-emission models will not be developed (previously addressed by other research projects like STORM).

Tool design characteristic/capability		Development required for ICE-GENESIS	Importance				Notes
			Essential	Important	Desirable	Nice to have	
Liquid mass deposit	Able to predict liquid mass transfer between impacting droplets and iced/water layer	X	X				
Runback water flow modelling	Model water flow in terms of surface mass flow rates.		X				Minimum requirement: Current method used within 2D codes. Not specific to ICE-GENESIS
	Calculation of water film height.	X		X			Not specific to ICE-GENESIS Could be essential for droplet wall impact
	Calculation of water film height, taking into account roughness features caused by ice accretion.				X		
	Calculation of water film break-up into rivulets: Semi-empirical.		X				This function is needed for any anti-icing ice protection system. Not specific to ICE-GENESIS
	Calculation of water film break-up into rivulets: Fully theoretical.					X	
	Calculation of water film re-emission: geometric rupture		X				Not specific to ICE-GENESIS
	Calculation of water film re-emission: aerodynamic peeling			X			
Transportation of runback water	Air shear (skin friction)		X				Not specific to ICE-GENESIS

Tool design characteristic/capability		Development required for ICE-GENESIS	Importance				Notes
			Essential	Important	Desirable	Nice to have	
Transportation of runback water calculated with allowances for: (cont.)	Solid surface friction			X			Roughness influence, static/dynamic contact angle (hydrophobic or hydrophilic surfaces) Not addressed in ICE-GENESIS
	Pressure forces			X			
	Gravitational forces				X		
	Centrifugal forces		X				Only applicable if the tool has a rotational capability. Not specific to ICE-GENESIS
	Coriolis forces		X				Only applicable if the tool has a rotational capability. See above
	Mass loss due to evaporation and sublimation.		X				Essential when analysing anti-icing at ambient temperature above freezing. Sublimation necessary for ice loss aft of protection (from pre-existing runback ice) See above
Ice growth modelling, taking into account the following heat sources:	Kinetic heating/convection		X				Basic functions not specific to ICE-GENESIS and already available in numerous icing tools
	Cooling due to evaporation		X				
	Cooling due to sublimation			X			
	Correction to evaporation/ sublimation heat loss due to relative humidity <100%		X				Essential for engine core but not specific to ICE-GENESIS
	Allowances in evaporation/ sublimation heat loss due to partially wetted surface				X		See above
	Latent heat of freezing		X				
	Sensible heat due impinging droplets		X				
	Sensible heat from runback water		X				
	Heat from kinetic energy of the droplets		X				

Tool design characteristic/capability		Development required for ICE-GENESIS	Importance				Notes
			Essential	Important	Desirable	Nice to have	
Ice growth modelling, taking account of the following heat sources: (cont.)	Heat flow due to conduction		X		X		Essential for modelling thermal ice protection systems (addressed later), desirable for modelling substrates with a large thermal mass. Not specific to ICE-GENESIS
	Steady state conduction, from the control volume into the substrate and within the substrate.			X			No consideration of the thermal mass. Lateral conduction through the substrate affects neighbouring ice growth rates. Already developed in 2D code of ONERA.
	Transient conduction, through the ice and within the substrate.					X	Complete analysis of the conduction characteristics.
	Automatic adjustment of spatial discretisation of the mesh used for the ice growth model to control errors.			X			Not addressed in ICE-GENESIS

4.2.1.2.7 Heated surfaces in steady state behaviour

- Req #14: The software should compute thermal balance in presence of an activated ice protection system (heated wall)
- Req #15: The software shall handle steady state behaviour

4.2.1.2.7.1 Attributes description

In the framework of ICE GENESIS, dedicated anti-icing models will not be developed. Validation of tests with existing anti-icing system will be performed with current tool capability.

Tool design characteristic/capability		Development required for ICE-GENESIS	Importance				Notes
			Essential	Important	Desirable	Nice to have	
General capabilities (Inputs required from system point of view to confirm the relative importance of these capabilities)	Able to perform a steady state thermal calculation of anti-iced surface		X				Constant heat flux or wall temperature at the surface. Option to model steady state conduction within the substrate. Not specific to ICE-GENESIS
Universal requirements for an ice protection analysis model	Analysis capability: Calculates the outcome for a user defined heat flux at the substrate		X				Not specific to ICE-GENESIS
	Analysis capability: Calculates the outcome for a user defined internal HTC and temperature			X			Not specific to ICE-GENESIS
	Design capability: Calculates what heat input is needed for a certain criterion to be fulfilled.			X			The details of this requirement need further clarification. Examples include: - What heat flux distribution is needed to obtain a specified surface temperature - How much heat is needed to obtain a full evaporation of the water within a specified area. Not specific to ICE-GENESIS
	Able to model ice shapes that form behind protected regions and where heating is insufficient.		X				Not specific to ICE-GENEIS
	Include heat flux from surface in heat balance equation.		X	X			Not specific to ICE-GENEIS
	Able to model lateral conduction through the substrate.			X			To prevent unrealistic steps in the surface temperature or runback ice shapes. Slightly more complex because solution of heat balance equations becomes iterative since downstream node affects upstream equation Not specific to ICE-GENESIS

Tool design characteristic/capability		Development required for ICE-GENESIS	Importance				Notes
			Essential	Important	Desirable	Nice to have	
Universal requirements for an ice protection analysis model (cont.)	Able to model evaporation of impinging/ runback water		X				Not specific to ICE-GENEIS
	Include heat flux from surface in heat balance equation.		X				Not specific to ICE-GENEIS
	Able to model lateral conduction through the substrate.			X			To prevent unrealistic steps in the surface temperature or runback ice shapes. Slightly more complex because solution of heat balance equations becomes iterative since downstream node affects upstream equation.

4.2.1.2.9 Non-heated or heated surfaces transient features

- Req #16: The software should handle the time evolution of the ice shape

4.2.1.2.9.1 Attributes description

Tool design characteristic/capability		Development required for ICE-GENESIS	Importance				Notes
			Essential	Important	Desirable	Nice to have	
General capabilities (Inputs required from system point of view to confirm the relative importance of these capabilities)	1) Able to perform a transient icing calculation	X	X				ICE GENESIS partners will investigate different techniques to track the ice surface displacement: mesh deformation, re-meshing, IBM
	2) Able to perform a transient anti-icing calculation.			X			Transient effects such as cycling of power at temperature control limits. Transient conduction modelled within the substrate and the ice but limited to NOT modelling the melting of ice at the surface and shedding.
	3) Able to perform a transient de-icing calculation.		X				Full transient effects modelled. Able to model ice melting at the surface and shedding. Not specific to ICE-GENESIS
For capability 2 (Transient anti-icing analysis)	Able to model heat flux at the surface as a function of time.		X				Not specific to ICE-GENESIS
	Able to model transient conduction effects through the substrate and the ice.		X				Anti-icing is achieved during the 'off' periods due to the heat stored in the substrate, therefore modelling of transient conduction is essential. Not specific to ICE-GENESIS
For capability 3 (Transient de-icing analysis)	Able to model heat flux at the surface as a function of time.		X				Not specific to ICE-GENESIS
	Able to model transient conduction effects through the substrate and the ice.		X				Not specific to ICE-GENESIS
	Able to model melting of ice		X				Not specific to ICE-GENESIS
Transient calculation methods	Able to perform a single-step first order (SS) calculation		X				Transient effects have been categorised into long time-scale and short time-scale effects. Long time-scale effects include multi-stepping (interaction between shape, flow and catch) and changes in the icing freestream icing conditions. Single step calculation is already available in 2D/3D. Not specific to ICE-GENESIS

Tool design characteristic/capability		Development required for ICE-GENESIS	Importance				Notes
			Essential	Important	Desirable	Nice to have	
	Able to perform a single predictor-corrector (PC) calculation	X	X				
	Able to perform a multiple-step (MS) calculation.	X	X				
	Able to perform a multiple-step predictor corrector (MSPC) calculation.					X	
For PC, MS and MSPC methods:	Generation of the ice shapes that can be directly processed by the grid generator.	X	X				Interesting formats for industrials are: Catia files and ICEM
	Complete automation of PC, MS process without user interaction.	X	X				Tracking and processing of the ice surface shall be robust enough to avoid a rework of the generated surface
	Automatic time-step selection for MS method and also intermediate step for PC methods.	X		X			Seen as important by AAs to remove user dependency. At least, best practices to be provided for the definition of the time-step.
	Automatic surface discretization setting for MS and MSPC methods	X		X			At least, best practices to be provided for the definition of the surface discretization setting.
	Generation of the ice shapes with mass conservation.			X			The volume of the ice shape shall be consistent with the ice density and the mass balance of the ice accretion calculation. Not specific to ICE-GENESIS
	Generation of the ice shape taking into account ice bridging.			X			The surface tracking shall be able to handle hole closure, but also cases with bridging between ice shapes from two components (example: ice on an engine wall and on a blade leading edge) Not specific to ICE-GENESIS
	Automatic time-step calculation based on predicted error for MS and MSPC methods and also intermediate step for PC methods.				X		
	Able to model changes in the icing conditions.	X		X			Long time-scale changes, so that it can be assumed that accretion from previous time steps has no effect on the new heat balance.
	Modelling of ice sublimation rates: Ignoring where the original substrate is.			X			Not specific to ICE-GENESIS
For PC, MS and MSPC methods (cont.)	Modelling of ice sublimation rates: Stopping ice sublimation when it reaches the original substrate.			X			

Tool design characteristic/capability		Development required for ICE-GENESIS	Importance				Notes
			Essential	Important	Desirable	Nice to have	
	Melting of ice for subsequent warm temperature calculation steps					X	
Transient effects: short time-scale effects	Modelling of transient conduction effects, rather than a solution of the adiabatic surface heat balance for each time-step.			X			This capability could enable flight test data to be used with more confidence, or at least investigate the effects of rapidly varying conditions on the shape.
	Able to calculate rapidly varying LWC			X			Not need to re-compute trajectories etc.
	Able to calculate rapidly varying MVD				X		Need to recalculate trajectories, or re-compute catch from a series of catch data obtained previously for standard droplet diameters
	Able to calculate rapidly varying flight conditions					X	Need multiple CFD solutions. Solution would be very time consuming.
	Automatic adjustment of time step used for transient derivatives of the ice growth model to control errors.			X			

4.2.1.2.11 Industrial environment

- Req #17 : The software shall be compatible and comply with industrial simulation environment and platforms
- Req #18 : The software shall be delivered with a documented user guide, a theoretical manual, a non-regression/validation database and associated Best Practices
- Req #19 : The software should be structured with independent modules that can be interfaced with external modules
- Req #20 : The software shall be able to handle unstructured meshes and/or structured meshes (tetrahedral, prisms, hexahedra, pyramids)

4.2.1.2.11.1 Attributes description

Tool design characteristic/capability		Development required for ICE-GENESIS	Importance				Notes
			Essential	Important	Desirable	Nice to have	
Mesh size compatibility	Mesh size limited only by computer hardware.		X				Not specific to ICE-GENESIS
Mesh type compatibility	Single-block structured meshes		X				
	Multi-block structured meshes		X				
	Unstructured meshes – tetrahedral		X				
	Unstructured meshes – prisms		X				
	Unstructured meshes – hexahedra		X				
	Unstructured meshes – pyramids		X				
	Unstructured meshes – Arbitrary polyhedral			X			Includes capability for hybrid structured/unstructured meshes.
	Hanging node compatibility		X				Not specific to ICE-GENESIS
	Hanging face compatibility		X				Not specific to ICE-GENESIS
	Cartesian capability			X			
	Overlapping mesh capability			X			
	Adaptative unstructured meshes	X		X			
	Immersed boundary method	X		X			
Input & Output	Ability to read inputs (meshes, flow solutions) and write outputs in CGNS format	X	X				
Post-processing	Able to visualise the predicted ice surface		X				Not specific to ICE-GENESIS
	Able to visualise droplet trajectories		X				
	Able to visualise the surface local catch efficiencies (β parameter)		X				Not specific to ICE-GENESIS
	Able to visualise local LWC concentration (α parameter)		X				
	Able to visualise local ice growth rates			X			Not specific to ICE-GENESIS

Tool design characteristic/capability		Development required for ICE-GENESIS	Importance				Notes
			Essential	Important	Desirable	Nice to have	
Post-processing (cont.)	Able to visualise wall surface temperature		X				
	Able to generate Catia surface/solid from predicted ice.		X				
	Able to visualise ice debris shape, size at the shedding location.		X				
	Able to visualise ice debris trajectory, impact location and relative energy.		X				
	Able to characterise the water film on the skin (speed and thickness)	X		X			
Documentation	User guide documentation, validation report, non-regression report, best practices (incl. mesh convergence influence)	X	X				
Structure organization	Independent modules (flow solver, trajectory solver, ice accretion solver) coupled via interfaces	X	X				

4.3 Conclusions

These specifications are established on the needs of industrials involved in ICE-GENESIS. They take into account numerous needs coming from various industrial fields such as, airframe, rotorcraft, engine, suppliers….

This document is meant to be as much comprehensive and easy to understand as possible, in order to clearly put ahead the essential part of the work which is expected in ICE-GENESIS. This effort will be used by WP9 to prepare basic experiments and WP11 partners for validation purpose.

Final results obtained at the end of the project will be also assessed by using these requirements in order to evaluate the achieved improvement and what is still remaining for future projects.

4.4 Bibliography

[1]: HAIC/STORM D62.1.Model, Tool and Validation Specification

